Turkish Journal of
Analytical
Chemistry

2019

Turkish Journal of
Analytical Chemistry
TurkJAC

Volume 2
Issue 1
June 2020

Prof. Fikret Karadeniz — Kafkas University, Faculty of Science and Literature, Department of Chemistry

Prof. Mehmet Yaman — Fırat University, Faculty of Sciences, Department of Chemistry

Prof. Halit Kantekin — Karadeniz Technical University, Faculty of Sciences, Department of Chemistry

Prof. Esin Canel — Ankara University, Faculty of Sciences, Department of Chemistry

Prof. Dilek Ak — Anadolu University, Faculty of Pharmacy, Department of Basic Pharmaceutical Sciences

Prof. Mustafa Küçükislamoğlu — Sakarya University, Faculty of Science and Literature, Department of Chemistry

Prof. Salih Zeki Yildiz — Sakarya University, Faculty of Science and Literature, Department of Chemistry

Prof. Recai İnam — Gazi University, Faculty of Sciences, Department of Chemistry

Prof. Dr. Durişehvar Ünal — İstanbul University, Faculty of Pharmacy, Department of Basic Pharmaceutical Sciences

Prof. Mehmet Tüfekçi — Avrasya University, Faculty of Science and Literature, Department of Biochemistry

Prof. Hüseyin Kara — Selçuk University, Faculty of Sciences, Department of Chemistry

Prof. Sezgin Bakirdere — Yıldız Technical University, Faculty of Science and Literature, Department of Chemistry

Prof. Hasan Basri Şentürk — Karadeniz Technical University, Faculty of Sciences, Department of Chemistry

Prof. Yusuf Atalay — Sakarya University, Faculty of Science and Literature, Department of Physics

Prof. Salih Zeki Yildiz — Sakarya University, Faculty of Science and Literature, Department of Chemistry

Authorship, Originality, and Plagiarism: The authors accept that the work is completely original and that the works of others have been appropriately cited or quoted in the text with the necessary permissions. The authors should avoid plagiarism. It is recommended that they check the article using appropriate software such as Ithenticate and CrossCheck. The responsibility for this matter rests entirely with the authors. All authors will be notified when the manuscript is submitted. If a change of author is needed, the reason for the change should be indicated. Once the manuscript is accepted, no author changes can be made.

Aims and Scope

"Turkish Journal of Analytical Chemistry" publishes original full-text research articles and reviews covering a variety of topics in analytical chemistry. Original research articles may be improved versions of known analytical methods. However, studies involving new and innovative methods are preferred. Topics covered include:

- Analytical materials
- Atomic methods
- Biochemical methods
- Chromatographic methods
- Electrochemical methods
- Environmental analysis
- Food analysis

- Forensic analysis
- Optical methods
- Pharmaceutical analysis
- Plant analysis
- Theoretical calculations
- Nanostructures for analytical purposes
- Chemometric methods

ETHICAL GUIDELINES

TurkJAC follows ethical tasks and responsibilities are defined by the Committee on Publication Ethics (COPE) in publication procedure. Based on this guide, the rules regarding publication ethics are presented in the following sections.

Ethical Approval

Ethics committee approval must be obtained for studies on clinical and experimental regarding human and animals that require an ethical committee decision, this approval must be stated in the article and documented in the submission. In such articles, the statement that research and publication ethics are complied with should include. Information about the approval such as committee name, date, and number should be included in the method section and also on the first/last page of the article.

Editors

1. In the preliminary evaluation of a submission, the editor of the journal evaluates the article's suitability for the purpose and scope of the journal, whether it is similar to other articles in the literature, and whether it meets the expectations regarding the language of writing. When it meets the mentioned criteria, the scientific evaluation process is started by assigning a section editor if necessary.
2. A peer-reviewed publication policy is employed in all original studies, taking into full account of possible problems due to related or conflicting interests.
3. Section editors work on the articles with a specific subject and their suggestion is effective in the journal editor's decision about acceptance or rejection of the article.
4. No section editor contacts anyone except the authors, reviewers, and the journal editor about articles in the continued evaluation process.
5. In the journal editor's decision to accept or reject an article, in the addition of section editor's suggestion in consequence of scientific reviewing, the importance of the article, clarity and originality are decisive. The final decision, in this case, belongs to the journal editor.

Authors

1. The authors should actively contribute to the design and execution of the work. Authorship should not be given to a person who does not have at least one specific task in the study.
2. Normally all authors are responsible for the content of the article. However, in interdisciplinary studies with many authors, the part that each author is responsible for should be explained in the cover letter.
3. Before the start of the study it would be better to determine the authors, contributors, and who will be acknowledged in order to avoid conflict in academic credits.
4. The corresponding author is one of the authors of the article submitted to the journal for publication. All communications will be conducted with this person until the publication of the article. The copyright form will be signed by the corresponding author on all the authors' behalf.
5. It is unacceptable to submit an article that has already been published entirely or partly in other publication media. In such situation, the responsibility lies with all authors. It is also unacceptable that the same article has been sent to TurkJAC and another journal simultaneously for publication. Authors should pay attention to this situation in terms of publication ethics.
6. Plagiarism from others' publications or their own publications and slicing of the same study is not acceptable.
7. All authors agree that the data presented in the article are real and original. In case of an error in the data presented, the authors have to be involved in the withdraw and correction process.
8. All authors must contribute to the peer-reviewed procedure.

Reviewers

1. Peer reviewers worked voluntarily are external experts assigned by editors to improve the submitted article.
2. It is extremely important that the referee performs the review on time so that the process does not prolong. Therefore, when the invitation is agreed upon, the reviewer is expected to do this on time. Also, the reviewer agrees that there are no conflicts of interest regarding the research, the authors, and/or the research funders.
3. Reviewers are expected not to share the articles reviewed with other people. The review process should be done securely.
4. Reviewers are scored according to criteria such as responding to the invitations, whether their evaluations are comprehensive and acting in accordance with deadlines, and the article submissions that they can make to TurkJAC are handled with priority.

Contents

*Author of correspondence:

Preparation and characterization of self-standing and flexible CuS/rGO composite paper

Ezgi Topçu* 🆔, Kader Dağcı Kıranşan 🆔

Atatürk University, Faculty of Science, Department of Chemistry, 25240, Erzurum, Turkey

Abstract

A self-standing, durable, and flexible CuS/reduced graphene oxide (rGO) composite paper electrode was synthesized through a facile electrochemical deposition of CuS on the surface of the rGO paper. CuS/rGO composite paper electrode was characterized by using X-ray photoelectron spectroscopy (XPS), X-ray diffraction (XRD), scanning electron microscopy (SEM), and Raman spectroscopy. The morphological characterization displayed that the surface of the rGO paper electrode was covered with ball-like CuS structures. Microstructures of rGO and CuS/rGO papers and the intensity of surface defects were compared with Raman spectra. Electrochemical studies exhibited that as-prepared flexible CuS/rGO composite paper electrode has very high electrochemical activity.

Keywords: CuS, graphene-based electrode, characterization

1. Introduction

Graphene papers are generally used to obtain flexible electrodes [1-3]. These materials, due to possessing cuttable, rollable, and shapeable features, have attracted more interest in many areas such as hydrogen-oxygen evolution reactions [4], lithium-ion batteries [5], supercapacitors [6], and sensors [7-9]. Recent studies have shown that flexible graphene papers display excellent chemical, mechanical, and physical features such as high mechanical strength, high electrical conductivity, chemical stability, and flexibility [10,11].

Graphene papers can be modified with various materials to prepare composite graphene-based papers, resulting in improving mechanical, electrical, and chemical properties of the graphene-based papers [12,13]. In this regard, modification of the graphene surfaces with semiconductor metal chalcogenides attracts attention in recent years [14,15].

Among the different semiconductors, the covellite phase copper monosulfide (CuS) is the most important metal chalcogenide, which is of great interest with its modern applications ranging from biomedical to industrial and its structural, optical, and surface properties, which are very different from the bulk material due to its superior chemical and physical properties. CuS is a non-toxic p-type semiconductor having a direct band gap [14]. The importance of CuS in semiconductor materials is high conductivity, excellent metallic properties, and convertibility to superconductors at about 1.6K [16]. CuS nanostructures have been synthesized by various methods such as chemical co-precipitation method [17], hydrothermal or solvothermal methods [18,19], solid-state reaction method [20] and sonoelectrochemical method [21] over the years.

In this study, CuS structures synthesized through a simple hydrothermal method were coated on the rGO paper electrode surface by using the electrochemical technique. The morphological and structural analysis of CuS/rGO composite paper was characterized by using XPS, XRD, SEM, and Raman spectroscopy, and the electrochemical performance of this composite paper was investigated by using CV and EIS techniques. The results of the characterization studies showed that self-standing CuS/rGO composite paper was successfully prepared and its electrochemical activity was high enough to be used as an electrode

2. Experimental section

2.1. Preparation of rGO paper

Modified Hummer's method was used to synthesize GO [22]. 100 mL of the GO (1.0 mg mL^{-1}) suspension was filtrated through a nucleopore polycarbonate membrane filter (Whatman; Ø=47 mm; pore size, 0.2 µm) by using ultrafiltration vacuum cell. To obtain GO paper, this process is followed by washing, air drying, and peeling off from the filter. GO paper was immersed in a HI solution for 1 h to fabricated rGO paper. The rGO paper was washed with copious ethanol and distilled water and dried in air. This conductive rGO paper, prepared with a radius of approximately 47 mm each time, was cut into a strip shape (25 mm x 5 mm) and directly used as an electrode in the electrochemical studies.

2.2. Synthesis of CuS crystals

Copper (II) sulfate pentahydrate (CuSO$_4$·5H$_2$O) and sodium sulfide nonahydrate (Na$_2$S·9H$_2$O) were used as precursors and L-cysteine (C$_3$H$_7$NO$_2$S) was used as a surface ligand [23]. The distilled water as the solvent was used to prepare all solutions. 5 ml of 0.1 M CuSO$_4$·5H$_2$O and 20 mL of 0.1 M C$_3$H$_7$NO$_2$S were mixed. The pH of the solution was adjusted to 11 with 2 M NaOH. 5.0 ml of 0.1 M Na$_2$S·9H$_2$O was added to this solution. The mixture was then refluxed and stirred at 95°C. The solution heated for 4 h before it was cooled down to room temperature. The formed precipitates were collected and washed with ethanol several times before it was dried at 60°C in the air [23].

2.3. Electrochemical fabrication of CuS/rGO composite paper

CuS dispersion was prepared through the ultrasonic treatment of the mixture of CuS powder, and 0.1 M NaNO$_3$ containing dimethylformamide (DMF: C$_3$H$_7$NO) and 0.05 M NaOH solutions. The electrodeposition of CuS on the surface of rGO paper was performed by applying cyclic voltammetry from 0 to -1200 mV potentials in a suspension of 5 mM CuS. The obtained paper was denoted as CuS/rGO.

2.4. Characterization

Scanning electron microscopy (SEM) images were performed by using SEM, ZEISS SIGMA 300 for the morphological investigations, equipped to the elemental analysis by energy-dispersive X-ray spectroscopy (EDS). The surface chemical composition was studied by X-ray photoelectron spectroscopy (XPS) using Spect-Flex with standart Al

X-ray source. Material characterization was acquired using the Rigaku TTR III X-ray diffractometer (XRD) with monochromatized Cu Kα radiation (λ=1.5406 Å). A micro-Raman spectrometer (WITech alpha 300R) was used to record Raman spectra under atmospheric conditions.

2.5. Electrochemical performance of composite paper electrode

In the three-electrode system, a strip of rGO paper was directly used as the working electrode, platinum wire and Ag/AgCl (saturated KCl) (BASi) electrode were used as counter and reference electrodes, respectively. Cyclic voltammetry (CV), and electrochemical impedance spectroscopy (EIS) tests were performed with Gamry (600 +) potentiostat system. The EIS were investigated over the frequency range from 0.1 to 1x10^5 Hz at the open circuit potential by using an AC voltage of 5 mV.

3. Results and discussion

The schematic of the fabrication of flexible CuS/rGO composite paper was shown in Fig. 1. rGO paper was prepared in two steps. Firstly, GO dispersion was filtrated through a simple vacuum filtration system to obtain GO paper. Then, GO paper was chemically reduced by immersing it into HI solution to provide conductivity and converted to rGO paper. This rGO paper was cut into a rectangular strip and directly used as a working electrode in the electrochemical system. rGO paper electrode surface was electrochemically coated with the CuS structure in the solution containing CuS, thus self-standing and flexible CuS/rGO paper electrode was successfully prepared in this way (Fig. 1).
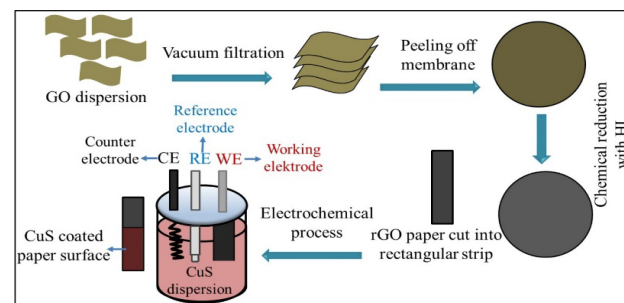
Figure 1. Schematic of the fabrication of flexible CuS/rGO composite paper.

SEM technique was used for the morphological characterization of the prepared rGO and CuS/rGO paper electrodes. SEM image of rGO paper was presented in Fig. 2a. The characteristic wrinkled structure of graphene was observed on the surface of

rGO paper (Fig. 2.a). SEM images of CuS/rGO paper (Fig. 2b and c) exhibited that porous ball-like structures of CuS covered the surface of rGO paper.
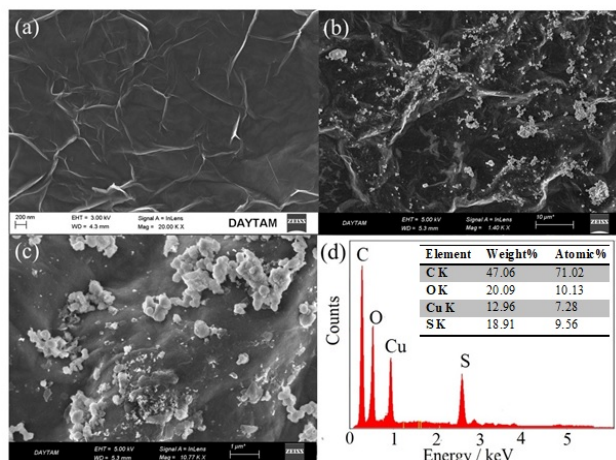
Figure 2. SEM images of (a) rGO paper, (b, c) CuS/rGO composite paper at different magnifications. (d) EDS spectra of CuS/rGO composite paper.

EDS profiles for surface structure analysis of CuS/rGO composite paper was shown in Fig. 2d. It was found that CuS/rGO composite paper contains C (47.06%), O (20.09%), Cu (12.96%), and S (18.91%), which attributed that the composite structure was successfully fabricated.
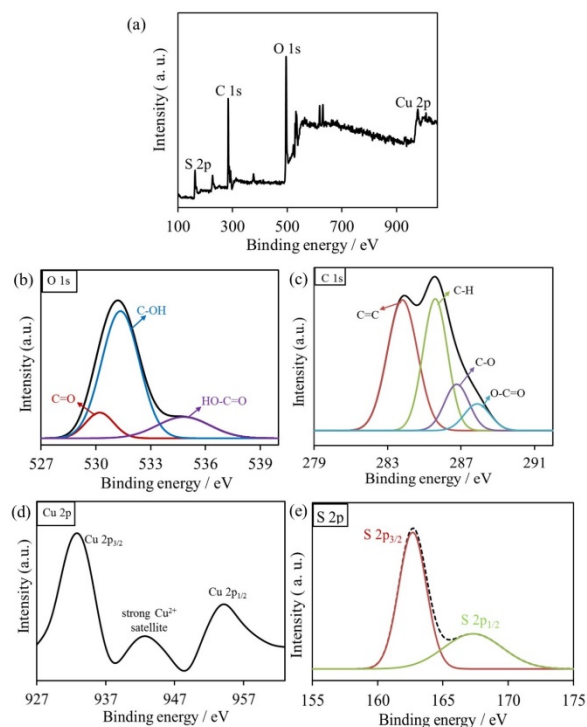
Figure 3. XPS spectra of CuS/rGO composite paper material: (a) survey, (b) O 1s, (c) C 1s, (d) Cu 2p, and (e) S 2p.

XPS method was used for chemical structure analysis of as-prepared flexible CuS/rGO composite paper. In the XPS spectrum (Fig. 3a) demonstrated

that the CuS/rGO composite paper contains 45.37% C, 23.26% O, 17.25% Cu, and 20.35 % S atoms. The O 1s peak of CuS/rGO exhibited the presence of three types of O bonds, C=O, C-OH, and HO-C=O (Fig. 3b), while C 1s peak of CuS/rGO showed four types of C bonds, C=C, C-H, C-O, and O-C=O (Fig. 3c). In the Cu 2p high-resolution XPS spectrum of CuS/rGO (Fig. 3d), the binding energy peaks at 932 and 950 eV are corresponding to Cu $2p_{3/2}$ and Cu $2p_{1/2}$ [24]. S $2p_{3/2}$ and S $2p_{1/2}$ peaks formed at 162.5 eV and 167.5 eV attributed to the presence of S at the CuS/rGO paper (Fig. 3e) [16]. XPS results displayed that the designed composite paper was successfully fabricated in the desired composition.
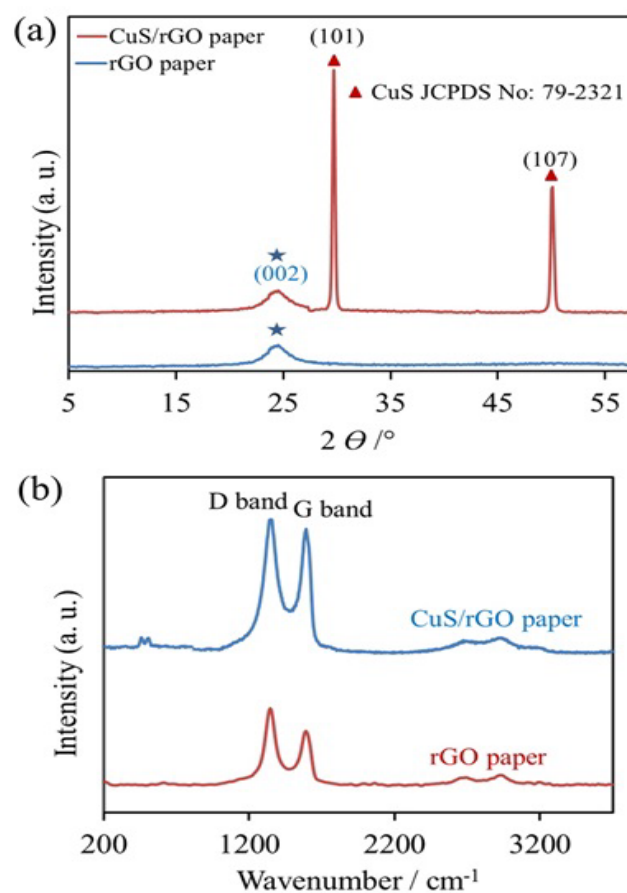
Figure 4. (a) XRD patterns, (b) Raman spectra of rGO, and CuS/rGO papers.

The XRD spectra of rGO and CuS/rGO papers were shown in Fig. 4a. In the XRD data of rGO paper, the diffraction peak (JCPDS 41-1487) corresponding to the characteristic rGO (002) crystal structure was observed at 24.8°. XRD spectrum of CuS/rGO paper, showed the peaks at about 29.5°, and 49.8°, corresponding to (101) and (107) structure of CuS, respectively (JCPDS 79-2321) [25]. Observation of the diffraction peaks of both rGO and CuS for CuS/rGO composite paper exhibited that this flexible composite paper was successfully prepared.

The Raman spectra of rGO and CuS/rGO composite papers were presented in Fig. 4b. Raman spectra of rGO paper showed G band, corresponding to E2g geometry of two dimensional hexagonal C=C sp^2 structure, at 1610 cm^{-1}. Besides, the D band was observed at 1365 cm^{-1}, resulting from defects of the graphene layers [4,9]. Raman spectrum of CuS/rGO composite paper showed peaks corresponding to CuS structure in the range of 200 to 1000 cm^{-1} in addition to D and G bands, attributing that the CuS structure deposited onto the rGO paper surface. The intensity of the D and G bands (I_D/I_G) is used to determine the surface defects of graphene-based papers. The I_D/I_G ratios of the rGO and CuS/rGO composite papers were calculated as 1.72 and 1.32, respectively. The I_D/I_G ratio of CuS/rGO composite paper is lower than that of rGO paper. This may be attributed to the deposition of CuS structures on surface defects of rGO paper.

CV measurements in the electrochemical solution containing $Fe(CN)_6^{3-/4-}$ redox pair were carried out to compare the electrochemical performance of rGO paper and CuS/rGO (Fig. 5a). ΔEp values of rGO and CuS/rGO papers were observed as 360 and 150 mV, respectively. In Fig. 5a, the peak current density of the CuS/rGO composite paper was about 2 times higher than the rGO paper. These results displayed that self-standing and flexible CuS/rGO composite paper has a quite high electrochemical activity.

For electrochemical studies, EIS is used to investigate the electron transfer mechanism in the electrode-solution interface. The Nyquist curves for rGO paper and CuS/rGO composite paper were presented in Fig. 5b. As seen from Fig.5b inset, the Nyquist curves were fitted according to the electrical circuit and electron transfer resistances (Rp) at the interface were determined for the paper electrodes. The smaller the Rp value, the easier the electron-transfer. Rp values of rGO paper and CuS/rGO composite paper were calculated as 125 and 78 Ω, respectively. The results showed that electron transfer over CuS/rGO composite paper would be easier compared to rGO paper. The cut-off point of the Z'_{re}-axis in the Nyquist curves is related to the solution resistance (Ru). Ru values of both paper electrodes were found to be very close since the same electrochemical solution was used [26].

Fig. 6 demonstrated the N_2 adsorption-desorption isotherms and pore size distributions of rGO and CuS/rGO papers at 77K. It was determined that due to CuS structure on rGO surface, CuS/rGO exhibited a typical hysteresis cycle, which was resulting in a large number of mesoporous pore [27,28]. Isotherm

curves were compatible with the Brunauer-Emmett-Teller (BET) model.
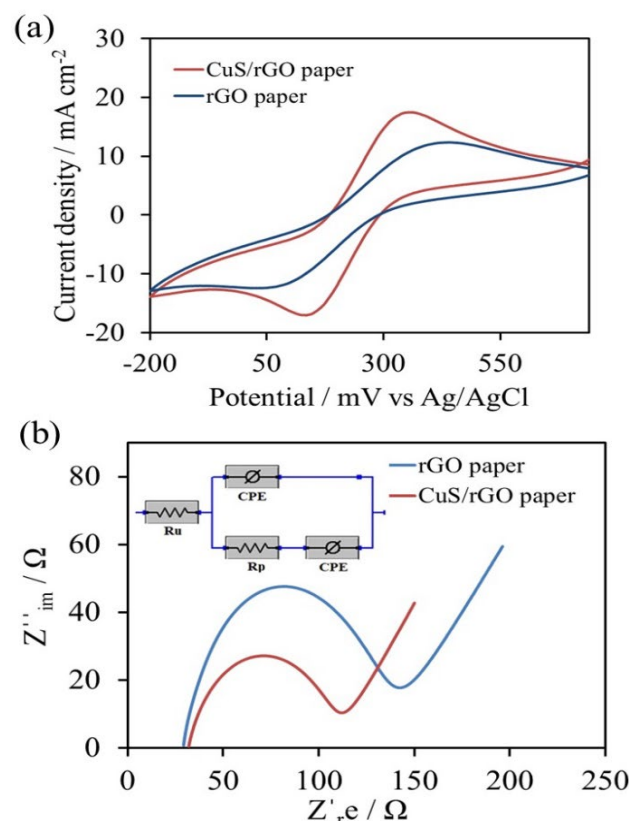
Figure 5. (a) CV curves, (b) Nyquist plots of rGO and CuS/rGO paper electrodes in a solution containing 10 mM $K_3Fe(CN)_6$, 10 mM $K_4Fe(CN)_6$ and 0.1 M KNO_3. Inset: The equivalent circuit model. Frequency range: 0.1-10^5 Hz.
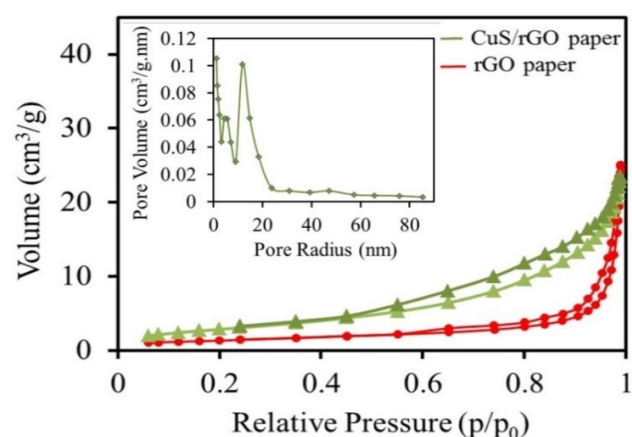
Figure 6. (a) N_2 adsorption-desorption isotherms of rGO, and CuS/rGO papers. Inset: BJH pore size distributions of CuS/rGO paper.

BET surface areas and Barrett-Joyner-Halenda (BJH) pore size distributions [29] of rGO and CuS/rGO papers were shown in Table 1. The surface area of the rGO and CuS/rGO papers was calculated as 40 and 62 m^2 g^{-1}, respectively (Table 1). Table 1 exhibited that CuS/rGO composite paper has a large surface area and high pore size, compared to rGO paper. This

porous property of flexible composite paper can provide an effective surface area for electrochemical studies [30].

Table 1. BET surface area and average pore size of rGO and CuS/rGO papers.

Paper Electrodes	BET surface area ($m^2\ g^{-1}$)	Average pore radius (nm)
rGO	39	3-9
CuS/rGO	61	4-16

4. Conclusion

CuS structures synthesized through a simple hydrothermal method were electrochemically coated onto the surface of rGO paper to prepare flexible and self-standing CuS/rGO composite paper. In the morphological characterization of CuS/rGO composite paper, it was observed that the surface of the rGO was covered homogeneously with ball-like CuS structures. Structural analysis performed with XPS, XRD, and Raman techniques showed that the flexible CuS/rGO paper electrode was successfully prepared in the desired composition. Electrochemical studies demonstrated that the electrochemical activity of flexible CuS/rGO composite paper is high enough to be used as an electrode.

References

[1] K.D. Kıranşan, E. Topçu, M. Alanyalıoğlu, Surface-confined electropolymerization of pyronin Y in the graphene composite paper structure for the amperometric determination of dopamine, J Appl Polym Sci, 134, 2017, 45139.

[2] K. Dağcı, M. Alanyalıoğlu, Preparation of free-standing and flexible graphene/Ag nanoparticles/poly(pyronin Y) hybrid paper electrode for amperometric determination of nitrite, ACS Appl Mater Inter, 8, 2016, 2713-2722.

[3] E. Topçu, K. Dağcı, M. Alanyalıoğlu, Free-standing graphene/poly(methylene blue)/AgNPs composite paper for electrochemical sensing of NADH, Electroanal, 28, 2016, 2058-2069.

[4] E. Topçu, K.D. Kıranşan, Flexible andfree-standing PtNLs-MoS₂/reduced graphene oxide composite paper: A High-performance rolled paper catalyst for hydrogen evolution reaction, ChemistrySelect, 3, 2018, 5941-5949.

[5] K.D. Kıranşan, E. Topçu, Graphene paper with sharp-edged nanorods of Fe-CuMOF as an excellent electrode for the simultaneous detection of catechol and resorcinol, Electroanal, 31, 2019, 2518-2529.

[6] K. Dağcı Kıranşan, M. Aksoy, E. Topçu, Flexible and freestanding catalase-Fe₃O₄/reduced graphene oxide paper: Enzymatic hydrogen peroxide sensor applications, Mater Res Bull, 106, 2018, 57-65.

[7] J.K. Lee, K.B. Smith, C.M. Hayner, H.H. Kung, Silicon nanoparticles-graphene paper composites for Li ion battery anodes, Chem Commun, 46, 2010, 2025-2027.

[8] E. Topçu, K. Dağcı Kıranşan, Flexible gold nanoparticles/rGO and thin film/rGO papers: novel electrocatalysts for hydrogen evolution reaction, J Chem Technol Biot, 94, 2019, 3895-3904.

[9] K. Chi, Z. Zhang, J. Xi, Y. Huang, F. Xiao, S. Wang, Y. Liu, Freestanding graphene paper supported three-dimensional porous graphene-polyaniline nanocomposite synthesized by inkjet printing and in flexible all-solid-state supercapacitor, ACS Appl Mater Inter, 6, 2014, 16312-16319.

[10] K.D. Kıranşan, E. Topçu, Free-standing and flexible MoS₂/rGO paper electrode for amperometric detection of folic acid, Electroanal, 30, 2018, 810-818.

[11] E. Topçu, K.D. Kıranşan, Electrochemical simultaneous sensing of melatonin and ascorbic acid at a novel flexible B-RGO composite paper electrode, Diam Relat Mater, 105, 2020, 107811.

[12] E. Topçu, Three-dimensional, free-standing, and flexible cobalt-based metal-organic frameworks/graphene composite paper: A novel electrochemical sensor for determination of resorcinol, Mater Res Bull, 121, 2020, 110629.

[13] K.D. Kıranşan, Preparation and characterization of highly flexible, free-standing, three-dimensional and rough NiMOF/rGO composite paper electrode for determination of catechol, ChemistrySelect, 4, 2019, 6488-6495.

[14] H. Li, Y. Wang, J. Huang, Y. Zhang, J. Zhao, Microwave-assisted synthesis of CuS/graphene composite for enhanced lithium storage properties, Electrochim Acta, 225, 2017, 443-451.

[15] J.T. Cao, Y.X. Dong, Y. Ma, B. Wang, S.H. Ma, Y.M. Liu, A ternary CdS@Au-g-C₃N₄ heterojunction-based photoelectrochemical immunosensor for prostate specific antigen detection using graphene oxide-CuS as tags for signal amplification, Anal Chim Acta, 1106, 2020, 183-190.

[16] A.A. Sagade, R. Sharma, Copper sulphide (CuxS) as an ammonia gas sensor working at room temperature, Sensor Actuat B Chem, 133, 2008, 135-143.

[17] N. Sreelekha, K. Subramanyam, D. Amaranatha Reddy, G. Murali, S. Ramu, K. Rahul Varma, R.P. Vijayalakshmi, Structural, optical, magnetic and photocatalytic properties of Co doped CuS diluted magnetic semiconductor nanoparticles, Appl Surf Sci, 378, 2016, 330-340.

[18] M. Saranya, C. Santhosh, R. Ramachandran, P. Kollu, P. Saravanan, M. Vinoba, S.K. Jeong, A.N. Grace, Hydrothermal growth of CuS nanostructures and its photocatalytic properties, Powder Technol, 252, 2014, 25-32.

[19] X.S. Hu, Y. Shen, L.H. Xu, L.M. Wang, Y.J. Xing, Preparation of flower-like CuS by solvothermal method and its photodegradation and UV protection, J Alloy Compd, 674, 2016, 289-294.

[20] W. Wang, L. Ao, Synthesis and characterization of crystalline CuS nanorods prepared via a room temperature one-step, solid-state route, Mater Chem Phys, 109, 2008, 77-81.

[21] Y. Zhao, H. Pan, Y. Lou, X. Qiu, J. Zhu, C. Burda, Plasmonic Cu₂₋ₓS nanocrystals: Optical and structural properties of copper-deficient copper (I) sulfides, J Am Chem Soc, 131, 2009, 4253-4261.

[22] N.I. Kovtyukhova, Layer-by-layer assembly of ultrathin composite films from micron-sized graphite oxide sheets and polycations, Chem Mater, 11, 1999, 771-778.

[23] N. Loudhaief, M. Ben Salem, H. Labiadh, M. Zouaoui, Electrical properties and fluctuation induced conductivity studies of Bi-based superconductors added by CuS nanoparticles synthesized through the aqueous route, Mater Chem Phys, 242, 2020, 122464.

[24] S. Iqbal, A. Bahadur, A. Saeed, K. Zhou, M. Shoaib, M. Waqas, Electrochemical performance of 2D polyaniline anchored CuS/Graphene nano-active composite as anode material for lithium-ion battery, J Colloid Interf Sci, 502, 2017, 16-23.

[25] T. Hurma, S. Kose, XRD Raman analysis and optical properties of CuS nanostructured film, Optik (Stuttg), 127, 2016, 6000-6006.

[26] D. Song, J. Xia, F. Zhang, S. Bi, W. Xiang, Z. Wang, L. Xia, Y. Xia, Y. Li, L. Xia, Multiwall carbon nanotubes-poly(diallyldimethylammonium chloride)-graphene hybrid composite film for simultaneous determination of catechol and hydroquinone, Sensor Actuat B Chem, 206, 2015, 111-118.

[27] D. Jiang, Q. Xu, S. Meng, C. Xia, M. Chen, Construction of cobalt sulfide/graphitic carbon nitride hybrid nanosheet composites for high performance supercapacitor electrodes, J Alloy Compd, 706, 2017, 41-47.

[28] J. Luo, J. Lai, N. Zhang, Y. Liu, R. Liu, X. Liu, Tannic acid induced self-assembly of three-dimensional graphene with good adsorption and antibacterial properties, ACS Sustain Chem Eng, 4, 2016, 1404-1413.

[29] Y. Li, H. Bin Zhang, L. Zhang, B. Shen, W. Zhai, Z.Z. Yu, W. Zheng, One-pot sintering strategy for efficient fabrication of high-performance and multifunctional graphene foams, ACS Appl Mater Inter, 9, 2017, 13323-13330.

[30] J. Sha, C. Gao, S.K. Lee, Y. Li, N. Zhao, J.M. Tour, Preparation of three-dimensional graphene foams using powder metallurgy templates, ACS Nano, 10, 2016, 1411-1416.

Turkish Journal of
A n a l y t i c a l C h e m i s t r y
w w w . t u r k j a c . o r g
2 0 1 9

TurkJAC

Adsorptive removal of Cr(VI) ions from aqueous solutions by H₂SO₄ modified oak (*Quercus* L.) sawdust

Duygu Özdeş[1*] (iD), İbrahim Yıldırım[2] (iD), Celal Duran[3] (iD)

[1]Gümüşhane University, Gümüşhane Vocational School, Department of Chemistry and Chemical Processing Technologies, 29100, Gümüşhane, Turkey
[2]Gümüşhane University, Institute of Science, 29100, Gümüşhane, Turkey
[3]Karadeniz Technical University, Faculty of Sciences, Department of Chemistry, 61080, Trabzon, Turkey

Abstract

In this study, the utilization of H₂SO₄ modified oak sawdust (*Quercus* L.) (HMOS) as a new and promising sorbent for the uptake of an extremely toxic inorganic pollutant, Cr(VI), from aqueous media by batch adsorption method has been investigated. The HMOS has been characterized by different methods such as Boehm titration, pH$_{pzc}$, and moisture content. Some of the process parameters including initial solution pH, equilibrium time, initial Cr(VI) concentration, HMOS amount, and salt effect were examined in detail in order to optimize the experimental conditions for the uptake of Cr(VI) ions onto HMOS. The maximum Cr(VI) uptake was achieved at initial solution pH of 2.5 and at equilibrium time of 240 min. The adsorption behaviors of Cr(VI) ions onto both natural oak sawdust (NOS) and HMOS were analyzed in terms of Langmuir and Freundlich isotherm models and the Cr(VI) adsorption was obtained to be compatible with both isotherm models. The Cr(VI) adsorption capacities of NOS and HMOS were calculated as 48.07 and 100.00 mg g^{-1}, respectively by utilizing the Langmuir model. As a result, H₂SO₄ modified oak sawdust provides a strong alternative to remove Cr(VI) ions from wastewaters.

Keywords: Adsorption, chromium, heavy metal, isotherm, Oak Sawdust

1. Introduction

Heavy metals, which occur naturally in the earth's crust, cause serious troubles to both the environment and all of the living organisms depending on their types and levels [1]. Chromium, which is a major heavy metal pollutant in aqueous media, is usually spread into both the environment and the water sources by virtue of several industrial activities such as metal plating, batteries, paper production, leather tanning, pesticides, mining and electroplating [2-4]. Although chromium is found at different oxidation states in nature, only two of them are stable: Cr(III) and Cr(VI). The solubility, mobility, and toxicity of these two chromium species are different from each other. Cr(III) has an important part in carbohydrate metabolism hence it is an essential element for the human body. Nevertheless, Cr(VI), which exists in aqueous solutions as chromate (CrO_4^{2-} or $HCrO_4^-$) and dichromate ($Cr_2O_7^{2-}$) depending on solution pH and its concentration, may cause serious damages to the living organism. Cr(VI) is a strong oxidizing agent and easily absorbed in the human body via digestion, respiratory system, skin, and mucous membrane. Eventually, it may induce many health problems such as skin irritation, lung cancer, gastric and liver damage, ulcer formation, and nervous system failure [5,6]. The permissible limit for Cr(VI) in drinking water is recommended as 0.05 mg L^{-1} by World Health Organization (WHO) [7]. That is why it is compulsory to develop economical and efficient methods for purification of waters contaminated with Cr(VI) ions by virtue of various industrial activities.

Several techniques including reverse osmosis [8], coagulation [9], ion exchange [10], advanced oxidation [11], and adsorption [12] have been carried out in order to remove Cr(VI) from water resources. Adsorption method, performed without causing a secondary waste generation, is commonly utilized in wastewater treatment due to its high selectivity, simplicity of design, low cost, and high efficiency

when compared with other conventional techniques. The choosing of adsorbents plays a significant role during the adsorption process. Adsorbents, used in developed processes should be inexpensive and easily available, which are not harmful to the environment. In addition, they should have a large specific surface area and have functional groups that can interact with the target pollutants [13].

The agroforestry wastes, which are the by-product of agricultural and forestry production, substantially composed of polyphenolic compounds and hydroxyl groups originating from tannin and lignin. These functional groups are known to be the active sites for the binding of heavy metal ions. Sawdust is a timber industry waste product and it is used as a fuel or a packaging material. It contains lignin and cellulose, and it is comprised of electron rich-functional groups [14]. Acid and alkali treatment of sawdust enhances the pollutant uptake capacity of them. Agricultural waste by-products have been used in the adsorption process as efficient adsorbents in the removal of both organic and inorganic pollutants recently since they are low cost and easily available. Until now, several agricultural wastes have been reported in the literature including date pit and olive stone [5], sugarcane bagasse [15], corncob [16], rice husk [17], Citrus limetta peel [18], peanut shell [19], and apple peel [20], etc. to uptake Cr(VI) from aqueous media.

In this study, H_2SO_4 modified oak (*Quercus* L.) sawdust (HMOS) was prepared and applied to remove Cr(VI) ions from aqueous solution. To our best knowledge, no study has been reported on the removal of any pollutant by using H_2SO_4 modified oak (*Quercus* L.) sawdust. The HMOS was characterized by different techniques. Subsequently, to achieve the optimum uptake conditions, the effects of various experimental parameters including initial solution pH, initial Cr(VI), and HMOS concentration and contact time on the process were evaluated. The adsorption isotherms were used to determine the Cr(VI) adsorption capacity of HMOS and to interpret the adsorption mechanism.

2.   Materials and methods

2.1. Preparation and characterization of HMOS

For the modification of the oak sawdust with H_2SO_4, 20 g of the oak sawdust was taken without grinding, and 20 mL of concentrated H_2SO_4 was added and mixed well. The mixture was left on a hot plate at 200°C for 24 hours. After this period, the adsorbent was washed with boiled distilled water for several

times to neutralize the carbonized sample. The adsorbent was then treated with a 1% $NaHCO_3$ solution for 24 hours to completely neutralize the acid residues. After the modified adsorbent was filtered, it was washed well with distilled water and finally dried in the oven for 24 hours at 105°C. The obtained adsorbent (HMOS) was used in the adsorption process after grinding to a particle size of 150 μm [21, 22]. The pH_{pzc} (point of zero charge) and moisture content of HMOS were determined according to standard methods [23] while the surface acidic groups of it were obtained by Boehm titration [24].

2.2. Adsorption method

Adsorption studies were performed by a batch method using 15 mL polyethylene centrifuge tubes which were shaken by using BOECO PSU-15i model mechanical shaker at room temperature. The initial pH of the Cr(VI) solution was adjusted to the desired values by the addition of 0.1 M HNO_3 and NaOH solutions using Hanna pH-2221 model digital pH meter. The adsorption studies were performed in duplicate, and the Cr(VI) levels in the dilute phase were analyzed by Perkin Elmer Analyst 400 model flame atomic absorption spectrophotometer (FAAS). The adsorption studies were performed by mixing Cr(VI) solutions (10 mL) in the concentration range of 100-2300 mg L^{-1} and in the pH range of 1.0-8.0 with 10-200 mg of HMOS amount. The mixtures were shaken in the contact time range of 1-360 min at 350 rpm. After enough shaking time, the mixtures were centrifuged at 3500 rpm for 10 min. The Cr(VI) amounts in the aqueous phase were analyzed by FAAS and the adsorption amount was calculated by using the following equation;

$$q_e = \frac{V(C_o - C_e)}{m_s} \qquad (1)$$

C_o (mg L^{-1}) and C_e (mg L^{-1}) is the initial and equilibrium Cr(VI) concentration in aqueous solution, respectively, V (L) is the aqueous solution volume, m_s (g) is the HMOS amount, and q_e (mg g^{-1}) is the amount of calculated Cr(VI) adsorption onto 1.0 gram of HMOS.

3.   Results and discussion

3.1. Characterization of HMOS

The pH_{pzc} value of HMOS was determined as 2.6, which indicates that the surface acidic groups are more dominant than the basic groups. It is important

to know the pH_{pzc} values of the adsorbents in order to have an idea about the pH values, at which maximum adsorption will occur of the species that may be found in an anionic or cationic form in aqueous solutions. At $pH>pH_{pzc}$, the surface charge of adsorbent is negative, whereas $pH<pH_{pzc}$ the surface charge of adsorbent is positive. Thus, in the studies conducted at pH lower than the pH_{pzc} value of the adsorbent, it is thought that the anionic species in the aqueous solution such as Cr(VI) will be better adsorbed [25].

The values of the carboxylic and phenolic groups on the surface of HMOS were determined as 8.72 and 7.34 mmol g^{-1}, respectively, and the total acidic group amount was obtained as 16.06 mmol g^{-1}. It is seen that HMOS is rich in terms of total acidic groups and especially the amounts of carboxylic groups are higher than the phenolic groups. Besides, the moisture content of HMOS was determined as 9.5%.

3.2. Effect of initial solution pH

The influence of initial solution pH on the adsorptive removal of Cr(VI) ions by HMOS was investigated in the pH range of 1.0-8.0 by using 50 mg L^{-1} of initial Cr(VI) concentration and 5.0 g L^{-1} of HMOS. From Fig. 1, it is seen that the adsorption efficiency of Cr(VI) ions rises from 74.0% to 99.2% when pH increases from 1.0 to pH 2.5 and it decreases prominently after pH 2.5. Cr(VI) ions exist in the form of acid chromate ($HCrO_4^-$), chromate (CrO_4^{2-}), and dichromate ($Cr_2O_7^{2-}$) depending on the pH of the aqueous solution. In acidic pH values, the dominant form of Cr(VI) is $HCrO_4^-$, and the surrounding of HMOS is wrapped with H_3O^+ ions to make the surface functional groups positively charged. Thus at low pH values, an increase in the adsorption efficiency was observed because of occurring an electrostatic interaction between the $HCrO_4^-$ ions and the positively charged HMOS surface. At higher pH values the adsorption efficiency decreases because of the competitive effect of OH^- ions with $Cr_2O_7^{2-}$ ions, the dominant form of Cr(VI), to adsorb the active adsorption sites on the HMOS surface. Besides, the electrostatic repulsion between the same charged Cr(VI) ions and the HMOS surface decreases the adsorption efficiency at high pH values. The pH effect on the adsorption of Cr(VI) ions onto HMOS can also be explained by the pH_{pzc} value of the adsorbent. The pH_{pzc} value of HMOS was determined as 2.6. In the case of $pH<pH_{pzc}$, the net surface charge of HMOS is positive and the adsorption efficiency of Cr(VI) ions is expected to be high [25].

In subsequent experimental studies, the optimum pH value was determined as 2.5 for the adsorption of Cr(VI) ions onto HMOS (Fig. 1).
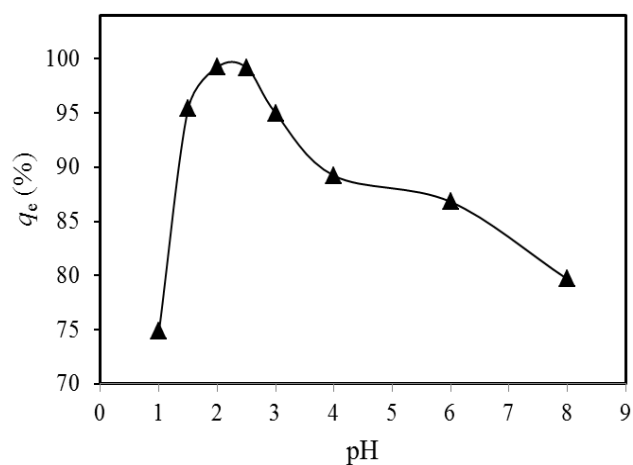
Figure 1. Effect of initial pH on Cr(VI) adsorption onto HMOS (initial Cr(VI) concentration: 50 mg L^{-1}; HMOS concentration: 5.0 g L^{-1})

3.3. Effect of contact time

In order to investigate the sufficient equilibrium time, the adsorption studies were carried out in the shaking time range of 1-360 min by mixing 230 mg L^{-1} of initial Cr(VI) concentrations containing 5.0 g L^{-1} of HMOS at initial pH 2.5. In the first stages of the adsorption (in the 1-30 minute time interval), the uptake of Cr(VI) ions onto HMOS occurs very quickly since the active adsorption sites are completely open. Subsequently, the adsorption rate gradually decreases due to the diffusion of Cr(VI) ions towards HMOS pores, and finally, the equilibrium occurs due to the saturation of the HMOS surfaces [12].

In the light of the results obtained in this parameter, the appropriate contact time for the adsorption of Cr(VI) ions onto HMOS was determined as 240 minutes (Fig. 2). No notable increases were noticed in the Cr(VI) uptake amount after this period.

3.4. Effect of HMOS amount

The influence of HMOS amount on the adsorption of Cr(VI) ions was investigated in the HMOS concentration range of 1.0-20.0 g L^{-1} by using 230 mg L^{-1} of initial Cr(VI) concentration at initial pH 2.5. When the amount of HMOS was increased from 1.0 to 20.0 g L^{-1}, the removal percentage increased from 29.3 to 86.0% as a result of the increase in the active adsorption surfaces. Conversely, the higher HMOS amount causes a decrease in total surface area due to the formation of agglomerates and of unsaturated adsorption surfaces [26], and thus the adsorption

amount decreased from 67.5 to 9.9 mg g^{-1} as increasing the amount of HMOS from 1.0 to 20.0 g L^{-1} (Fig. 3).
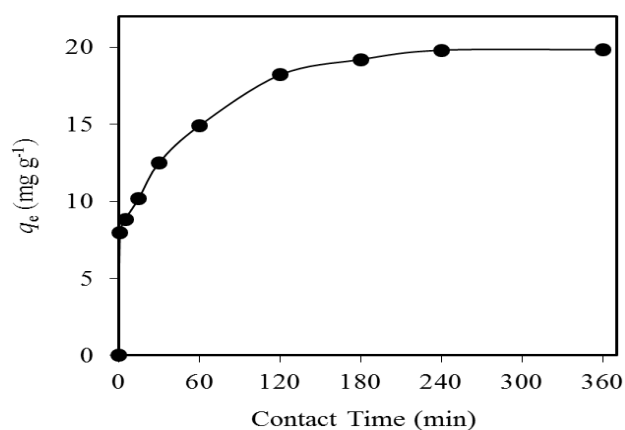
Figure 2. Effect of contact time on Cr(VI) uptake by HMOS (initial Cr(VI) concentration: 230 mg L^{-1}; HMOS concentration: 5.0 g L^{-1}; initial pH: 2.5**).**
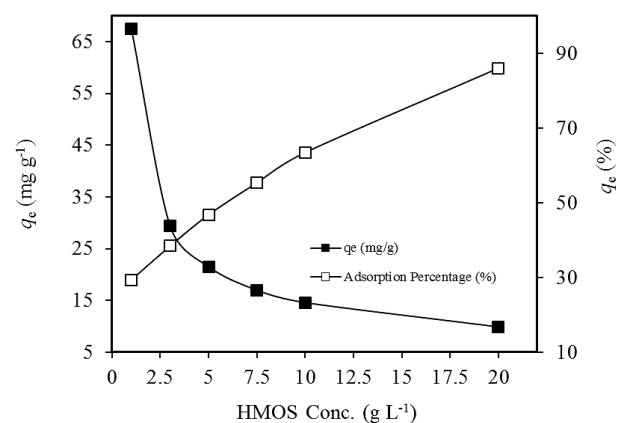
Figure 3. Effect of adsorbent amount on Cr(VI) uptake by HMOS (initial Cr(VI) concentration: 230 mg L^{-1}; initial pH: 2.5; contact time: 240 min).

3.5. Effect of initial Cr(VI) concentration and adsorption isotherms

The data obtained as a result of the investigation of the influence of initial metal concentration on the uptake of heavy metal ions is applied to various adsorption isotherms to have an idea about the capacities of the adsorbents. Therefore, to examine the change in Cr(VI) uptake capacity of oak sawdust due to the modification with H$_2$SO$_4$, the effect of increasing initial Cr(VI) concentration was evaluated for both natural oak sawdust (NOS) and H$_2$SO$_4$ modified oak sawdust (HMOS).

In order to evaluate the effect of initial Cr(VI) ions concentration on the adsorption efficiency of NOS ānd HMOS, a series of Cr(VI) solution at initial concentrations of 100-2300 mg L^{-1} were added to the centrifuge tubes containing 0.05 g NOS or HMOS, separately, and the mixtures were shaken until the

equilibrium reached. After centrifugation, the Cr(VI) concentrations remaining in the solutions were determined by FAAS and from the obtained data the relationship between the adsorbed Cr(VI) amounts (q_e) and the adsorption percentages (%) against initial Cr(VI) concentrations were plotted in Fig. 4 (for NOS) and in Fig. 5 (for HMOS).

By increasing the initial Cr(VI) concentration from 100 mg L^{-1} to 2300 mg L^{-1}; at constant NOS amount, the amount of adsorption increased from 7.7 mg g^{-1} to 40.0 mg g^{-1}, the percentage of adsorption decreased from 33.5% to 8.8% (Fig. 4) and at constant HMOS amount, the amount of adsorption increased from 11.9 mg g^{-1} to 78.4 mg g^{-1}, and the percentage of adsorption decreased from 52.0% to 17.3% (Fig. 5). At constant NOS and HMOS amount, the increase in initial Cr(VI) concentration causes a driving force to overcome mass transfer resistance for Cr(VI) transportation between the solution and the surface of NOS and HMOS, which increases the adsorption amount. Conversely, at high Cr(VI) concentrations, a saturation occurs on the active adsorption sites of NOS and HMOS surface which makes them less available for Cr(VI) binding thus the adsorption percentage decreases [27].
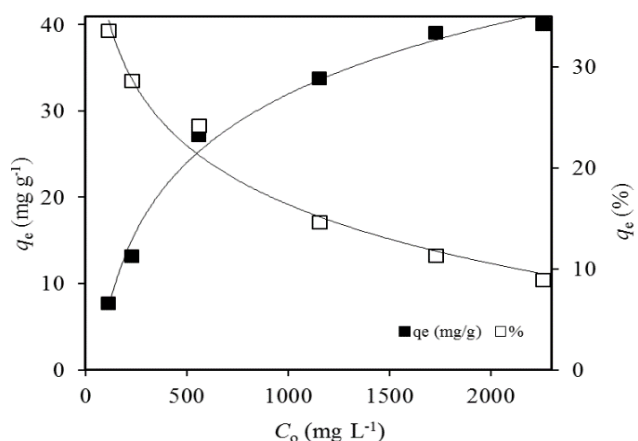
Figure 4. Effect of initial Cr(VI) concentration on its uptake by NOS (initial pH: 2.5; NOS concentration: 5.0 g L^{-1}; contact time: 240 min).

The Langmuir and Freundlich isotherm models were fitted to the experimental data in order to have an opinion about the mechanism of the adsorption of Cr(VI) ions onto NOS and HMOS. According to Langmuir isotherm model, the adsorption process occurs as a monolayer on homogeneous surfaces, and all active binding sites on the adsorbent surface have equal energy [28]. In contrast, the Freundlich isotherm model is based on the idea that the multilayer adsorption occurs on heterogeneous adsorbent surfaces [29].
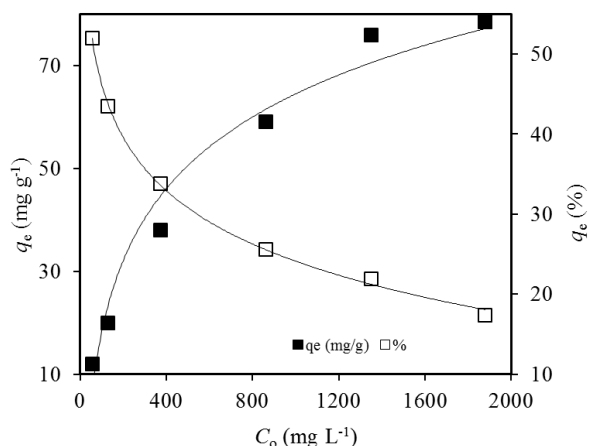
Figure 5. Effect of initial Cr(VI) concentration on its uptake by HMOS (initial pH: 2.5; HMOS concentration: 5.0 g L^{-1}; contact time: 240 min).

The linear forms of Langmuir and Freundlich isotherm models are given in Eqs. 2 and 3, respectively.

$$\frac{C_e}{q_e} = \frac{C_e}{q_{max}} + \frac{1}{bq_{max}} \qquad (2)$$

$$\ln q_e = \ln K_f + \frac{1}{n}\ln C_e \qquad (3)$$

where q_e (mg g^{-1}); Cr(VI) adsorption per unit mass of NOS and HMOS at equilibrium, C_e (mg L^{-1}); equilibrium concentration of Cr(VI) ions in solution, q_{max} (mg g^{-1}); maximum adsorption capacity of NOS and HMOS, b (L mg^{-1}); adsorption energy, K_f (mg g^{-1}); sorption capacity, and n; sorption intensity.

The suitability of the adsorption process can be evaluated by using the separation factor (R_L) related to Langmuir isotherm which is given in the following equation [30];

$$R_L = \frac{1}{1 + b.Co} \qquad (4)$$

where b (L mg^{-1}) is the Langmuir constant and C_o (mg L^{-1}) is the initial Cr(VI) concentration. R_L values should be in the range of 0-1 for favorable adsorption.

q_{max} and b values belong to Langmuir isotherm model were calculated from the slope and intercept of the linear plot of C_e/q_e versus C_e, respectively (Fig. 6(a) and (b)) and K_f and n values belong to Freundlich isotherm model were determined from the intercept and slope of the linear plot of $\ln q_e$ versus $\ln C_e$,

respectively (Fig. 7a and b). All of the isotherm constants were given in Table 1. The correlation coefficients calculated from the figures drawn by applying the linear equations are compared to determine which of the two models is more suitable for explaining the surface structure of the adsorbents. The correlation coefficients obtained from both the Langmuir and Freundlich isotherm models for the adsorption of Cr(VI) ions onto NOS and HMOS are greater than 0.95. This indicates that the active adsorption sites on the NOS and HMOS surface exhibit both the homogeneous and heterogeneous distribution [13].
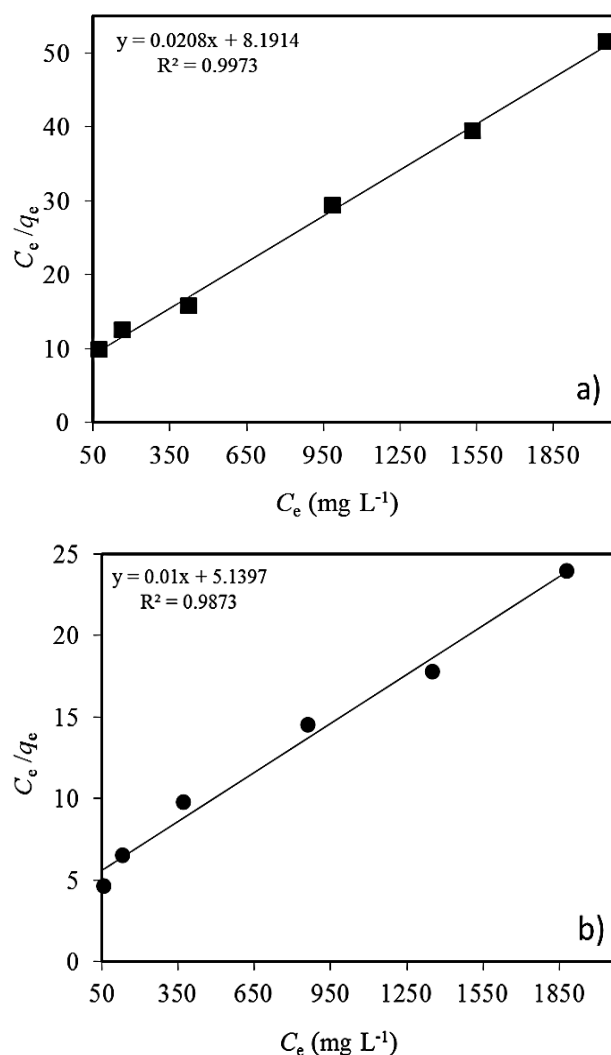
Figure 6. Langmuir isotherm model plotted for a) NOS b) HMOS.

One of the most important benefits of the Langmuir isotherm model is that it can be applied in the calculation of the maximum adsorption capacities of the adsorbents. By using the Langmuir isotherm model the maximum Cr(VI) adsorption capacity of NOS and HMOS has been calculated as 48.07 and

100.00 mg g^{-1}, respectively. As can be noticed from these values, as a result of the modification process of oak sawdust with H$_2$SO$_4$, Cr(VI) adsorption capacity has increased by about 100%. The maximum Cr(VI) adsorption capacity of NOS and HMOS has also been compared with the adsorbents previously used in the removal of Cr(VI) ions in the literature (Table 2). As seen in Table 2, the maximum Cr(VI) adsorption capacity of NOS and HMOS is better than many adsorbents given in the literature [31-39]. This comparison showed that NOS and HMOS can be utilized as effective and low-cost adsorbents in the removal of Cr(VI) ions from aqueous media.

Table 1. The isotherm parameters of Cr(VI) adsorption.

Langmuir isotherm model	NOS	HMOS
q_{max} (mg g^{-1})	48.07	100.0
b (L mg^{-1})	0.0025	0.0019
R^2	0.9973	0.9873
Freundlich isotherm model		
K_f (mg g^{-1})	0.99	1.36
n	1.98	1.81
R^2	0.9514	0.9930

The Langmuir and Freundlich isotherm models are also used to give an idea about the suitability of the studied adsorption system. For this purpose, the R_L values, indicating whether the adsorption process is suitable for the adsorbent-adsorbate pair, have been calculated using the Langmuir isotherm constant b. By increasing the initial Cr(VI) concentration from 100 mg L^{-1} to 2300 mg L^{-1}, the R_L values for NOS and HMOS varied between 0.81-0.18 and 0.18-0.01, respectively, suggesting that the adsorption of Cr(VI) ions onto both NOS and HMOS is favorable. Besides, n values calculated from the Freundlich isotherm model were determined as 1.98 and 1.81 for the adsorption of Cr(VI) ions onto NOS and HMOS, respectively. This result also supports the suitability of the adsorption process [40].

3.6. Effect of salt concentration
Industrial wastewaters contain various salts that generate ionic strength as well as toxic organic or inorganic pollutants. Such salts cause various effects by increasing or decreasing the pollutant removal efficiency. For this reason, it is significant to investigate the influence of ionic strength in order to evaluate the applicability and efficiency of the adsorption process applied to remove the heavy metal ions from waters and wastewaters.

The NaCl and BaCl$_2$ were chosen as model salts to evaluate the effects of ionic strength on the uptake of

Cr(VI) ions by HMOS. For this purpose; the Cr(VI) solutions at an initial concentration of 230 mg L^{-1} (at initial pH of 2.5) containing 0.05 g HMOS were treated with NaCl and BaCl$_2$ solutions in the concentration range of 0.05-0.5 M, separately at optimized equilibrium time.
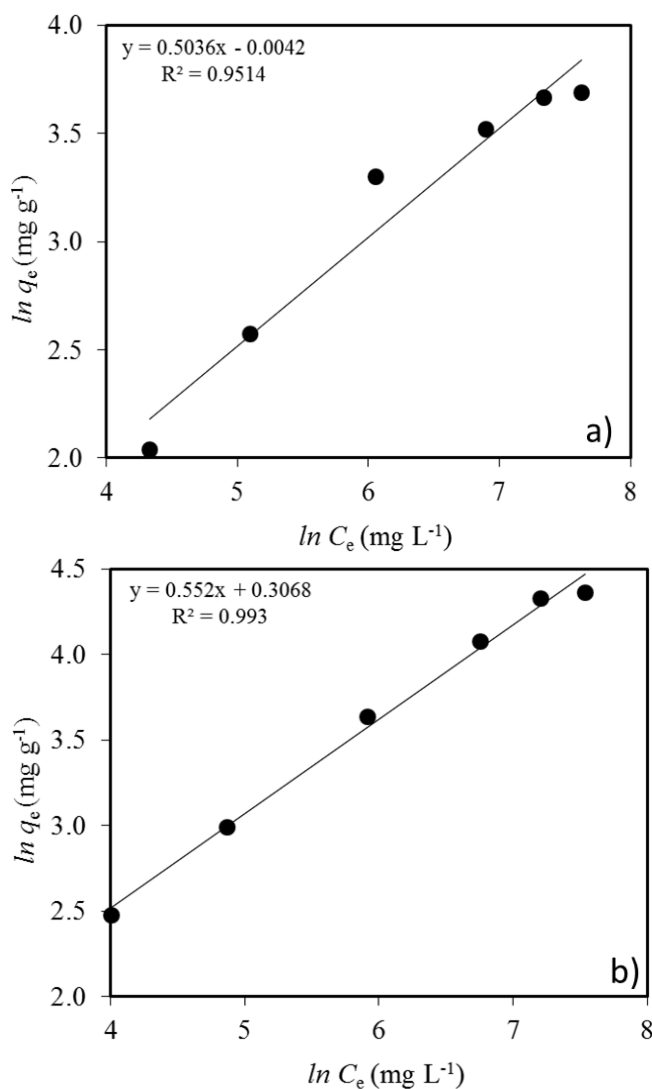
Figure 7. Freundlich isotherm model plotted for a) NOS b) HMOS

By increasing the NaCl and BaCl$_2$ concentrations from 0.05 M to 0.50 M; the Cr(VI) adsorption efficiency on HMOS decreased from 19.8 mg g^{-1} to 10.14 mg g^{-1} and from 14.12 mg g^{-1} to 7.66 mg g^{-1}, respectively (Fig. 8). It is clearly seen that a significant decrease in Cr(VI) adsorption amount occurs by increasing the salt concentration. This decrease in Cr(VI) adsorption as a result of the increase in salt concentration is thought to be caused by two reasons: i) The competition effect of salt anions (Cl$^-$) with Cr(VI) ions which present in an anionic form in aqueous solution to adhere the active adsorption surfaces of HMOS. ii) The screening of the

electrostatic interaction between the Cr(VI) ions and the active adsorption sites of the HMOS due to the presence of ions in the adsorption medium [41,42].

Table 2. Comparison of the Cr(VI) uptake capacities of the different sorbents in the literature.

Adsorbent	Adsorption capacity (mg g^{-1})	Reference
Cetylpyridinium chloride modified montmorillonite	43.84	[31]
Magnetic phoenix tree leaves-derived biochar composite	55.0	[32]
Chemically modified date pits	82.63	[5]
Chemically modified olive stone	53.31	[5]
Fe$_3$O$_4$@ chitosan composite	21.04	[33]
Longan seed activated carbon	35.02	[34]
Apple peels activated carbon	36.01	[35]
Waste newspaper	59.88	[36]
Almond shell	3.4	[37]
HCl treated sawdust	6.34	[38]
Eucalyptus camaldulensis sawdust	35.58	[39]
Natural oak sawdust	48.07	This work
H$_2$SO$_4$ modified oak sawdust	100.0	This work
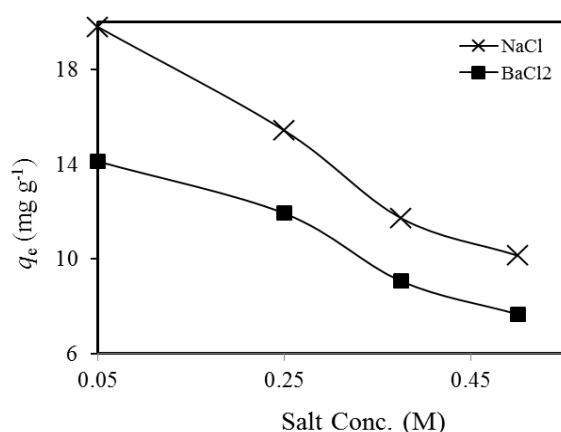
Figure 8. Effect of salt concentration on the adsorption of Cr(VI) ions onto HMOS (initial Cr(VI) concentration: 230 mg L^{-1}; initial pH: 2.5; HMOS concentration: 5.0 g L^{-1}, contact time: 240 min).

4.   Conclusions

In the present research, the usage of the waste material, H$_2$SO$_4$ modified oak sawdust (HMOS), to remove Cr(VI) ions from waters and wastewaters has been evaluated. Although there are some studies in the literature that natural or modified oak sawdust have been used as sorbents for the uptake of different pollutants from aqueous media, the H$_2$SO$_4$ modified oak sawdust has been used for the first time in the removal of Cr(VI) ions in this investigation. The experimental results indicated that the process is highly pH-dependent and the optimum Cr(VI) uptake was observed at initial solution pH 2.5. The

equilibrium was reached within 240 min of shaking time. Although the presence of other ions (Na$^+$, Cl$^-$, Ba^{2+}) in aqueous solutions has remarkable effects on Cr(VI) adsorption, approximately in the rate of 100% of adsorption efficiency has been achieved under the optimized conditions. The equilibrium adsorption data have been evaluated in terms of Langmuir and Freundlich isotherm models and both model fitted well to the experimental data which indicating the homogeneous and heterogeneous distribution of the active adsorption sites on the natural oak sawdust (NOS) and HMOS surface. The maximum adsorption capacities of NOS and HMOS have been obtained as 48.07 and 100.0 mg g^{-1}, respectively with the application of the Langmuir isotherm model. As a result, it has been concluded that the HMOS appears to be an effective, low cost and promising adsorbent for the removal of Cr(VI) ions as compared to many other adsorbents previously reported in the literature.

References

[1] J. Wang, D. Zhang, S. Liu, C. Wang, Enhanced removal of chromium (III) for aqueous solution by EDTA modified attapulgite: Adsorption performance and mechanism, Sci Total Environ, 720, 2020, 137391.

[2] M. Kazemi, M. Jahanshahi, M. Peyravi, Hexavalent chromium removal by multilayer membrane assisted by photocatalytic couple nanoparticle from both permeate and retentate, J Hazard Mater, 344, 2018, 12-22.

[3] Z. Zhao, H. An, J. Lin, M. Feng, V. Murugadoss, T. Ding, H. Liu, Q. Shao, X. Mai, N. Wang, Progress on the photocatalytic reduction removal of chromium contamination, Chem Rec, 19, 2019, 873-882.

[4] L. Liu, X. Liu, D. Wang, H. Lin, L. Huang, Removal and reduction of Cr(VI) in simulated wastewater using magnetic biochar prepared by co-pyrolysis of nano-zero-valent iron and sewage sludge, J Clean Prod, 257, 2020,120562.

[5] C. Mangwandi, T.A. Kurniawan, A.B. Albadarin, Comparative biosorption of chromium (VI) using chemically modified date pits (CM-DP) and olive stone (CM-OS): Kinetics, isotherms and influence of co-existing ions, Chem Eng Res Des, 156, 2020, 251-262.

[6] L. Qin, L. He, W. Yang, A. Lin, Preparation of a novel iron-based biochar composite for removal of hexavalent chromium in water, Environ Sci Pollut, R 27, 2020, 9214-9226.

[7] Guidelines for Drinking-Water Quality (3. edition), 2006, Geneva: World Health Organization,

[8] M. Mohsen-Nia, P. Montazeri, H. Modarress, Removal of Cu^{2+} and Ni^{2+} from wastewater with a chelating agent and reverse osmosis processes, Desalination, 217, 2007, 276-281.

[9] K.Y. Chen, Y.M. Tzou, Y.T. Chan, J.J. Wu, H.Y. Teah, Y.T. Liu, Removal and simultaneous reduction of Cr(VI) by organo-Fe(III) composites produced during coprecipitation and coagulation processes, J Hazard Mater, 376, 2019, 12-20.

[10] R. Hans, G. Senanayake, L.C.S. Dharmasiri, J.A.P. Mathes, D.J. Kim, A preliminary batch study of sorption kinetics of Cr(VI) ions from aqueous solutions by a magnetic ion exchange

(MIEX) resin and determination of film/pore diffusivity, Hydrometallurgy, 164, 2016, 208-218.

[11] M.R. Abukhadra, A. Adlii, B.M. Bakry, Green fabrication of bentonite/chitosan@cobalt oxide composite (BE/CH@Co) of enhanced adsorption and advanced oxidation removal of Congo red dye and Cr(VI) from water, Int J Biol Macromol, 126, 2019, 402-413.

[12] D. Ozdes, A. Gundogdu, B. Kemer, C. Duran, M. Kucuk, Assessment of kinetics, thermodynamics and equilibrium parameters of Cr(VI) biosorption onto *Pinus brutia* Ten, Can J Chem Eng, 92, 2014, 139-147.

[13] D. Ozdes, C. Duran, Equilibrium, Kinetics, and Thermodynamic Evaluation of Mercury (II) Removal from Aqueous Solutions by Moss (*Homalothecium sericeum*) Biomass, Environ Prog Sustain, 34, 2015, 1620-1628.

[14] F. Gode, E.D. Atalay, E. Pehlivan, Removal of Cr(VI) from aqueous solutions using modified red pine sawdust, J Hazard Mater, 152, 2008, 1201-1207.

[15] R.R. Karri, J.N. Sahu, B.C. Meikap, Improving efficacy of Cr(VI) adsorption process on sustainable adsorbent derived from waste biomass (sugarcane bagasse) with help of ant colony optimization, Ind Crop Prod, 143, 2020, 111927.

[16] Y. He, S. Han, H. Lin, Y. Dong, Microwave-assisted modification of corncob with trimethylammonium chloride for efficient removal of Cr(VI): Preparation, Characterization, and Mechanism, Water Air Soil Poll, 231, 2020, 137.

[17] S. Sugashini, K.M.M.S. Begum, Optimization using central composite design (CCD) for the biosorption of Cr(VI) ions by cross linked chitosan carbonized rice husk (CCACR), Clean Technol Envir, 15, 2013, 293-302.

[18] R. Saha, K. Mukherjee, I. Saha, A. Ghosh, S.K. Ghosh, B. Saha, Removal of hexavalent chromium from water by adsorption on mosambi (*Citrus limetta*) peel, Res Chem Intermediat, 39 (5), 2013, 2245-2257.

[19] Z.A. Al-Othman, R. Ali, M. Naushad, Hexavalent chromium removal from aqueous medium by activated carbon prepared from peanut shell: Adsorption kinetics, equilibrium and thermodynamic studies, Chem Eng J, 184, 2012, 238-247.

[20] I. Enniya, L. Rghioui, A. Jourani, Adsorption of hexavalent chromium in aqueous solution on activated carbon prepared from apple peels, Sustain Chem Pharm, 7, 2018, 9-16.

[21] H. Lata, V.K. Garg, R.K. Gupta, Sequestration of nickel from aqueous solution onto activated carbon prepared from *Parthenium hysterophorus* L., J Hazard Mater, 157, 2008, 503-509.

[22] İ. Yıldırım, Sulu Çözeltilerden Ağır Metal İyonlarının Uzaklaştırılmasında Doğal ve H₂SO₄ ile Modifiye Edilmiş Meşe Talaşının Kullanılabilirliğinin Araştırılması, Master Thesis, Gümüşhane University, Institute of Science, 2018.

[23] Standard Methods for the Examination of Water and Wastewater (18. edition), 1985, Washington DC. American Public Health Association.

[24] H.P. Boehm, Surface oxides on carbon and their analysis: A critical assessment, Carbon, 40, 2002, 145-149.

[25] Y. Chen, B. Wang, J. Xin, P. Sun, D. Wu, Adsorption behavior and mechanism of Cr(VI) by modified biochar derived from *Enteromorpha prolifera*, Ecotox Environ Safe, 164, 2018, 440-447.

[26] R.D.C. Soltani, M. Safari, A. Maleki, R. Rezaee, P. Teymouri, S.E. Hashemi, R. Ghanbari, Y. Zandsalimi, Preparation of chitosan/bone char/Fe₃O₄ nanocomposite for adsorption of hexavalent chromium in aquatic environments, Arab J Sci Eng, 43, 2018, 5799-5808.

[27] N. Rajamohan, M. Rajasimman, M. Dilipkumar, Parametric and kinetic studies on biosorption of mercury using modified *Phoenix dactylifera* biomass, J Taiwan Inst Chem E, 45, 2014, 2622-2627.

[28] I. Langmuir, The adsorption of gases on plane surfaces of glass, mica and platinum, J Am Chem Soc, 40, 1918, 1361-1403.

[29] H.M.F. Freundlich, Über die adsorption in lösungen, Z Phys Chem, 57, 1906, 385-470.

[30] K.R. Hall, L.C. Eagleton, A. Acrivos, T. Vermeulen, Pore- and solid-diffusion kinetics in fixed-bed adsorption under constant-pattern conditions, Ind Eng Chem Fund, 5, 1966, 212-223.

[31] S. Liu, M. Chen, X. Cao, G. Li, D. Zhang, M. Li, N. Meng, J. Yin, B. Yan, Chromium (VI) removal from water using cetylpyridinium chloride (CPC)-modified montmorillonite, Sep Purif Technol, 241, 2020, 116732.

[32] S. Liang, S. Shi, H. Zhang, H. Qiu, W. Yu, M. Li, Q. Gan, W. Yu, K. Xiao, B. Liu, One pot solvothermal synthesis of magnetic biochar from waste biomass: Formation mechanism and efficient adsorption of Cr(VI) in an aqueous solution, Sci Total Environ, 695, 2019, 133886.

[33] W.C. Yang, Q.-Z. Tang, S.Y. Dong, L.Y. Chai, H.Y. Wang, Single-step synthesis of magnetic chitosan composites and application for chromate (Cr(VI)) removal, J Cent South Univ, 23, 2016, 317-323.

[34] J. Yang, M. Yu, W. Chen, Adsorption of hexavalent chromium from aqueous solution by activated carbon prepared from longan seed: Kinetics, equilibrium and thermodynamics, J Ind Eng, Chem 21, 2015, 414-422.

[35] I. Enniya, L. Rghioui, A. Jourani, Adsorption of hexavalent chromium in aqueous solution on activated carbon prepared from apple peels, Sustain Chem Pharm, 7, 2018, 9-16.

[36] M.H. Dehghani, D. Sanaei, I. Ali, A. Bhatnagar, Removal of chromium (VI) from aqueous solution using treated waste newspaper as a low-cost adsorbent: Kinetic modeling and isotherm studies, J Mol Liq, 215, 2016, 671-679.

[37] E. Pehlivan, T. Altun, Biosorption of chromium (VI) ion from aqueous solutions using walnut, hazelnut and almond shell, J Hazard Mater, 155, 2008, 378-384.

[38] R. Khalid, Z. Aslam, A. Abbas, W. Ahmad, N. Ramzan, R. Shawabkeh, Adsorptive potential of *Acacia nilotica* based adsorbent for chromium (VI) from an aqueous phase, Chin J Chem Eng, 26, 2018, 614-622.

[39] H. Haroon, T. Ashfaq, S.M.H. Gardazi, T.A. Sherazi, M. Ali, N. Rashid, M. Bilal, Equilibrium kinetic and thermodynamic studies of Cr(VI) adsorption onto a novel adsorbent of *Eucalyptus camaldulensis* waste: Batch and column reactors, Korean J Chem Eng, 33(10), 2016, 2898-2907.

[40] A. Kamari, S.N.M. Yusoff, F. Abdullah, W.P. Putra, Biosorptive removal of Cu(II), Ni(II) and Pb(II) ions from aqueous solutions using coconut dregs residue: Adsorption and characterization studies, J Environ Chem Eng, 2, 2014, 1912-1919.

[41] N. Rajamohan, M. Rajasimman, M. Dilipkumar, Parametric and kinetic studies on biosorption of mercury using modified *Phoenix dactylifera* biomass, J Taiwan Inst Chem E, 45, 2014, 2622-2627.

[42] C.P. Tso, C.M. Zhung, Y.H. Shih, Y.M. Tseng, S.C. Wu, R.A. Doong, Stability of metal oxide nanoparticles in aqueous solutions, Water Sci Technol, 61, 2010, 127-133.

Preparation of cobalt oxide/gold nanoparticle modified glassy carbon electrode for electrochemical detection of dopamine

Ceren Kuşçu[1] (ID), K. Volkan Özdokur[2*] (ID), Süleyman Koçak[3] (ID), F. Nil Ertaş[1] (ID)

[1]Ege University, Faculty of Science, Department of Chemistry, İzmir, Turkey
[2]Erzincan Binali Yıldırım University, Faculty of Art & Science, Department of Chemistry, Erzincan, Turkey
[3]Manisa Celal Bayar University, Faculty of Art & Science, Department of Chemistry, Manisa, Turkey

Abstract

This study deals with electrochemical preparation of cobalt oxide modified glassy carbon electrodes decorated with gold nanoparticles as an effective platform for dopamine (DA) detection. The experimental parameters affecting the oxidation signal of DA by square wave voltammetry have been evaluated. Under optimal conditions, developed sensor exhibited a linear response towards to DA in the concentration range of 6.00×10^{-8} to 7.15×10^{-6} M. The detection and quantification limits were calculated as 2.0×10^{-8} and 6.0×10^{-8} M, respectively. The repeatability and reproducibility of the electrode were calculated as 13.2 and 16.1% for 6.5×10^{-7} M (N=5), respectively. Finally, the sensor was successfully applied for the DA analysis in artificial cerebrospinal fluid, and the mean recovery was found as 105.8 ±6.5% by the standard addition method.

Keywords: Dopamine, square wave voltammetry, cobalt oxide, Au nanoparticles

1. Introduction

Dopamine (3,4-dihydroxyphenethylamine, DA) belongs to catecholamine and phenethylamine families. From the chemical point of view, DA is an amine that can be produced by decarboxylation of L-Dopa. DA is an important neurotransmitter and plays a number of significant roles in the human brain and body [1]. It is responsible for communications of nerve cells and plays a major role in reward-motivated behavior [2].

There are several distinct dopamine pathways in our brain and the level and neuronal activity of DA is increased by most reward and addictive drug types, respectively. Other dopamine systems are responsible for motor control and in releasing of other important hormones [3]. On the other hand, an abnormal level of DA has been found related to some neurological disorders such as schizophrenia, Parkinson's and Huntington's diseases [2]. Thus, it is very crucial to detect and quantitate the dopamine in biological samples such as brain fluids, plasma, and urine.

Various analytical methods have been described in the literature including colorimetric and fluorometric methods [4-6], gas chromatography with tandem mass detection [7,8], high performance liquid chromatography coupled with various detectors [9-11], chemiluminescence [12]. These methods, however, have some drawbacks being labor-intensive or time-consuming, and most of them require expensive instrumentation. Electrochemical analysis methods, on the other hand, are very popular since very sensitive and selective methods can be developed at a very low cost. Amperometric [13,14] and voltammetric [15-17] methods have been developed for DA detection in micromolar levels in the presence of ascorbic acid. However, the oxidation peak of the dopamine is prone to the interference of electroactive matrix constituents and therefore, the electrode surfaces have been modified with conductive polymers, carbonaceous materials, conductive polymers, metal nanoparticles, and/or metal oxides.

Recent studies utilize square wave voltammetry for DA detection at carbon-based electrodes including glassy carbon disk modified with reduced graphene oxide for human serum samples [18], nitrogen-doped graphene modified glassy carbon electrode (GCE) [19] or carbon-fiber microelectrodes suitable for in-vivo analysis [20]. Carbon-based electrodes modified with cobalt phthalocyanine complexes have been widely used for the detection of catecholamines but weakly adsorbed complexes suffer from the low conductivity [21]. Carbonaceous nanomaterials, particularly graphenes are often employed as conducting supports on the electrode surfaces for achieving a selective and sensitive DA determination [22, 23].

Metal oxides, on the other hand, are becoming more popular due to their unique electrochemical properties, chemical stability, and low-cost. However, some metal oxides may fail to show the desired catalytic activity and this limitation can be eliminated by decorating the transition metal oxide film with noble metallic nanoparticles. This hyper d-hypo d element combination provides a synergistic effect and enhances the catalytic activity [24].

Among the transition metals, cobalt and its oxide species along with their nanomaterials have drawn a great deal of attention due to their outstanding electronic, optical, magnetic, and catalytic properties [25].

Various types of cobalt oxides with different catalytic performances have been synthesized and used for catalysis and analytical purposes [26].

Their performance is not only dependent on the structure of the cobalt oxide but, also depends on its fabrication process [27, 28]. Electrochemical deposition is probably the best solution for controlling the catalytic properties where the potential is either cycled between two limits suitable for the growth of the metal oxide film or applied in the form of pulses between the limits for certain duration times. The latter technique, also known as the pulsed deposition, results in a more ordered film structure with better catalytic activity in both directions [29].

Here we report a simple, cheap, and green methodology for the synthesis of Au nanoparticles decorated cobalt oxide film for dopamine detection in trace levels. The surface morphology of the electrode was characterized by using Field-Effect Scanning Electron Microscopy (FESEM) and then, the analytical performance of the electrode was investigated. The method was applied to the determination of dopamine at nanomolar levels in artificial cerebrospinal fluid.

2. Materials and method

2.1. Reagents and apparatus

Analytical grade reagents and ultrapure water obtained from Milli Pore (with 18.2 MΩ resistivity) were used throughout the study. Cobalt (II) chloride hexahydrate, potassium gold (III) chloride, dopamine hydrochloride, ascorbic acid, uric acid, sodium chloride, potassium ferricyanide, potassium ferrocyanide, sodium hydrogen carbonate, potassium chloride, sodium dihydrogen phosphate, magnesium chloride, glucose, calcium chloride, acetic acid, chloroacetic acid, hydrochloric acid, phosphoric acid, boric acid, and sodium hydroxide were purchased from Sigma Aldrich from Germany. Britton Robinson (BR) buffer consisted of 0.08 M acetic, phosphoric, and boric acid each, the final pH was adjusted with 3 M NaOH solution. Chloroacetic acid-acetate buffer solution (CAA-Ac) was prepared from 0.1 M CAA and 0.1 M acetic acid and pH was adjusted to pH 4.0 with 3.0 M NaOH.

Artificial cerebrospinal fluid was prepared by mixing 119 mM NaCl, 26.2 mM NaHCO$_3$, 2.5 mM KCl, 1 mM NaH$_2$PO$_4$, 1.3 mM MgCl$_2$, 10 mM glucose and 2.5 mM CaCl$_2$ dissolved in ultrapure water and stored at 4°C. This solution was stable for 3-4 weeks.

Electrochemical measurements were performed by using Autolab PGSTAT101 (Metrohm, Netherland) voltammetric analyzer with a three-electrode system consisting of Ag/AgCl (sat. KCl) as the reference electrode, Pt wire as the counter electrode and GCE (BASi, 3 mm diameter and a surface area of 0.07 cm^2) as the working electrode. The inspection of the modified surfaces was made by using an FEI Quanta 450 FESEM that was used for SEM analysis.

2.2. Electrode modification procedure

Prior to each experiment, the GCE was polished with 0.3-micron alumina slurry and treated with water and ethanol mixture in an ultrasonic bath. After rinsing with ultrapure water, the electrode was dipped into a 0.05 M Co(II) solution in pH 4.0 CAA/Acetate buffer. The GCE surfaces have been modified with metal oxide film by cycling the potential in the range of 0.5 - -1.2 V for 5 times at a scan rate of 75 mV s^{-1}. Then, the obtained electrode (CoO$_x$/GCE) was immersed into a 1×10^{-4} M Au(II) solution prepared in 0.1 M HCl solution and further deposition was achieved by cycling the potential

between 0.0 and 1.2 V at a rate of 75 mV s^{-1} for 15 times. The electrode obtained by this means was denoted as Au/CoO$_X$/GCE.

2.3. Electrochemical measurements

The electrochemical behavior of dopamine (DA) was tested by using voltammetric techniques in the potential range of 0 to 1.0 V at different scan rates. Linear Sweep Voltammetry (LSV), Differential Pulse Voltammetry (DPV), Square Wave Voltammetry (SWV) techniques were utilized for this purpose. Instrumental parameters of SWV were as follows; frequency (*f*) 25 Hz, pulse amplitude (ΔE) 20 mV, and staircase step (ΔEs) 5 mV and the potential between 0.00 and 1.00 V. Efficient Surface Area (ESA) calculation was made from the cyclic voltammetric measurements carried out in 2.5×10^{-3} M K$_3$[Fe(CN)$_6$] and K$_4$[Fe(CN)$_6$] solution containing 0.1 M KCl.

3. Results and discussion

3.1. Characterization

The inspection of the surface morphology of the modified electrode was made by the FESEM measurements along with the Energy Dispersive Spectroscopy (EDAX) spectra. A smooth surface of the bare GCE was clearly seen in Fig. 1A. After the modification with CoOx on GCE, irregular spherical deposits were observed in the range of 70-100 nm and the chemical composition of the deposit was proven with the EDAX results (Fig. 1B). Fig. 1C depicted the closer image of Au/CoOx/GCE and the Au nanoparticles were about 70 nm-sized and homogenously distributed onto the CoOx/GCE surface.

Element	Atomic Percent (%)
Co	3.84
O	17.10
Au	7.03
C	70.30
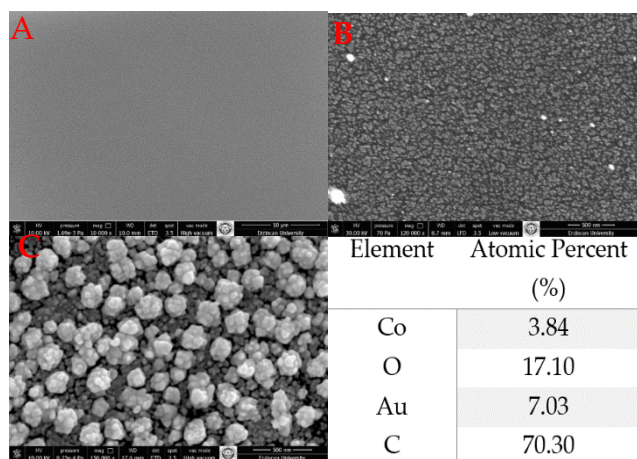
Figure 1. SEM images of A) Bare GCE, B) CoOx /GCE, C) Au/CoOx/GCE electrode and EDAX result of Au/CoOx/GCE electrode.

The electrochemical characterization of the modified surfaces was accomplished by recording the cyclic voltammograms. A linear correlation was observed between anodic peak current observed for 2.5 mM K$_3$Fe(CN)$_6$ and K$_4$Fe(CN)$_6$ solution and the square root of the scan rate, indicating the diffusion-controlled electrode process (Supplementary Figure 1). The electroactive surface area (ESA) is calculated by applying the data obtained above to the Randles-Sevcik equation (Eq. 1).

$$I_p = (2.69 \times 10^5)n^{3/2}AD^{1/2}C^*v^{1/2} \qquad (1)$$

Here; I_P is the anodic peak current of ferrocyanide, n is the numbers of the electron processed in redox reaction (n=1), *A* is the electroactive surface area (cm^2), *D* is the diffusion coefficient (6.7×10^{-6} cm^2 s^{-1} at 25°C), C^* is the concentration of K$_3$Fe(CN)$_6$ (2.5 mM) and ν is scan rate of potential scan (V s^{-1}) [30]. The ESA of GCE, CoOx/GCE, and Au/CoOx/GCE were calculated as 0.05, 0.08, 0.13 cm^2, respectively.

3.2. Electrochemical behavior of DA

After the characterization of the Au/CoOx/GCE electrode, well-known voltammetric techniques have been applied for revealing the electrochemical behavior of DA. CV, LSV, DPV, and SWV measurements recorded in 6.52×10^{-6} M DA in pH 2.00 BR buffer and on the basis of the current signal, the SWV has resulted in the most sensitive results (Data not have shown). Therefore, further experiments were performed with the SWV technique while the CV was utilized for the optimization studies.

The comparison of step-by-step modified electrodes is given in Fig. 2. DA has displayed an oxidation peak at 0.57 V with a peak current of 7.0 μA on the bare GCE surface. After the modification with CoOx (CoOx/GCE), DA peak was shifted to 0.51 V and the peak current has arisen to 10.3 μA. Further decoration with AuNP (Au/CoOx/GCE) has led to a 30 mV potential shift to the negative direction while the peak current has increased to 21.0 μA. Gold nanoparticles decorated bare GCE (Au/GCE) were also prepared for comparison, and this electrode has exhibited an oxidation peak at 0.53 V with a peak current of 13.0 μA. The enhancement in the peak current can be attributed to the synergistic effect between CoOx and AuNP due to the hyper d-hypo d attraction.

3.3. Electrochemical characterization of DA and optimization studies

The effects of the experimental parameters on the DA signal were investigated by using 6.52×10^{-6} M DA. The initial parameter was chosen the pH of the electrochemical cell and this parameter was studied in the pH range of 2.0 - 11.0 by using BR buffer.
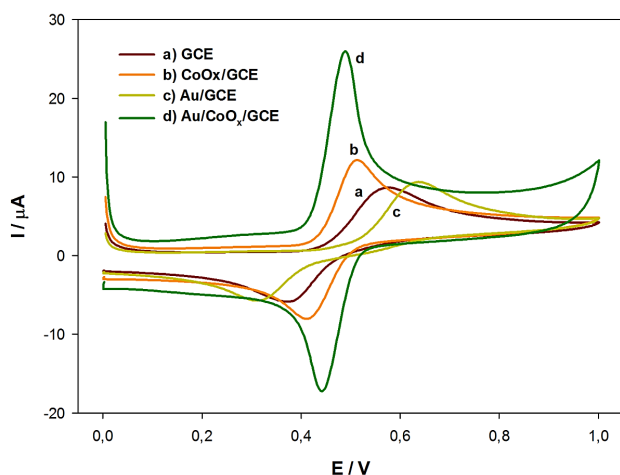
Figure 2 The comparative CV voltammograms of step-by-step modified electrodes for 6.52×10^{-6} M DA in pH 2.0 BR buffer.

The results were given in Fig. 3. The anodic peak current of DA was increased by increasing pH up to 6.0, after this pH the anodic peak current was diminished. The optimum pH was designated as 6.0 and used for further studies. On the other hand, the oxidation peak potential (E_{ox}) has shifted to a negative direction with increasing medium pH, meaning the hydronium ion has participated in the electrochemical process.
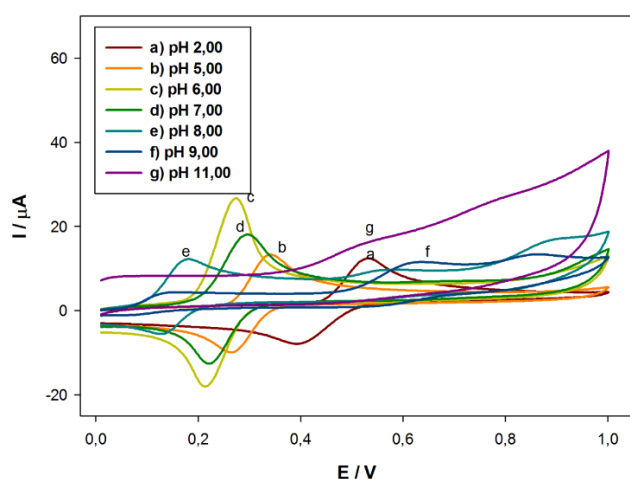
Figure 3. Effect of measurement medium pH on 6.52×10^{-6} M DA signal.

The relation between pH and E_{ox} was found linear with an equation of $E_P = -0.063$ pH $+ 0.6548$ in the range of 2 to 8. The slope of the pH curve is close to the identical value of 0.059 V, indicating the equal

number of protons and electron transferred in the electrochemical process [31]. Further electrochemical information for the DA oxidation mechanism was obtained by changing the CV scan rate in the range of 5 to 1000 mV s^{-1}. The relationship between oxidation peak current (I_{pa}) of 6.52×10^{-6} M mol L^{-1} DA and the square root of the scan rate ($v^{1/2}$) was found linear with an equation of $I_{pa}= 3.657$ (SR)$^{1/2}$ - 8.07 and correlation coefficient of (R^2) 0.9901. These results were indicating that mass transportation was controlled by diffusion.

The thickness of the deposits grown on the electrode is generally related to the cell concentration of precursor ions, deposition cycle numbers, and scan rate. Accordingly, Co(II) concentration was varied between 0.005 - 0.5 M and 0.05 M was found as an optimal value (Supplementary Figure 2). Another parameter is the deposition scan rate applied during the CoOx deposition. The scan rate was changed between 5 to 100 mV s^{-1} and 75 mV s^{-1} was given the best result (Supplementary Figure 3). Finally, the repetitive cycle number is another important parameter to film growth, and therefore the thickness can be controlled by changing this parameter. Repetitive cycle number was started from 2 and increased up to 40 cycles and the voltammograms have revealed that the oxidation peak current of DA has given a maximum at 5 cycles, after this value the oxidation peak current has reached a plateau (Supplementary Figure 4). Therefore, consecutive five cycles were used for further studies. Similar parameters were investigated for Au nanoparticle deposition and overall results were summarized in Table 1.

Table 1. Optimal condition for CV deposition of CoOx and Au.

Parameter		Range	Optimum value
Cell Conc. (M)	Co (II)	0.005 - 0.5	0.05
	AuCl$_4^-$	-	0.0001
Scan rate (mV s^{-1})	CoOx	5 - 100	75
	AuNP	5 - 100	75
Cycle number	CoOx	2 - 40	5
	AuNP	2 - 20	15

3.4. Analytical characteristics of the method

After the characterization of the modified surface characteristics and electrochemical process of DA, the analytical performance of the developed surfaces was tested. Au/CoOx/GCE electrode was exhibited linear response in the concentration range of 6.0×10^{-8} to 7.15×10^{-6} M DA. The SWV voltammograms and the calibration curve were given Fig. 4 and the linear equation was calculated as $I_P = 526258$ C$_{DA}$ + 0.303 with a correlation coefficient (R^2) of 0.9983.

Signal to noise (S/N) was set to three for the limit of detection (LOD) and five for the limit of quantification (LOQ) and these values were calculated as 20 and 60 nM, respectively. The repeatability (interday, N=5) and reproducibility (intraday, N=5) were determined as relative standard deviation (RSD) and figured out as 13.2 and 16.1% for 6.5×10^{-7} M, respectively.
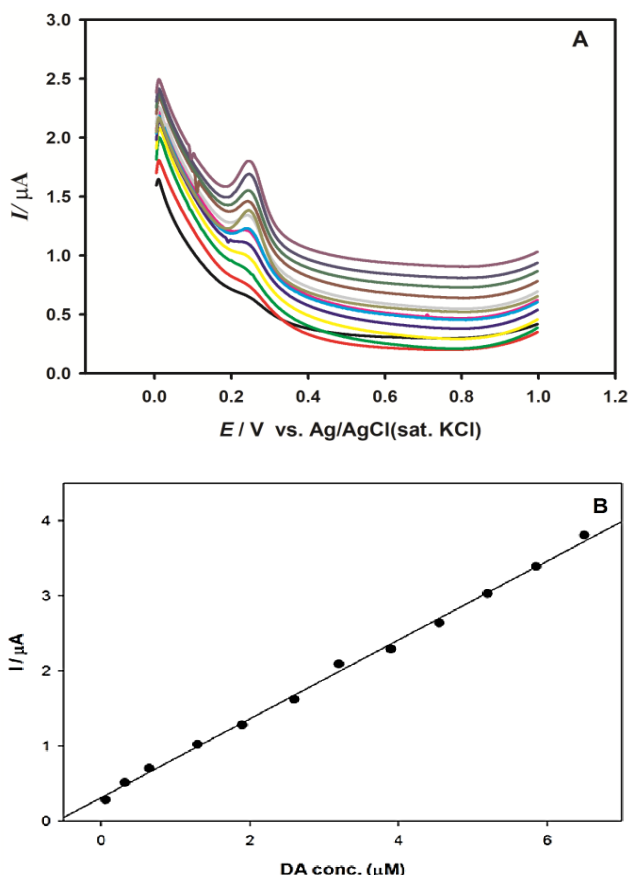
Figure 4. SWV voltammograms of 6.0×10^{-8} to 7.15×10^{-6} M dopamine and the calibration curve.

The accuracy of the calibration curve was tested by analyzing quality control samples with a concentration of 6.5×10^{-7} M and the recovery of the sample was found as 107.3% for this concentration. The possible interference of 1.0 mM of NaCl, NaHCO$_3$, KCl, NaH$_2$PO$_4$, MgCl$_2$, glucose, CaCl$_2$, 50.0×10^{-6} M ascorbic acid, and uric acid was tested. No interference was observed for the 6.5×10^{-7} M DA signal. The stability of the electrode was tested by analyzing 6.5×10^{-7} M DA, and the electrode developed was shown 98% of its initial activity after 50 measurements. The method developed was applied to DA analysis in ACSF by the standard addition method. A satisfactory recovery value (105.8 ± 6.5%) was obtained for 6.5×10^{-7} M DA in ACSF.

The developed sensor performance was compared with the literature studies in Table 2. According to the literature survey, the sensor developed is a good candidate for the trace analysis of DA. The analytical characteristics of the developed sensor were found comparable with the literature in terms of detection limit and linear range.

Table 2. Comparison of AuNPs/CoOx/GCE analytical performance with previous reported electrochemical methods.

Electrode	Technique	Linear Range (μM)	LOD (μM)	Ref.
BCNTs/GCE	DPV	0.02 - 75.00	0.001	[32]
Gr/AuNPs/GCE/	DPV	5.0 - 1000	1.860	[33]
AuNPs/Ch/GCE/	DPV	0.2 - 80	0.120	[34]
Gr/Pt/GCE	Amperometry	0.03-8.13	0.030	[35]
RGO-Pd/GCE	LSV	1-150	0.230	[36]
Methylene blue/ MWCNT/GCE	DPASV	0.4-10	0.200	[37]
AuNPs/CoOx/GCE	SWV	0.06 - 7.15	0.020	This study

(BCNTs: Boron-doped carbon nanotubes, AuNPs: Gold nanoparticles, Gr: Graphene, Ch: Choline, CoOx: Cobalt oxide, MWCNT: multi-walled carbon nanotube, Pt: Platinum, RGO: reduced graphene oxide, Pd: Palladium, DPV: Differential pulse voltammetry, LSV: Linear scan voltammetry, DPASV: Differential pulse anodic stripping voltammetry, SWV: Square wave voltammetry)

4. Conclusion

The present study reported, metal/metal oxide modified electrode for sensitive DA analysis. Au/CoOx/GCE/ electrode was prepared via CV technique and characterized by various methods. Au/CoOx/GCE electrode exhibited a catalytic signal towards DA oxidation. Three-fold current enhancement was obtained while the peak potential shifted 100 mV negative to the negative direction. The synergetic effect between CoOx and AuNP is responsible for the current enhancement due to the hyper-hypo d attraction. The analytical characteristics were found comparable with the literature values.

References

[1] G. Di Chiara, V. Bassareo, Reward system and addiction: What dopamine does and doesn't do, Curr Opin Pharmacol, 7, 2007, 69-76.

[2] D. Meder, D.M. Herz, J.B. Rowe, S. Lehericy, H.R. Siebner, The role of dopamine in the brain - lessons learned from Parkinson's disease, Neuroimage, 190, 2019, 79-93.

[3] A. Bjorklund, S.B. Dunnett, Dopamine neuron systems in the brain: An update, Trends Neurosci, 30, 2007, 194-202.

[4] J. Wang, R. Du, W. Liu, L. Yao, F. Ding, P. Zou, Y. Wang, X. Wang, Q. Zhao, H. Rao, Colorimetric and fluorometric dual-signal determination of dopamine by the use of Cu-Mn-O

microcrystals and C dots. Sensor Actuat B: Chem, 290, 2019, 125-132.

[5] Y. Tao, Y. Lin, J. Ren, X. Qu, A dual fluorometric and colorimetric sensor for dopamine based on BSA-stabilized Au nano clusters, Biosens Bioelectron, 42, 2013, 41-46.

[6] S. Roastami, A. Mehdinia, A. Jabbari, E. Kowsari, R. Niroumand, T.J. Booth, Colorimetric sensing of dopamine using hexagonal silver nanoparticles decorated by task-specific pyridinum based ionic liquid, Sensor Actuat B: Chem, 271, 2018, 64-72.

[7] A. Naccarato, E. Gionfriddo, G. Sindona, A. Tagaralli, Development of a simple and rapid solid phase microextraction-gas chromatography-triple quadrupole mass spectrometry method for the analysis of dopamine, serotonin and norepinephrine in human urine, Anal Chim Acta, 810, 2014, 17-24.

[8] F. Musshoff, P. Schmidt, R. Dettmeyer, F. Priemer, K. Jachau, B. Madea, Determination of dopamine and dopamine-derived (R)-/(S) salsolinol and norsalinol in various human brain areas using solid-phase extraction and gas chromatography/mass spectrometry, Forensic Sci Int, 113, 2000, 359-366.

[9] A. Gottås, Å. Ripel, F. Boix, V. Vindenes, J. Mørland, E.L. Øiestad, Determination of dopamine concentrations in brain extracellular fluid using microdialysis with short sampling intervals, analyzed by ultrahigh performance liquid chromatography tandem mass spectrometry, J Pharmacol Tox Met, 74, 2015,75-79.

[10] M. Oh, E. Huh, M.S. Oh, J. Jeong, S. Hon, Development of a diagnostic method for Parkinson's disease by reverse-phase high-performance liquid chromatography coupled with integrated pulsed amperometric detection, J Pharmaceut Biomed Analysis, 153, 2018, 110-116.

[11] L. Dillen, M. Claeys, W.P.D. Potter, Determination of dopamine-β- hydroxylase in cerebrospinal fluid by high-performance liquid chromatography with electrochemical detection, J Pharmacol, 15, 1986, 51-63.

[12] W. Gao, L. Qi, Z. Liu, S. Majeed, S. A. Kitte, G. Xu, Efficient lucigenin/thiourea dioxide chemiluminescence system and its application for selective and sensitive dopamine detection, Sensor Actuat B, 238, 2017, 468-472.

[13] K. Min, Y.J. Yoo, Amperometric detection of dopamine based on tyrosinase-SWNTs-Ppy composite electrode, Talanta, 80, 2009, 1007-1011.

[14] H. Duan, L. Li, X. Wang, Y. Wang, J. Li, C. Luo, A sensitive and selective chemiluminescence sensor for the determination of dopamine based on silanized magnetic graphene oxide-molecularly imprinted polymer, Spectrochim Acta A, 139, 2015, 374-379.

[15] W.-L. Yeh, Y.-R. Kuo, S.-H. Cheng, Voltammetry and flow-injection amperometry for indirect determination of dopamine, Electrochem Commun, 10, 2008, 66-70.

[16] L. Zhang, T. Norio T., Hasebe, M. Kurihara, T. Kawashima, Flow-injection determination of trace amounts of dopamine by chemiluminescence detection, Talanta, 50, 1999, 677-683.

[17] Y. Sun, Y. Lin, C. Ding, W. Sun, Y. Dai, X. Zhu, H. Liu, C. Luo, An ultrasensitive and ultraselective chemiluminescence aptasensor for dopamine detection based on aptamers modified magnetic mesoporous silica @ graphite oxide polymers, Sensor Actuat B: Chem, 257, 2018, 312-323.

[18] A.M. Granero, G.D. Pierini, S.N. Robledo, M.S. Di Nezio, H. Fernández, Zon, M.A. Simultaneous determination of ascorbic and uric acids and dopamine in human serum samples using three-way calibration with data from square wave voltammetry, Microchem J, 129, 2016, 205-212.

[19] A. Hatefi-Mehrjardi, A. Beheshti-Marnani, N. Askari, Cu^{+2} loaded "zeolite A"/ nitrogen-doped graphene as a novel

hybrid for simultaneous voltammetry determination of carbamazepine and dopamine, Mater Chem Phy, 225, 2019, 137-144.

[20] Y. Oh, M.L. Heien, C. Park, Y.M. Kang, J. Kim, S.L. Boschen, H. Shin, H.U, Cho, C.D. Blaha, K.E. Bennet, H.K. Lee, S.J. Jung, I.Y. Kim, K.H. Lee, D.P. Jang, Tracking tonic dopamine levels in vivo using multiple cyclic square wave voltammetry, Biosens Bioelectron, 121, 2018, 174-182.

[21] J.H. Zagal, S. Griveau, J.F. Silva, T. Nyokong, F. Bedioui, Metallophthalocyanine-based molecular materials as catalysts for electrochemical reactions, Coordin Chem Rev, 254, 2010, 2755-2791.

[22] J. Yang, D. Mu, Y. Gao, J. Tan, A. Lu, D. Ma, Cobalt phthalocyanine-graphene complex for electro-catalytic oxidation of dopamine, J Nat Gas Chem, 21, 2012, 265-269.

[23] N. Diab, D.M. Morales, C. Andronescu, M. Masoud, W. Schuhmann, A sensitive and selective graphene/cobalt tetrasulfonated phthalocyanine sensor for detection of dopamine, Sensor Actuat B: Chem, 285, 2019, 17-23.

[24] K.V. Özdokur, S. Koçak, F.N. Ertaş, Nanostructures Metal-Metal oxides and Their Electrocatalytic Applications. Chapter in Advanced coating Materials, Editors: L. Li, Q. Yang, 2019, Wiley Interscience.

[25] Q. Wang, W. Hu, Y. Huang, Nitrogen doped graphene anchored cobalt oxides efficiently bi-functionally catalyze both oxygen reduction reaction and oxygen revolution reaction, Int J Hydrogen Energ, 4, 2017, 5899-5907.

[26] I.G. Casella, M. Contursi, Cobalt oxide electrodeposition on various electrode substrates from alkaline medium containing Co-gluconate complexes: A comparative voltammetric study, J Solid State Electr, 1, 2012, 3739-3746.

[27] R. Hallaj, K. Akhtari, A. Salimi, S. Soltanian, Controlling of morphology and electrocatalytic properties of cobalt oxide nanostructures prepared by potentiodynamic deposition method, Appl Surf Sci, 276, 2013, 512-520.

[28] C. Kuşçu, K.V. Özdokur, S. Koçak, F.N. Ertaş, Development of cobalt oxide film modified electrode decorated with platinum nanoparticles as a biosensing platform for phenol, Int J Environ An Ch, 14, 2019, 1-7.

[29] K.V. Özdokur, A.Y. Tatlı, B. Yılmaz, S. Kocak, F.N. Ertaş, Development of pulse deposited manganese and molybdenum oxide surfaces decorated with platinum nanoparticles and their catalytic application for formaldehyde oxidation, Int J Hydrogen Energ, 41, 2016, 5927-5933.

[30] Ç.C. Koçak, Poly(taurine-glutathione)/carbon nanotube modified glassy carbon electrode as a new levofloxacin sensor, Electroanal, 31(8), 2019, 153-1544.

[31] Ş. Ulubay, Z. Dursun, Cu nanoparticles incorporated polypyrrole modified GCE for sensitive simultaneous determination of dopamine and uric acid, Talanta, 80(3), 2010, 1461-1466.

[32] C. Deng, J. Chen, M. Wang, C. Xiao, Z. Nie, S. Yao, A novel and simple strategy for selective and sensitive determination of dopamine based on the boron-doped carbon nanotubes modified electrode, Biosens Bioelectron, 24, 2009, 2091-2094.

[33] J. Li, J. Yang, Z. Yang, Y. Li, S. Yu, Q. Xu, X. Hu, Graphene-Au nanoparticles nanocomposite film for selective electrochemical determination of dopamine, Anal Methods, 4, 2012, 1725-1728.

[34] P. Wang, Y. Li, X. Huang, L. Wang, Fabrication of layer-by-layer modified multilayer films containing choline and gold nanoparticles and its sensing application for electrochemical determination of dopamine and uric acid, Talanta, 73, 2007, 431-437.

[35] C.L. Sun, H.-H. Lee, J.-M. Yang, C.-C. Wu, The simultaneous electrochemical detection of ascorbic acid, dopamine, and uric acid using graphene/size-selected Pt nanocomposites, Biosens Bioelectron, 26, 2011, 3450-3455.

[36] S. Palanisamy, S. Ku, S.-M. Chen, Dopamine sensor based on a glassy carbon electrode modified with a reduced graphene oxide and palladium nanoparticles composite, Microchim Acta, 180, 2013, 1037-1042.

[37] S.L. Yang, G. Li, R. Yang, M.M. Xia, Qu, L.B. Simultaneous voltammetric detection of dopamine and uric acid in the presence of high concentration of ascorbic acid using multi-walled carbon nanotubes with methylene blue composite film-modified electrode, J Solid State Electr, 15, 2011, 1909-1918.

Adsorption of reactive Orange 16 by Amberlyst A21: Isotherm and kinetic investigations

Murat Basar [iD], Hülya Silah* [iD]

Bilecik Şeyh Edebali University, Faculty of Art & Science, Department of Chemistry, 11210, Bilecik, Turkey

Abstract

Recently, Amberlyst A21 has attracted much attention because of its highly selective feature as well as its specific chemical and physical structure. In the present work, Amberlyst A21 polystyrene resin was used as a new sorbent for Reactive Orange 16 dye. The experimental conditions i.e. such solution pH, initial Reactive Orange 16 concentration, contact time, and Amberlyst A21 dosage were optimized using by batch adsorption technique. The morphology of surface and functional groups of Amberlyst A21 was investigated by using Scanning Electron Microscopy (SEM) and Fourier Transform Infrared Spectroscopy (FT-IR). The adsorption isotherm data indicate that the Langmuir isotherm model is the best fit model. The calculated maximum Reactive Orange 16 adsorption capacity of Amberlyst A21 was 175.13 mg g^{-1}. The pseudo-first and second-order kinetic models are used to clarify the mechanism of adsorptive removal by Amberlyst A21 in optimal experimental conditions were discussed. The reactive Orange 16 adsorption kinetics and equilibrium data were successfully defined by pseudo-first-order and Langmuir models, respectively. This manuscript currently shows an uncomplicated way of wastewater treatment and a new adsorbent for dye removal which might develop an environmental process based on the use of Amberlyst A21 resin.

Keywords: Adsorbent, isotherms, kinetics, Reactive Orange 16, resin

1. Introduction

Due to the growth of industrialization, a large number of wastewaters containing dyes that are used in various industrial areas is discharged into the environment. The organic pollutants such as dyes, which have led to various serious health and environmental problems, are difficult to be treated owing to they are easily outspreading through air or water into the ground, long-time degradation, and high treatment cost [1,2]. So that various chemical, physical and biological methods, including ozonation [3], advanced oxidation [4], adsorption [5,6], membrane filtration [7], flocculation/coagulation [8], biosorption [9], ion-exchange [10], and photocatalytic degradation [11] are often used to treat of wastewater including dyes and other contaminants. Among these methods, adsorption was so attractive because of convenience and low-cost in application [12]. Nowadays, the adsorption technique is most commonly applied for wastewater purification due to its yield in the

removal of various pollutants too stable for biological methods [13].

Azo dyes, which are characterized by the presence of -N=N- chromophore groups in the complex chemical structure, are widely available textile, plastic, cosmetic, paper, leather, and food industry [14]. Reactive Orange 16 (Fig.1), a synthetic azo compound, is mostly used in various industrial areas. The discharge of wastewater containing Reactive Orange 16 causes serious biotic risk in the environmental media [15].
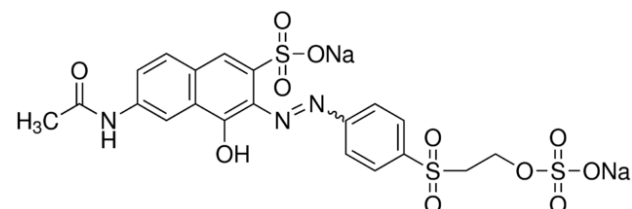

Figure 1. Chemical structure of Reactive Orange 16.

In this paper, Amberlyst A21 resin was selected as the sorbent due to its highly selective properties as

well as its specific chemical and physical structure so; removal of some pollutants as palladium (II) [17], acetic acid [18,19], butyric and oxalic acids [19] sulfate [16], chromium (VI) [20] have been investigated by using Amberlyst A21.

The present manuscript aims to explore the adsorption efficiency of Amberlyst A21 polystyrene resin for the removal of Reactive Orange 16 dye from wastewaters. FT-IR and SEM techniques are used to characterize the structure of Amberlyst A21 resin. The optimal adsorption conditions were defined by the experiments of pH, adsorption time, amount of Amberlyst A21, and initial Reactive Orange 16 concentrations. Langmuir, Freundlich, and Temkin isotherm were utilized to comply with equilibrium adsorption data and evaluate the adsorption behaviour of Reactive Orange 16. In addition, the experimental data were tested with kinetic models to determine the rate-controlling mechanism for the dye adsorption process. In the literature, there are very few studies about the removal of dyes with Amberlyst A21. The recommended removal process for Reactive Orange 16 has superiorities such as a simple way of operation and high efficiency to remove the dye in a short time.

2. Experimental

2.1. Materials
Amberlyst A21 and Reactive Orange 16 dye used for this study were provided from Sigma-Aldrich. Hydrogen chloride (HCl), sodium hydroxide (NaOH), and other chemicals used were of analytical grade from Merck and were used without further purification. All solutions were prepared with deionized water.

2.2. Morphological analysis of adsorbent
Fourier transform infrared spectroscopy (FT-IR) and scanning electron microscopy (SEM) were used to characterize Amberlyst A21. The FT-IR spectroscopy analyses were recorded on Perkin Elmer, Spectrum 100 Model over the range of 400-4000 cm^{-1} with ATR technique in the range resolution of 4 cm^{-1}. Scanning electron microscopy (Zeiss Supra 40 V device) was used to observe the internal and surface morphologies of Amberlyst A21.

2.3. Batch adsorption characteristics of Reactive Orange 16
In adsorption studies, all Reactive Orange 16 solutions were prepared by diluting the stock dye solution (1000 mg L^{-1}) with the appropriate volume of

deionized water. The pH value of aqueous solutions was set with HCl (0.1 M) or NaOH (0.1 M). All adsorption experiments were carried out in 100 mL Erlenmeyer flask with constant agitation at 100 rpm and room temperature (25 °C) for batch experiments. The effects of solution pH (2.0-10.0), Amberlyst A21 dose (0.25-2.00 g L^{-1}), contact times (5-200 minutes), and initial Reactive Orange 16 concentrations (50-300 mg L^{-1}) were investigated for removal process of dye. The concentration of the Reactive Orange 16 dye in aqueous solutions was examined with a UV-Vis spectrophotometer (T80 model-PG Instruments) by measuring the molar absorbance at 494 nm [24]. The equations (1) and (2) can be used to calculate the adsorption capacity (q_e, mg g^{-1}) of adsorbent and removal percentage (R %), respectively;

$$q_e = \frac{(C_0 - C_e)}{m} xV \qquad (1)$$

$$Removal\ (\%) = \frac{(C_0 - C_e)}{C_0} x100 \qquad (2)$$

where m and V are the weight of adsorbent in gram and volume of dye solution in a liter, respectively. C_0 (mg L^{-1}) is the initial dye concentration and C_e (mg L^{-1}) is the dye ion concentration in the adsorption equilibrium state.

2.4. Isotherm and kinetics investigations
The adsorption isotherms and kinetic are crucial investigations in the design of removal systems of pollutants from wastewaters. For the adsorption experiments, three isotherm models, which included Freundlich, Langmuir, and Temkin models were applied to fit the experimental adsorption data. Kinetic models of pseudo-first and pseudo-second-order model were investigated to understand the adsorption behaviour of Reactive Orange 16 onto Amberlyst A21 and to assess the rate of adsorption.

3. Results and discussions

3.1. Morphological analysis
To further analyze the functional groups of the Amberlyst A21 surface, FT-IR spectra were utilized to characterize and described in Fig. 2.

FT-IR spectra obtained from free Amberlyst A21 resin showed (Fig. 2a) specific peaks at 2935 cm^{-1} and 2857 cm^{-1} correspond to C-H bonds stretching of alkane. The peak at 1362 cm^{-1} present in the spectrum (a) related to the C-N stretch in the amine group.

There is also band corresponding to aromatic stretching of C=C located at 1600-1400 cm^{-1}. The vibrations of =C-H bending are in the range of 1000-675 cm^{-1} [21]. In comparison to the spectra of Amberlyst A21 before and after adsorption of Reactive Orange 16, a significant shift in the spectral peaks was observed in 3000-2850 and 1680-1600 cm^{-1}. Also, as seen from Fig. 2, the band was shown at 1456 cm^{-1} before adsorption but after adsorption, this band was shifted to 1493 cm^{-1}. These shifts were occurred owing to the binding of Reactive Orange 16 ions with functional groups of Amberlyst A21. Thus, the changing of wavenumber of peaks confirms the adsorption of Reactive Orange 16 on the surface of Amberlyst A21.

16 sorption by Amberlyst A21, various pH values from 2.0 to 10.0 were tested. As shown in Fig. 4, when the pH value was 2.0, the maximum removal efficiency (90.58%) was achieved. And with the rice of pH value, the removal percent of Reactive Orange 16 decreases gradually to pH 8.0. This behavior can be explained by the electrostatic interactions between anionic Reactive Orange 16 dye and positively charged Amberlyst A21 surface [R-NH$_3$(Amberlyst) + H$_2$O ↔ RNH$_4^+$ (Amberlyst) + OH$^-$(aqueous)] [16]. As solution pH increased from 2.0 to 4.0, the removal efficiency significantly reduced from 90.58% to 65.22%.
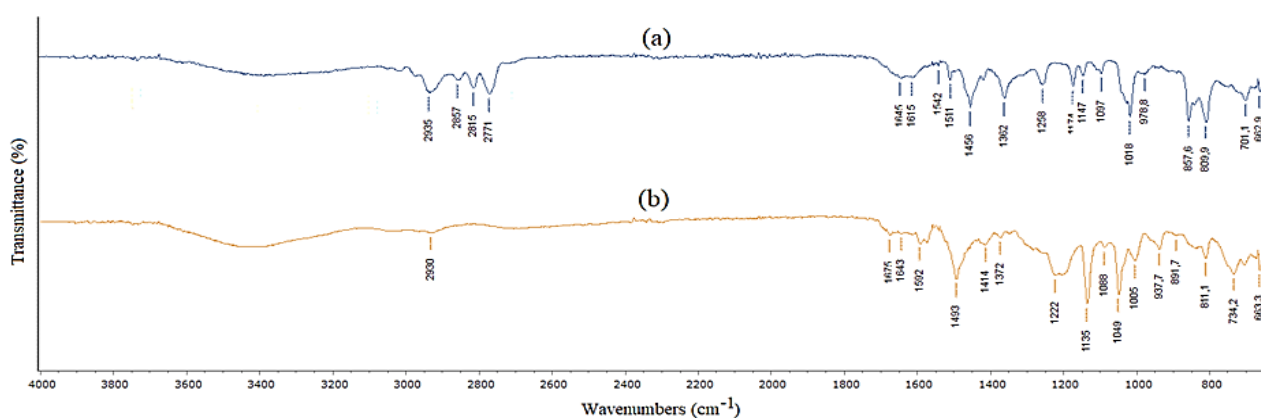
Figure 2. FT-IR spectra of (a) naked Amberlyst A21 and (b) Reactive Orange 16-Amberlyst A21.
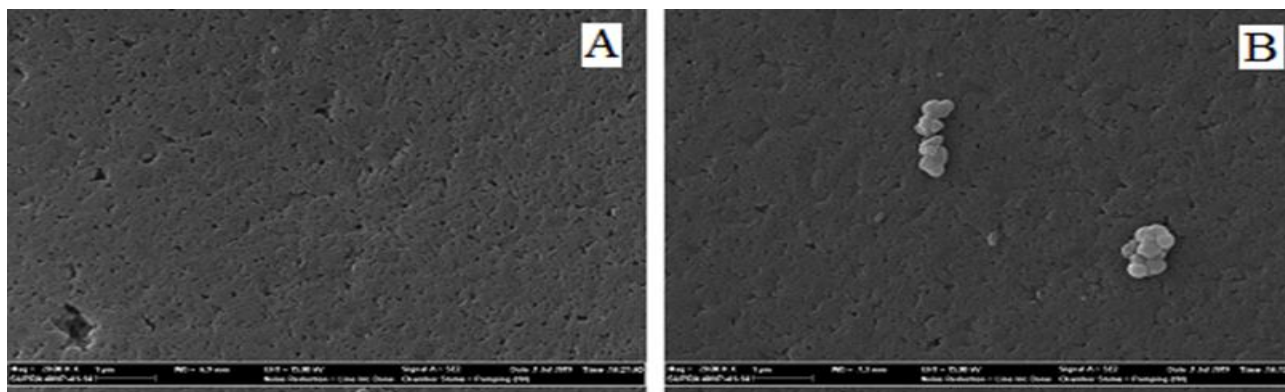
Figure 3. SEM images of (a) Reactive Orange 16 unloaded Amberlyst A21 and (b) Reactive Orange 16 loaded Amberlyst A21 resin.

Fig. 3 shows SEM images of Amberlyst A21 resin before (A) and after adsorption (B), indicating that the surface of Amberlyst A21 had a large surface area and rough porous structure.

3.2. Effect of solution pH and contact time
The solution pH plays an important role on the removal of dyes during the adsorption process because pH affects ionic forms of Reactive Orange 16 molecule and Amberlyst A21 surface charge. To reveal the optimum pH value for the Reactive Orange

The decrease in the adsorption of Reactive Orange 16 at pH greater than 2.0 can be related to the decrease of the positively charged sites of the Amberlyst A21 surface at a basic medium. Moreover, at higher pH values, the lower dye adsorption onto Amberlyst A21 can be linked to the large number of hydroxyl ions present, which compete with the negative dye groups for the adsorption binding sites of the resin. Further solution pH increased (4.0-10.0) removal percent of Reactive Orange 16 did not change remarkably. It is seen that this experimental result is consistent with the literature [16].
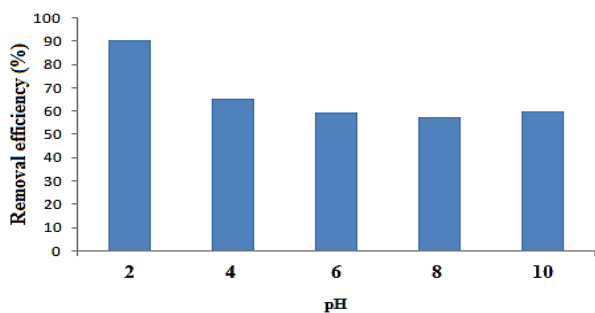
Figure 4. Effect of solution pH on the removal efficiency of Reactive Orange 16 using by Amberlyst A21 (C_0=100 mg L^{-1}, adsorbent dosage=1.0 g L^{-1}).

An important experimental factor that vigorously affects the adsorption of contaminants is the contact time. The effects of contact time on the removal of Reactive Orange 16 using by Amberlyst A21 was investigated in the range of 5-200 minutes at 100 mg L^{-1} initial Reactive Orange 16 solution at pH 2.0. The increasing dye removal percent with increasing contact time. After 180 minutes, curve of adsorption percentage tended to flat and no obvious change on the adsorption percentage of Reactive Orange 16 was observed. Therefore, the optimal contact time for Reactive Orange 16 adsorption on Amberlyst A21 was determined as 180 minutes for further removal studies.

3.3. Effect of Amberlyst A21 dose
The adsorbent dose is another important experimental condition for removing dyes from wastewaters and it determines the uptake capacity of adsorbents. The removal of Reactive Orange 16 was studied by varying the Amberlyst A21 dose from 0.25 to 2.00 g L^{-1} at other optimum experimental conditions. Adsorbent dosage increased from 0.75 to 2.00 g L^{-1}; the percent removal of 100 mg L^{-1} Reactive Orange 16 increased from 73.42 to 100.00 for Amberlyst A21. This can be attributed to the increased surface area of adsorbent and availability of more binding sites as the adsorbent dosage increases [22]. In this study, the Amberlyst A21 dose was selected as 1.0 g L^{-1} with the percent removal of 90.58%.

3.4. Effect of the initial Reactive Orange 16 concentration
The effect of the initial Reactive Orange 16 concentration on the removal performance of Amberlyst A21 was studied in the concentration range from 50 to 300 mg L^{-1} using by 1.00 g L^{-1} Amberlyst A21 dosage at 25 °C. The percent adsorption decreased with an increase in initial Reactive Orange 16 concentration. With the increase

of the initial concentration of Reactive Orange 16 from 50 to 300 mg L^{-1}, the adsorption capacity of Amberlyst A21 was greatly increased from 46.46 to 161.44 mg g^{-1}. However, when the concentration of dye increases further, the growth rate of adsorption decreases.

3.5. Adsorption isotherm study
The adsorbate-adsorbent interactions can be easily estimated by plotting the adsorption data into equilibrium isotherm models and the isotherm models help in understanding the designing of adsorption systems [23]. In the present work, three isotherm models, Langmuir, Freundlich, and Temkin were used to define the most appropriate isotherm model for the adsorption of Reactive Orange 16 onto Amberlyst A21. The Langmuir isotherm model is one of the most frequently used models in adsorption to describe the adsorption of adsorbate onto solid adsorbent surface. This isotherm model assumes that the adsorption takes place on an even monolayer surface with no layer interaction [24,25]. Also, the maximum adsorption capacity (qm) of adsorbents can be studied by the Langmuir adsorption isotherms. The Langmuir isotherm equation can be given as follows [26]:

$$\frac{C_e}{q_e} = \frac{C_e}{q_m} + \frac{1}{q_m K_L} \qquad (3)$$

Freundlich isotherm supposes that adsorption occurs on heterogeneous surfaces and according to this model different sites having different adsorption energies are involved during the adsorption process [27,28]. The equation of the Freundlich isotherm model is given as follows;

$$log q_e = log K_F + \frac{1}{n} log C_e \qquad (4)$$

The Temkin isotherm model assumes that the heat of the adsorption of all molecules in the layer decreases linearly with the surface of adsorbent coverage due to adsorbate-adsorbent interactions [29]. The Temkin isotherm model is given by the following equation;

$$qe = A \, ln K_T + A \, ln C_e \qquad (5)$$

In these equations; q_m is the maximum adsorption capacity (mg g^{-1}), A is the constant related to the heat of adsorption, K_T is the Temkin isotherm equilibrium

binding constant, K_L is the Langmuir constant ($L\ mg^{-1}$), K_F is the Freundlich constant and n is a parameter related to adsorbate-adsorbent affinity.

Equilibrium isotherm of Reactive Orange 16 on Amberlyst A21 was obtained at pH 2.0 and 25 °C. The Langmuir, Freundlich, and Temkin adsorption parameters calculated for Reactive Orange 16 are presented in Table 1 and Fig. 5.

The coefficient value (R^2) for the Langmuir isotherm model was over 0.990, as shown in Table 1, higher than that for Freundlich and Temkin isotherm model, suggesting the adsorption isotherm of Reactive Orange 16 onto Amberlyst A21 fits the Langmuir isotherm model.

The value of R_L is one of the most important parameters of the Langmuir isotherm and is called a separation factor. This dimensionless constant parameter of Reactive Orange 16 was obtained according to the Equation (6);

$$R_L = \frac{1}{1 + K_L C_0} \qquad (6)$$
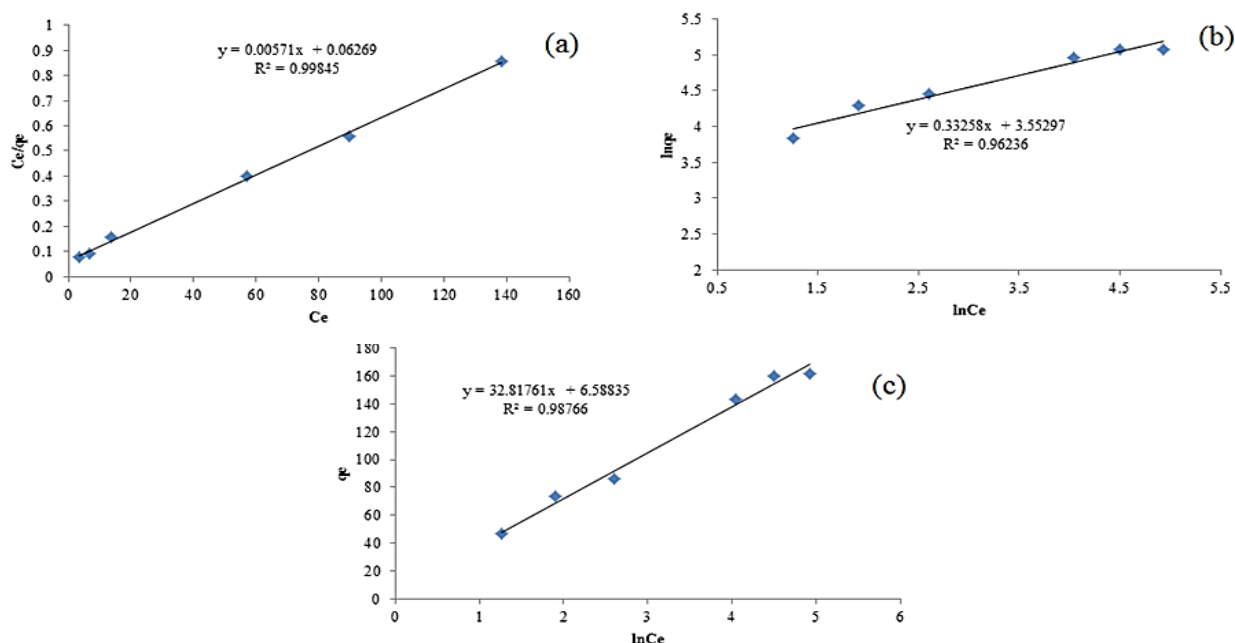
Figure 5. Isotherm models of (a) Langmuir, (b) Freundlich, and (c) Temkin for the adsorption of Reactive Orange 16 on Amberlyst A21

According to this result, during the adsorption process, the uptake of Reactive Orange 16 occurs on a homogenous surface by monolayer adsorption without any interaction between adsorbed dyes molecules [22].

Table 1. Isotherm parameters of Langmuir, Freundlich and Temkin models for Reactive Orange 16 adsorption on Amberlyst A21.

Langmuir	**R^2**	**q_m**	**K_L**	
	0.9985	175.13	0.09	
Freundlich	**R^2**	**$1/n$**	**n**	**K_F**
	0.9624	0.3326	3.01	34.92
Temkin	**R^2**	**A**	**K_T**	
	0.9877	32.82	1.22	

The maximum adsorption capacity q_m determined from the Langmuir isotherm defines the total capacity of the Amberlyst A21 for the Reactive Orange 16 as 175.13 mg g^{-1}.

where C_0 is the initial Reactive Orange 16 concentration and K_L is a Langmuir isotherm constant. In this regard, the dimensionless constants were calculated as 0.035-0.099 for dye, suggesting that the adsorption process is favorable [5] and Amberlyst A21 can be used for dye removal.

3.6. Adsorption kinetic study

Adsorption kinetic investigations are very important with respect to defining the adsorption rate, which is one of the parameters used to determine adsorbent performance and to verify the adsorption mechanism considering a rate-limiting step.

The kinetics of Reactive Orange 16 adsorption was investigated by pseudo-first and second-order kinetics model according to following equations, respectively [30].

$$log(q_e - q_t) = -\frac{k_1}{2.303}t + log\, q_e \qquad (7)$$

$$\frac{t}{q_t} = \frac{1}{k_2 q_e^2} + \frac{1}{q_e}t \qquad (8)$$

where q_t (mg g^{-1}) and q_e (mg g^{-1}) are adsorption capacity at time (t) and equilibrium adsorption capacity, respectively. k_1 (min^{-1}); the rate constant of pseudo-first-order model was calculated from the slope of the plots of log (q_e-q_t) versus t. k_2 is the pseudo-second-order rate constant in (g mg^{-1} min) and this constant is calculated from the intercept of the plots of t q_t^{-1} versus t.

the obtained and theoretical qe values and higher correlation coefficients.

4. Conclusion

The adsorption properties of Amberlyst A21 resin was studied by removal of Reactive Orange 16 azo dye from aqueous solutions, and the solution pH dependence of adsorption was also investigated in this manuscript.

The experimental results indicated the optimal pH for maximum adsorption was 2.0 at 25 °C. Under optimal adsorption conditions pH 2.0, adsorbent dosage 1.0 g L^{-1} and 180 minutes contact time the maximum adsorption capacity was determined as 175.13 mg g^{-1}.

Figure 6. Adsorption kinetic graphs of Reactive Orange 16 onto Amberlyst A21 (a) pseudo first order and (b) pseudo second order kinetic model.

The fitted curves of the experimental adsorption data of two kinetic models were given in Fig. 6, and the calculated kinetic parameters were tabulated in Table 2. Kinetic parameters of Reactive Orange 16 on Amberlyst A21 were obtained at pH 2.0 and 25 °C.

Table 2. The adsorption kinetic constants of the Amberlyst A21 to Reactive Orange 16.

Amberlyst A21	Pseudo first order kinetic model				Pseudo second order kinetic model		
	qe_{exp} (mg g^{-1})	qe_{cal} (mg g^{-1})	k_1 (min^{-1})	R^2	qe_{cal} (mg g^{-1})	k_2 (g mg^{-1} dak^{-1})	R^2
	86.50	89.50	1.73x10^{-2}	0.9739	119.76	1.21x10^{-4}	0.9890

The value of correlation coefficient, R^2, for the pseudo-first-order kinetic model is relatively high and the theoretical adsorption capacity calculated (qe_{cal}) by the kinetic equation (89.50 mg g^{-1}) is also very close to the determined value (86.50) by adsorption experiment (qe_{exp}) for 100 mg L^{-1} Reactive Orange 16. The results indicate that the pseudo-first-order model is more suitable for Amberlyst A21 resin to adsorption of Reactive Orange 16 dye from aqueous solutions because of consistency between

The adsorption isotherm studies showed that the adsorption of Reactive Orange 16 corresponded well with the Langmuir isotherm model. Also, the R_L values represented that adsorption of dye onto Amberlyst A21 was favorable. The investigation of adsorption kinetic data indicated that the proposed adsorption process could be described as a pseudo-first-order kinetic model with k_1 and qe of 1.73x10^{-2} min^{-1} and 89.50 mg g^{-1}, respectively. Also, the results of this study show a simple way of wastewater treatment and a new adsorbent for dye removal which might develop an environmental process based on the use of Amberlyst A21 resin.

References

[1] J.W. Kang, Removing environmental organic pollutants with bioremediation and phytoremediation, Biotechnol Lett, 36, 2014, 1129-1139.

[2] H. Xie, X. Xiong, A porous molybdenum disulfide and reduced graphene oxide nanocomposite (MoS2-rGO) with high adsorption capacity for fast and preferential adsorption towards Congo red, J Environ Chem Eng, 5(1), 2017, 1150-1158.

[3] S. Venkatesh, A.R. Quaff, N.D. Pandey, K. Venkatesh, Decolorization and mineralization of C.I. direct red 28 azo dye by ozonation, Desalin Water Treat, 57(9), 2016, 4135-4145.

[4] G.G. Bessegato, J.C. Souza, J.C. Cardoso, M.V.B. Zanoni, Assessment of several advanced oxidation processes applied in the treatment of environmental concern constituents from a real hair dye wastewater, J Environ Chem Eng, 6(2), 2018, 2794-2802.

[5] B. Satılmış, T. Uyar, Amine modified electrospun PIM-1 ultrafine fibers for an efficient removal of methyl orange from an aqueous system, Appl Surf Sci, 453, 2018, 220-229.

[6] U.D. Gül, H. Silah, Comparison of color removal from reactive dye contaminated water by systems containing fungal biosorbent, active carbon and their mixture, Water Sci Technol, 70(7), 2014, 1168-1174.

[7] N. Nikooe, E. Saljoughi, Preparation and characterization of novel PVDF nanofiltration membranes with hydrophilic property for filtration of dye aqueous solution, Appl Surf Sci, 413, 2017, 41-49.

[8] M. Chenna, R. Chemlal, N. Drouiche, K. Messaoudi, H. Lounici, Effectiveness of a physicochemical coagulation/flocculation process for the pretreatment of polluted water containing Hydron Blue Dye, Desalin Water Treat, 57, 2016, 27003-27014.

[9] J. Chukki, S. Shanthakumar, Optimization of malachite green dye removal by *Chrysanthemum Indicum* using response surface methodology, Environ Prog Sustain, 35(5), 2016, 1415-1419.

[10] M. Wawrzkiewicz, Z. Hubicki, E. Polska-Adach, Strongly basic anion exchanger Lewatit MonoPlus SR-7 for acid, reactive, and direct dyes removal wastewaters, Sep Sci Technol, 53(7), 2018, 1065-1075.

[11] K.M. Reza, A.S.W. Kurny, F. Gulshan, Parameters affecting the photocatalytic degradation of dyes using TiO$_2$: A review, Appl Water Sci, 7(4), 2017, 1569-1578.

[12] N.M. Mahmoodi, Z. Mokhtari-Shourijeh, J. Abdi, Preparation of mesoporous polyvinyl alcohol/chitosan/silica composite nanofiber and dye removal from wastewater, Environ Prog Sustain, 38, 2018, 100-109.

[13] G.Z. Kyzas, M. Kostoglu, Green adsorbents for wastewaters: A critical review, Materials, 7(1), 2014, 333-364.

[14] J.Z. Mitrovic, M.D. Radovic, T.D. Andelkovic, D.V. Bojic, A.L.J. Bojic, Identification of intermediates and ecotoxicity assessment during the UV/H$_2$O$_2$ oxidation of azo dye Reactive Orange 16, J. Environ Sci Heal, A 49(5), 2014, 491-502.

[15] S. Mishra, A. Maiti, Process optimization for effective bio-decolourization of reactive orange 16 using chemometric methods, J Environ Sci Heal, A 54(3), 2019, 179-192.

[16] D. Guimarães, V.A. Leão, Batch and fixed-bed assessment of sulphate removal by the weak base ion exchange resin Amberlyst A21, J Hazard Mater, 280, 2014, 209-215.

[17] Z. Hubicki, A. Wolowicz, Adsorption of palladium (II) from chloride solutions on Amberlyst A 29 and Amberlyst A 21 resins, Hydrometallurgy, 96(1-2), 2009, 159-165.

[18] B. Han, W. Carvalho, L. Canilha, S.S. da Silva, J.B.A.E. Silva, J.D. McMillan, S.R. Wickramasinghe, Adsorptive membranes vs. resins for acetic acid removal from biomass hydrolysates, Desalination, 193(1-3), 2006, 361-366.

[19] S.K. Sarı, D. Özmen, Design of optimum response surface experiments for the adsorption of acetic, butryic, and oxalic acids on Amberlyst A21, J Disper Sci Technol, 39(2), 2018, 305-309.

[20] J.M. Karekar, S.V. Divekar, Adsorption studies of chromium (VI) on weak base resins Tulsion A-10X (MP) and Amberlyst A-21 (MP) in aqueous and mixed media, Desalin Water Treat, 82, 2017, 252-261.

[21] S. Nagireddi, A.K. Golder, R. Uppaluri, Role of protonation and functional groups in Pd(II) recovery and reuse characteristics of commercial anion exchange resin-synthetic electroless plating solution systems, J Water Process Eng, 22, 2018, 227-238.

[22] P. Sathishkumar, M. Arulkumar, T. Palvannan, Utilization of agro-industrial waste *Jatropha curcas* pods as an activated carbon for the adsorption of reactive dye Remazol Brilliant Blue R (RBBR), J Clean Prod, 22(1), 2012, 67-75.

[23] F. Kallel, F. Chaari, F. Bouaziz, F. Bettaieb, R. Ghorbel, S.E. Chaabouni, Sorption and desorption characteristics for the removal of a toxic dye, methylene blue from aqueous solution by a low-cost agricultural by-product, J Mol Liq, 219, 2016, 279-288.

[24] V. Janaki, K. Vijayaraghavan, A.K. Ramasamy, K.J. Lee, B.T. Oh, S. Kamala-Kannan, Competitive adsorption of Reactive Orange 16 and Reactive Brilliant Blue R on polyaniline/bacterial extracellular polysaccharides composite-A novel eco-friendly polymer, J Hazard Mater, 241-242, 2012, 110-117.

[25] H. Zhu, T. Chen, J. Liu, D. Li, Adsorption of tetracycline antibiotics from an aqueous solution onto graphene oxide/calcium alginate composite fibers, RSC Adv, 8(5), 2018, 2616-2621.

[26] I. Langmuir, Adsorption of gases on plane surfaces of glass mica and platinum, J Am Chem Soc, 40(9), 1918, 1361-1403.

[27] S.R. Mishra, R. Chandra, J. Kaila, S. Darshi, Kinetics and isotherm studies for the adsorption of metal ions onto two soil types, Environ Technol Inno, 7, 2017, 87-101.

[28] H.M.F. Freundlich, Over the adsorption in solution, Phys Chem, 57, 1906, 385-470.

[29] S. Dadfarnia, A.M.H. Shabani, S.E. Moradi, S. Emami, Methyl red removal from water by iron-based metal-organic frameworks loaded onto iron oxide nanoparticle adsorbent, Appl Surf Sci, 330, 2015, 85-93.

[30] Y.S. Ho, G. Mckay, Pseudo-second order model for sorption processes, Process Biochem, 34(5), 1999, 451-465

The new tetrasubstituted metallophthalocyanines bearing four Schiff bases on the periphery: Synthesis, spectroscopic properties, and investigation of the effect of various central metals on aggregation properties

Halise Yalazan[1] (ID), Ayse Aktas Kamiloglu[2] (ID), Halit Kantekin[1*] (ID), Ümmühan Ocak[1] (ID)

[1]Karadeniz Technical University, Faculty of Sciences, Department of Chemistry, 61080, Trabzon, Turkey
[2] Artvin Çoruh University, Artvin Vocational School, 08100, Artvin, Turkey

Abstract

In the present study, new Schiff base compound (Z)-4-((quinolin-2-ylmethyleneamino)methyl)phenol (3) and phthalonitrile derivative (Z)-4-(4-((quinolin-2-ylmethyleneamino)methyl)phenoxy)phthalonitrile (4) were synthesized in the first step. Then, zinc (II) (Pc-5), cobalt (II) (Pc-6) and copper (II) (Pc-7) phthalocyanines containing Schiff base group including quinoline on peripheral positions were synthesized. All new compounds were characterized by general spectroscopic techniques. Aggregation properties of the obtained metallophthalocyanines were researched in polar and apolar solvents.

1. Introduction

Phthalocyanine complexes (Pcs) exhibit amazing physical and chemical properties. Phthalocyanines (Pcs) are versatile and stable aromatic macrocycles, they can also add a large number of metallic and non-metallic ions to the ring core. Due to the electronic and optical properties of Pcs, they have a great number of application areas. The most important disadvantage of unsubstituted Pcs is their poor solubility in prevalent polar and apolar solvents. Therefore, the solubility properties of Pcs are important for their usability in many applications. The solubility properties of phthalocyanines can be increased by adding long-chain alkyl, alkoxy, alkylthio, and bulky groups at the peripheral positions [1-5].

Aggregation is an important event for phthalocyanine complexes. Two types of aggregation are observed in the substituted phthalocyanines. These are called H-aggregation (face-to-face) and J-aggregation (side-to-side) [1,2]. In general, while phthalocyanine aggregation ensues a decrease in intensity of the Q band corresponding to the monomeric species, a new, broader, and blue-shifted band with increasing intensity is seen. The H-aggregation corresponding to blue-shifted is seen as a lower wavelength shift in Pcs. On the contrary, the J-aggregation corresponding to red-shifted is observed as a higher wavelength shift and is rarely seen in phthalocyanines [6-10].

Alkaloids containing nitrogen atoms are compounds that exhibit natural biological activity [11,12]. The quinolines are an important hetero-ring alkaloid obtained from coal tar and Cinchona (Quina) tree. Due to quinoline rings in its structures, these compounds show wide biological activity such as anti-malaria, anti-bacterial, anti-fungal, antitumor, anti-asthma, anti-inflammatory, and HIV replication inhibitor [13-22]. Many quinolines are ligands used in coordination chemistry as a N or O atom donor for chelating with metals [23-26].

Schiff base compounds formed with azo and azomethine groups are called azo-containing Schiff bases. These compounds are usually synthesized by condensation of an azo aldehyde with primary amine

[27]. Schiff bases play an important role in the development of organic synthesis and coordination chemistry. Their complexes in the literature are generally formed by transition metals [28].

As seen in the literature, there are few studies on the effect of aggregation properties of phthalocyanines containing quinoline. In our previous studies, we synthesized phthalocyanine compounds peripheral tetra substituted containing a quinoline group [29-31]. We wondered how different quinoline groups on the Schiff base impress aggregation properties of phthalocyanine compounds. In this work, we have planned to prepare phthalocyanine compounds containing substituted (*Z*)-4-((quinolin-2-ylmethyleneamino)-methyl)phenol as substituents on peripheral positions and investigated their aggregation properties. We used 2-quinolinecarboxaldehyde (1) and 4-hydroxybenzylamine (2) compounds during the synthesis of the Schiff base compound because the long-chain and bulky groups increase the solubility of phthalocyanine compounds. The solubility of phthalocyanines is important for their applications.

In the present study, the synthesis, characterization, spectroscopic and aggregation properties of zinc (II) (Pc-5), cobalt (II) (Pc-6) and copper (II) (Pc-7) phthalocyanines bearing four (*Z*)-4-((quinolin-2-ylmethyleneamino)methyl)phenol groups at the peripheral positions are investigated (Scheme 1). These phthalocyanine complexes exhibited good solubility in many organic solvents such as diethyl ether, DCM, ethyl acetate, THF, chloroform, DMF, and DMSO. As a result, the influence on aggregation properties of diverse central metal ions (zinc (II), cobalt (II), and copper (II)) in new phthalocyanine complexes was researched in many organic solvents.

2. Experimental

2.1. Synthesis

2.1.1. (Z)-4-((quinolin-2-ylmethyleneamino)methyl) phenol (3)

1.00 g (6.36 mmol) of 2-quinolinecarboxaldehyde (1) and 0.78 g (6.36 mmol) of 4-hydroxybenzylamine (2) were mixed in the methanol in a round-bottomed flask. Then, 15 drops of glacial acetic acid was added to the reaction mixture. This mixture was stirred under nitrogen atmosphere at reflux temperature for 48 h. At the end of this period, the reaction mixture was cooled and removed under vacuum. The resulting crude product was extracted with water:chloroform (20:20 v/v). The organic phase was

dried with MgSO$_4$, filtered and evaporated. The purification of the product was made by column chromatography on silica gel with chloroform: ethanol (50:1 v/v) solvent system. In conclusion, (*Z*)-4-((quinolin-2-ylmethyleneamino)-methyl)phenol(the Schiff base derivative) (3) was attained as orange solid product. Yield: 0.70 g (42%), m.p: 91-94 °C. FT-IR (ATR), v_{max} (cm^{-1}): 3059 (O-H), 3009 (Ar-H), 2921-2850 (Aliph. C-H), 1681, 1615, 1596, 1503, 1450, 1426, 1376, 1237, 1143, 1101, 938, 827, 752.^{1}H NMR (CDCl$_3$), (δ:ppm): 8.22-8.18 (m, 4H, Ar-H), 8.04 (m, 1H, Ar-H), 7.84-7.73 (m, 3H, Ar-H), 7.55 (s, 1H, CH=N),7.00 (s, 1H, OH), 6.78(d, 1H, Ar-H), 6.63 (d, 1H, Ar-H), 3.34 (s, 2H, -N-CH$_2$) ^{13}C NMR (CDCl$_3$), (δ:ppm):155.77 (imine carbon), 153.81,152.88, 151.05, 150.21, 149.77, 147.77, 145.81, 136.41, 136.10, 129.70, 128.44, 121.79, 120.54, 115.33, 115.08, 58.48 (N-CH$_2$) MS (ES$^+$) m/z: Calculated: 262.31; Found: 263.22 [M+H]$^+$.

2.1.2. (Z)-4-(4-((quinolin-2-ylmethyleneamino)methyl) phenoxy)phthalonitrile (4)

The Schiff base derivative (3) (0.70 g, 2.67 mmol) and 4-nitrophthalonitrile (0.46 g, 2.67 mmol) were dissolved in dry DMF (15 mL) in a two-necked round-bottomed flask. After stirring for 30 min at 50 °C, anhydrous potassium carbonate (1.11g, 8.01 mmol) was added in reaction ingredient with small portions. The reaction mixture was monitored by TLC and stirred at 55 °C for 112 h under N$_2$ atmosphere. At the end of this period, this mixture was poured into ice-water and stirred at room temperature. The obtained crude product filtered and washed with ethyl alcohol and hexane, then dried in a vacuum desiccator. The purification of the product was made by column chromatography on silica gel with chloroform:ethanol (50:5 v/v) solvent system. Consequently, the phthalonitrile derivative (4) was obtained as straw yellow solid product. Yield: 0.64 g (62%), m.p: 137-140 °C. FT-IR (ATR), v_{max} (cm^{-1}): 3044 (Ar-H), 2919-2851 (Aliph. C-H), 2231 (C≡N), 1675, 1617, 1592, 1562, 1484, 1423, 1377, 1278, 1248, 1208, 1167, 1088, 1015, 950, 830, 756. ^{1}H NMR (CDCl$_3$), (δ:ppm): 8.30-8.27 (m, 1H, Ar-H), 8.18 (d, 1H, Ar-H), 8.08 (m, 1H, Ar-H), 8.00 (m, 2H, Ar-H), 7.91-7.86 (m, 2H, Ar-H), 7.59-7.46 (m, 2H, Ar-H and CH=N), 7.05 (m, 3H, Ar-H), 6.72 (d, 2H, Ar-H), 3.45 (s, 2H, N-CH$_2$) ^{13}C NMR (CDCl$_3$), (δ:ppm): 161.71, 158.02, 152.10, 147.82, 140.41, 136.89, 136.07, 135.26, 134.96, 129.96, 129.56, 129.37, 129.18, 127.20, 126.96, 125.75, 123.83, 121.71, 120.29-120.21 (C≡N), 117.50, 115.35, 114.96, 108.64, 58.49 (N-CH$_2$) MS (ES$^+$) m/z: Calculated: 388.42; Found: 388.08 [M]$^+$.

2.1.3. General synthesis of metallophthalocyanines (Pc 5-7)

The phthalonitrile compound (4) (0.15 g, 0.386 mmol) and anhydrous metal salts [Zn(OAc)$_2$ (35 mg, 0.193 mmol) (for the complex *Pc-5*), CoCl$_2$ (25 mg, 0.193 mmol) (for the complex *Pc-6*) and CuCl2 (26 mg, 0.193 mmol) (for the complex *Pc-7*)] were dissolved in n-amyl alcohol (3 mL) and immediately after6 drops of DBU were added. The reaction mixtures were heated and stirred at 140 °C in a standard Schlenk tube under a nitrogen atmosphere for 20 h. After cooling to room temperature, green reaction mixtures were precipitated by adding ethanol. The obtained green solid products were stirred in ethyl alcohol under the N$_2$ atmosphere at reflux temperature overnight. Then, this mixture was filtered off, washed with ethanol and diethyl ether, and then dried in a vacuum desiccator. Finally, all metallophthalocyanine complexes (*Pc* 5-7) were obtained as green solids.

2.1.3.1. Zinc (II) Phthalocyanine (Pc-5)

Yield: 34 mg (22%), m.p.>300 ºC. FT-IR (ATR), v_{max} (cm^{-1}): 3060 (Ar-H), 2922-2852 (Aliph. C-H), 1645, 1596, 1504, 1467, 1389, 1318, 1261, 1229, 1164, 1088, 982, 943, 834, 759. ^{1}H NMR (CDCl$_3$), (δ:ppm): 7.19 (m, 44H, Ar-H), 3.41 (m, 8H, N-CH$_2$)UV-vis (THF), λ_{max}, nm (logε): 677 (4.44), 611 (3.91), 351 (4.47). MALDI-TOF-MS m/z: Calculated: 1619.08; Found: 1642.08 [M+Na]$^+$.

2.1.3.2. Cobalt (II) Phthalocyanine (Pc-6)

Yield: 22 mg (14%), m.p.>300 ºC. FT-IR (ATR), v_{max} (cm^{-1}): 3060 (Ar-H), 2919-2850 (Aliph. C-H), 1597, 1504, 1466, 1406, 1329, 1262, 1230, 1093, 1057, 1015, 956, 872, 828, 753, 662. UV-vis (THF), λ_{max}, nm (logε): 665 (4.38), 606 (4.03), 339 (4.67). MALDI-TOF-MS m/z: Calculated: 1612.63; Found: 1635.63 [M+Na]$^+$.

2.1.3.3. Copper (II) Phthalocyanine (Pc-7)

Yield: 38 mg (24%), m.p.>300 ºC. FT-IR (ATR), v_{max} (cm^{-1}): 3059 (Ar-H), 2919-2850 (Aliph. C-H), 1646, 1596, 1504, 1464, 1376, 1318, 1266, 1232, 1156, 1091, 1052, 1016, 983, 950, 873, 827, 747 UV-vis (THF), λ_{max}, nm (logε):677 (4.66), 611 (4.15), 347 (4.66). MALDI-TOF-MS$m/z$: Calculated: 1617.25; Found: 1640.25 [M+Na]$^+$.

3. Results and discussion

3.1. Synthesis and characterization

The synthesis scheme of all compounds was shown in Scheme 1. The Schiff base derivative (Z)-4-((quinolin-2-ylmethyleneamino)methyl)phenol (3) and phthalonitrile derivative (Z)-4-(4-((quinolin-2-ylmethyleneamino) methyl) phenoxy) phthalonitrile (4) were synthesized in the first step. Afterward zinc (II) (*Pc-5*), cobalt (II) (*Pc-6*), and copper (II) (*Pc-7*) phthalocyanines containing Schiff base were synthesized at peripheral positions. 2-quinolinecarboxaldehyde (1) and 4-hydroxybenzylamine (2) were treated with the glacial acetic acid in the methanol led to (Z)-4-(quinolin-2-ylmethyleneamino) methyl) phenol (3). The phthalonitrile (4) was acquired by the aromatic nucleophilic substitution reaction of 4-nitrophthalonitrile with (Z)-4-((quinolin-2-ylmethyleneamino)methyl)phenol (3) using K$_2$CO$_3$ as the base in dry DMF. This reaction was performed at 55 °C under N$_2$ atmosphere for 112 h. Subsequently, the metallophthalocyanines zinc (II) (*Pc-5*), cobalt (II) (*Pc-6*) and copper (II) (*Pc-7*) phthalocyanines were accomplished by the cyclotetramerization of phthalonitrile in the presence of anhydrous metal salts (Zn(OAc)$_2$, CoCl$_2$ and CuCl$_2$) in n-amyl alcohol and in the presence of DBU for 20 h. The structures of the new compounds were approved using UV-vis (for the metallophthalocyanines), FT-IR (all new compounds), ^{1}H NMR (except (*Pc-6*) and (*Pc-7*)), ^{13}C NMR and LC-MS/MS (for the compounds 3 and 4), MALDI-TOF mass spectral data (for all the MPcs). The obtained data are consistent with the expected structures as indicated in Section 2.

Some opinions about the structures of the products were obtained with the comparison of FT-IR spectra. In the IR spectrum of Schiff base derivative (3) stretching vibrations of OH group at 3059 cm^{-1} appeared and this value, in the IR spectrum of phthalonitrile derivative (4) disappeared. The dinitrile derivative (4) exhibited the characteristic C≡N stretching vibrations at 2231 cm^{-1}. Other characteristic vibration bands were observed at 3009 cm^{-1} (for the compound 3) and 3044 cm^{-1} (for the compound 4) for aromatic C-H stretching; between 2921-2850 cm^{-1} (for the compound 3) and between 2919-2851 cm^{-1} (for the compound 4) for aliphatic C-H stretching.

The ^{1}H NMR spectra of Schiff base derivative (3) and dicyano compound (4) were recorded in CDCl$_3$. In the ^{1}H NMR spectra of phthalonitrile (4), the signal OH group belonging to Schiff base derivative (3) disappeared as predicted after the conversion of this compound. In the ^{1}H NMR spectra of Schiff base derivative (3) and dicyano compound (4), the aromatic protons were observed among 8.20-6.59 ppm (for the compound 3) and 8.30-6.65 ppm (for the

compound **4**). The ¹³C NMR spectra of the dinitrile compound demonstrated that the nitrile group of carbon atoms was observed between 120.29-120.21 ppm (for **4**). The mass spectra of Schiff base derivative (**3**) and dicyano compound (**4**) were measured by the LC-MS/MS spectral data and molecular ion peaks were specified at m/z: 263.22 [M+H]⁺, 388.08 [M]⁺ respectively (Fig. 1).
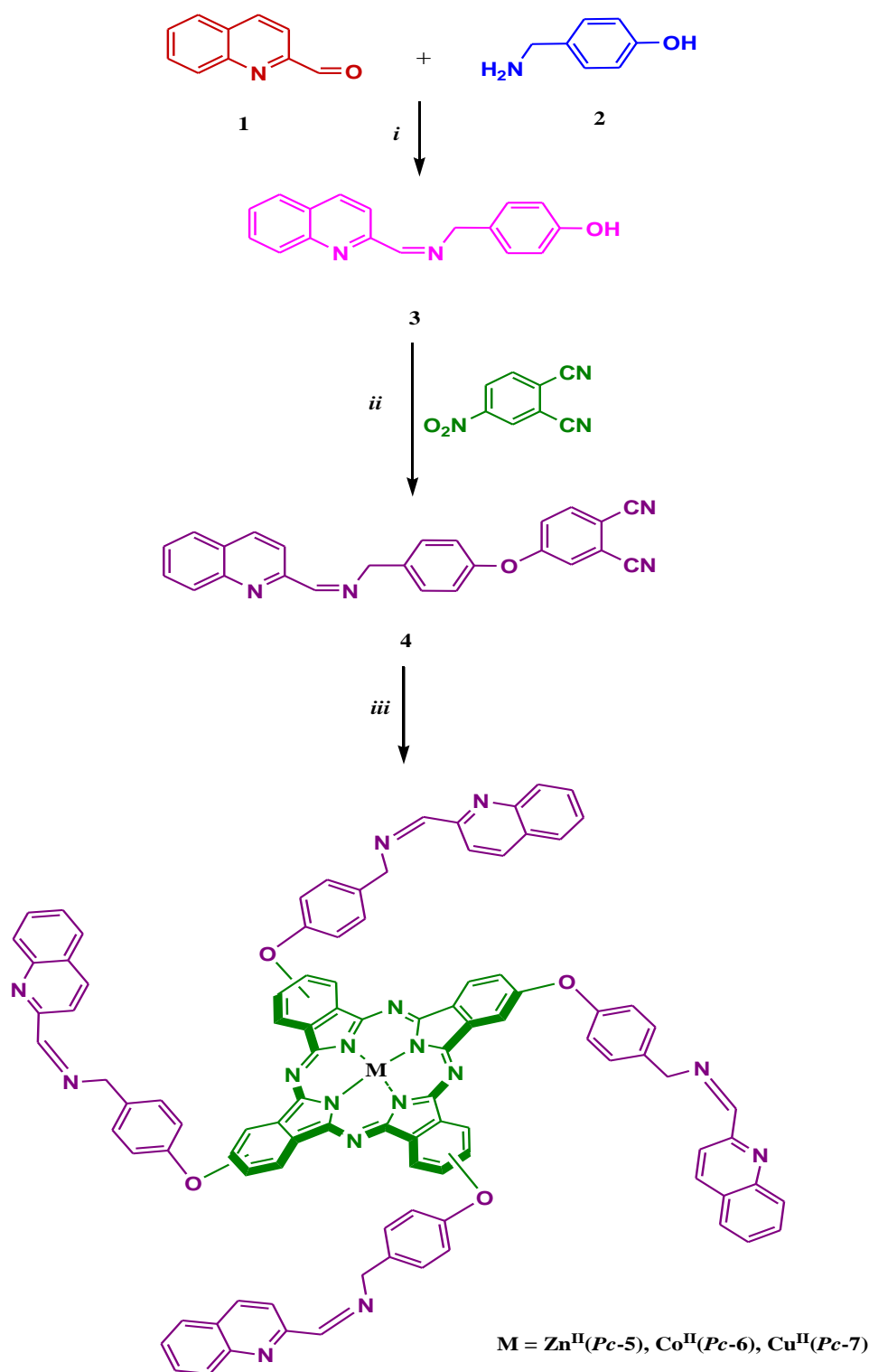
Scheme 1. Synthesis of Schiff base compound (**3**), phthalonitrile derivative (**4**) and metallophthalocyanines (*Pc*-**5**, *Pc*-**6** and *Pc*-**7**). Reagents and conditions (i) Methanol, glacial acetic acid, reflux temperature, N₂; (ii) N₂, K₂CO₃, DMF, 55°C; (iii) N₂, n-amyl alcohol, DBU, Zn(OAc)₂, CoCl₂ and CuCl₂, 140°C.
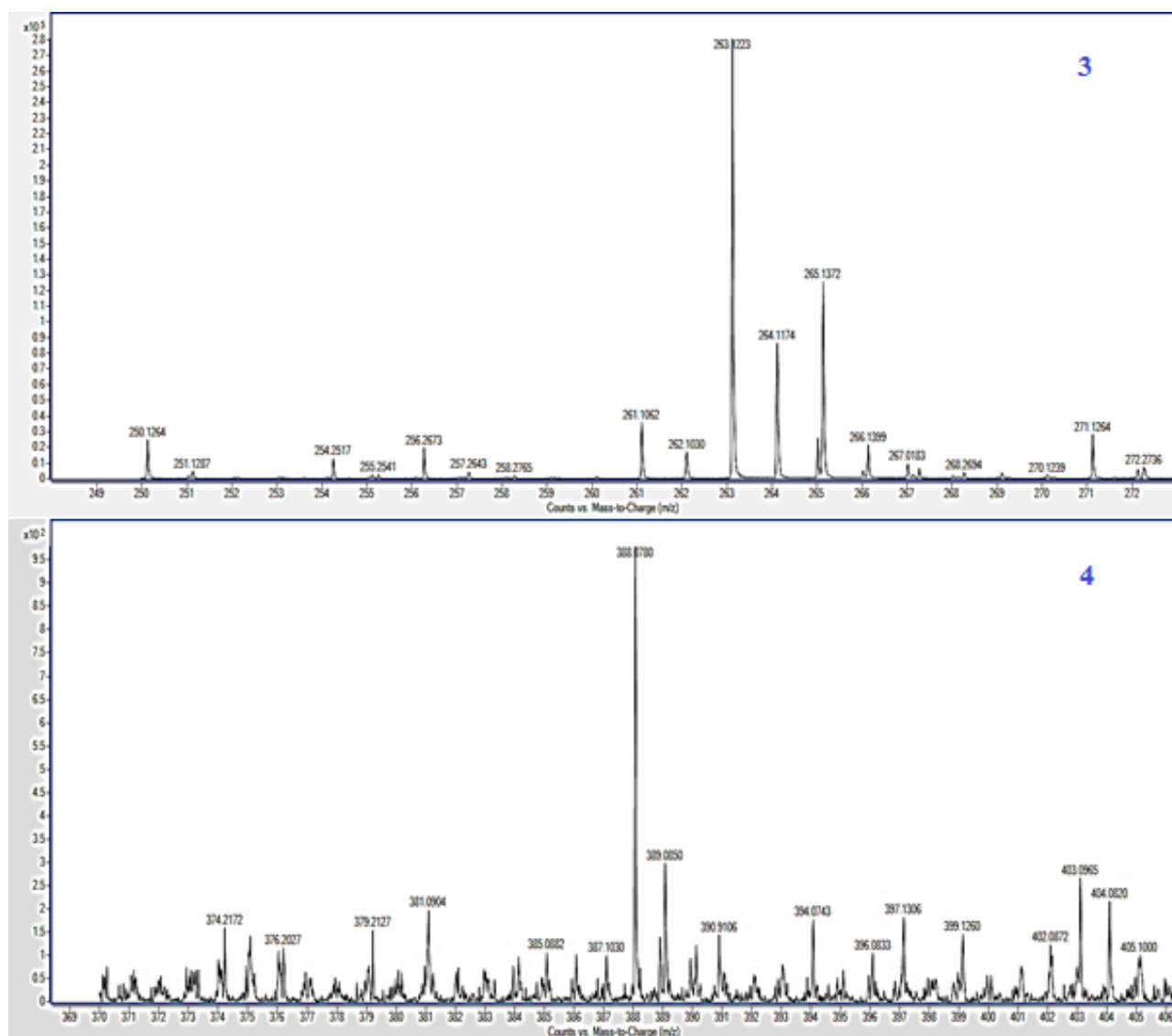
Figure 1. Mass spectra of the compounds 3 and 4.

In the FT-IR spectra of metallophthalocyanines, vibration bands were observed at 3060 cm^{-1} (for the complexes *Pc*-**5** and *Pc*-**6**) and 3059 cm^{-1} (for the complex *Pc*-**7**) for aromatic C-H stretching; between 2922-2852 cm^{-1} (for the complex *Pc*-**5**), 2919-2850 cm^{-1} (for the complexes *Pc*-**6** and *Pc*-**7**) for aliphatic C-H stretching. The ^{1}H NMR spectra of the synthesized phthalocyanine complex (*Pc*-**5)** was recorded in CDCl$_3$ and this MPc complex exhibited broad chemical shift when compared with that of corresponding Schiff base derivative (**3**) and dicyano compound (**4**). In the ^{1}H NMR spectra of MPc complex (*Pc*-**5**), the aromatic protons were observed at 7.19 ppm (for the complex *Pc*-**5**). In the mass spectra of phthalocyanine complexes acquired by the MALDI-TOF technique, the molecular ion peaks were observed at m/z: 1642.08 [M+Na]$^+$ for *Pc*-**5**, 1635.63 [M+Na]$^+$ for *Pc*-**6** and 1640.25 [M+Na]$^+$ for *Pc*-**7**.

The UV-vis spectra of the synthesized all new peripheral zinc (II) (*Pc*-**5**), cobalt (II) (*Pc*-**6**) and copper (II) (*Pc*-**7**) phthalocyanines were registered in THF at a concentration of 1.0 x 10^{-5} M. All of the obtained phthalocyanine complexes (*Pc*-**5**, *Pc*-**6**, and *Pc*-**7**) exhibited a spectrum similar to non-aggregated Pcs. The UV-vis spectra of peripheral zinc (II) (*Pc*-**5**), cobalt (II) (*Pc*-**6**) and copper (II) (*Pc*-**7**) phthalocyanines exhibited sharp and intense absorption band belonging the typical Q-bands at 677 nm (logε = 4.44) for *Pc*-**5**, 665 nm (logε = 4.38) for *Pc*-**6** and 677 nm (logε = 4.66) for *Pc*-**7** with a lower wavelength vibronic band at 611 nm (logε = 3.91) for *Pc*-**5**, 606 nm (logε = 4.03) for *Pc*-**6** and 611 nm (logε = 4.15) for *Pc*-**7**.The B-band absorptions for these complexes were exhibited at 351 nm (logε = 4.47) for *Pc*-**5**, 339 nm (logε = 4.67) for *Pc*-**6** and 347 nm (logε = 4.66) for *Pc*-**7**.
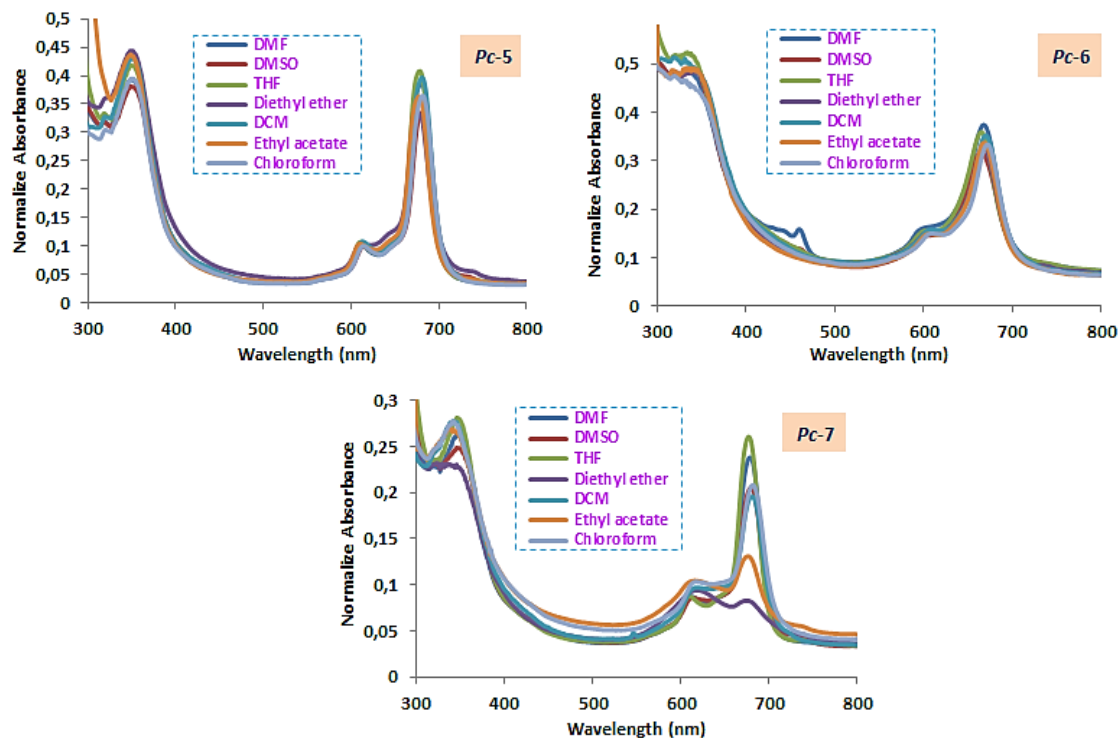
Figure 2. The ground state electronic absorption spectra of *Pc*-5, *Pc*-6, and *Pc*-7 in different solvents.
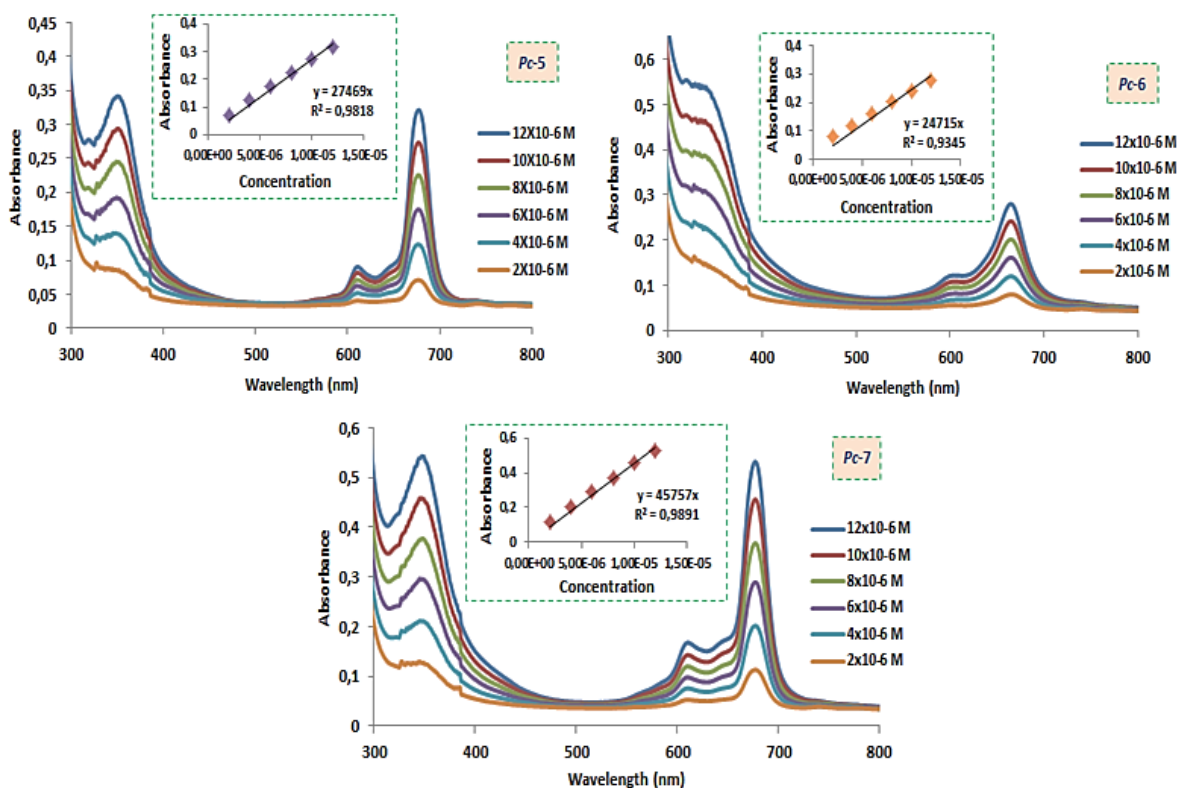
Figure 3. The ground state electronic absorption spectra of *Pc*-5, *Pc*-6 and *Pc*-7 in THF at different concentrations (2.0×10^{-6} to 12×10^{-6} M).

3.2. Aggregation studies

Aggregation is a co-planar association of macrocyclic rings and forms the assembly of monomers to dimers and higher-order aggregates. When the molecules aggregate, new bands come out in the absorption spectra. The reason is the formation of aggregation when the intermolecular attraction force between phthalocyanine molecules is stronger than the Pc-

solvent association [32,33]. Pcs have a high aggregation affinity on account of the interactions between their 18-π electron systems, which decreases their solubility property in many solvents and seriously affect their areas of usage. The aggregation behavior of MPcs depends on the nature of the temperature, the concentration-nature of the solvent, the substituents, and the complexed metal ion [34, 35].

In this paper, the aggregation behaviors of the peripheral tetra substituted zinc (II) (**Pc-5**), cobalt (II) (**Pc-6**) and copper (II) (**Pc-7**) phthalocyanines were researched in various solvents such as DMF, DMSO, THF, diethyl ether, DCM, ethyl acetate and chloroform to select an appropriate solvent for the usage of their in many applications (Fig. 2). The absorption intensities of Q bands showed significant changes by these solvents. If we look at the aggregation studies, the zinc (II) (**Pc-5**) phthalocyanine did not exhibit any aggregation in all studied solvents on account of sharp Q band intensities. Also, the cobalt (II) (**Pc-6**) phthalocyanine exhibited aggregation (H-aggregation) in DMSO and ethyl acetate, however, it did not demonstrate any aggregation in the other studied solvents. In addition to these, Q band of the copper (II) (**Pc-7**) phthalocyanine considerably reduced in diethyl ether and ethyl acetate and it exhibited aggregation (H-aggregation) in these two solvents.

The aggregation behaviors of the MPcs (**Pc-5**, **Pc-6**, and **Pc-7**) were examined at different concentrations in THF (Fig. 3). When the concentration increased, the absorption intensity of the Q band also increased and a new band due to the formation of aggregated species in THF was not observed. Beer-Lambert law was applied for all studied MPcs in the concentrations ranging from 2.0×10^{-6} to 12×10^{-6} M. The studied MPcs (**Pc-5**, **Pc-6**, and **Pc-7**) did not exhibit any aggregation at these concentration ranges in THF.

4. Conclusion

In conclusion, the present study has been explained the synthesis, spectroscopic properties, and investigation of the effect on aggregation properties of various central metal ions in synthesized MPcs. The Schiff base derivative (*Z*)-4-((quinolin-2-ylmethyleneamino)methyl)phenol (**3**), phthalonitrile derivative (*Z*)-4-(4-((quinolin-2-ylmethyleneamino)methyl)phenoxy) phthalonitrile (**4**) and peripheral tetra substituted zinc (II) (**Pc-5**), cobalt (II) (**Pc-6**), and copper (II) (**Pc-7**)

phthalocyanines were synthesized for the first time. The all new compounds were identified by general spectroscopic techniques. Because the aggregation and solubility of phthalocyanines are important for their applications, we used 4-hydroxybenzylamine (**2**) containing long chain and 2-quinolinecarboxaldehyde (**1**) including bulky group. Thus, metallophthalocyanine complexes exhibited good solubility in many organic solvents such as diethyl ether, DCM, ethyl acetate, THF, chloroform, DMF, and DMSO. The effects of concentration and solvent on the aggregation behavior of the new metallophthalocyanine complexes were researched. The effects of solvent on the aggregation behavior were investigated for MPcs (**Pc-5**, **Pc-6**, and **Pc-7**) in diethyl ether, DCM, ethyl acetate, THF, chloroform, DMF, and DMSO. All synthesized MPcs did not exhibit aggregation in chloroform, THF, and DCM. Besides, the effects of concentration on the aggregation behavior were examined for MPcs (**Pc-5**, **Pc-6**, and **Pc-7**) in THF. The all studied MPcs did not demonstrate any aggregation in the concentrations ranging from 2.0×10^{-6} to 12×10^{-6} M.

References

[1] C.C. Leznoff, A.B.P. Lever, Phthalocyanines: Properties and Applications, 1989, New York, VCH Publishers.

[2] K. Kadish, K.M. Smith, R. (Eds.) Guilard, The Porphyrin Handbook, 2003, Boston, Academic Press.

[3] N.B. McKeown, Phthalocyanine materials synthesis, structure and function, 1998, Cambridge University Press.

[4] B. Ertem, H. Yalazan, Ö. Güngör, G. Sarkı, M. Durmuş, E.T. Saka, H.Kantekin, Synthesis, structural characterization, and investigation on photophysical and photochemical features of new metallophthalocyanines, J Lumin, 204, 2018, 464-471.

[5] H. Kantekin, E.T. Saka, B. Ertem, M.N. Mısır, H. Yalazan, G. Sarkı, New peripherally tetra-[trans-3,7-dimethyl-2,6-octadien-1-ol] substituted metallophthalocyanines: Synthesis, characterization and catalytic activity studies on the oxidation of phenolic compounds, J Coord Chem,71(1), 2018, 164-182.

[6] K. Kameyama, M. Morisue, A. Satake, Y. Kobuke, Highly fluorescent self-coordinated phthalocyanine dimers, Angew Chem Int Edit, 44, 2005, 4763-4766.

[7] J.L. Sesler, J. Jayawickramarajah, A. Gouloumis, G.D. Patnos, T. Torres, D.M. Guldi, Guanosine and fullerene derived de-aggregation of a new phthalocyanine-linked cytidine derivative, Tetrahedron, 62, 2006, 2123-2131.

[8] X. Huang, F.Q. Zhao, Z.Y. Li, L. Huang, Y.W. Tang, F. Zhang, C.H. Tung, A novel self-aggregates of phthalocyanine based on Zn-O coordination, Chem Lett, 36, 2007, 108-115.

[9] X. Huang, F.Q. Zhao, Z.Y. Li, Y.W. Tang, F. Zhang, C.H. Tung, Self-assembled nanowire networks of aryloxy zinc

phthalocyanines based on Zn-O coordination, Langmuir, 23, 2007, 5167-5172.

[10] M. Morisue, Y. Kobuke, Tandem cofacial stacks of porphyrin-phthalocyanine dyads through complementary coordination, Chem-Eur J, 14, 2008, 4993-5000.

[11] H. Manfred, Alkaloids: Nature's curse or blessing, Verlag Helvetica Chimica Acta, 2002, Zürich, Switzerland and, Weinheim, Germany, Wiley-VCH,

[12] C.Y. Poon, P. Chiu, A synthesis of the tetracyclic carboskeleton of isaindigotidione. Tetrahedron Lett, 45, 2004, 2985-2988.

[13] S. Ökten, O. Çakmak, Ş. Tekin, The structure activity relationship (SAR) study of 6,8-disubstituted quinoline derivatives as anti cancer agents, Turk J Clin Lab, 8(4), 2017, 152-159.

[14] I. Jacquemond-Collet, F. Benoit-Vical, A. Valentin, E. Stanislas, M. Mallié, I. Fourasté, Antiplasmodial and cytotoxic activity of galipinine and other tetrahydroquinolines from Galipea officinalis, Planta Med, 68 (1), 2002, 68-69.

[15] K.C. Fang, Y.L. Chen, J. Sheu, T.C. Wang, C.C. Tzeng, Synthesis, antibacterial, and cytotoxic evaluation of certain 7-substituted norfloxacin derivatives, J Med Chem, 43, 20, 2000, 3809-3812.

[16] P. Palit, P. Paira, A. Hazra, S. Banerjee, A.D. Gupta, S.G. Dastidar, N.B. Mondal, Phase transfer catalyzed synthesis of bisquinolines: Antileishmanial activity in experimental visceral leishmaniasis and in vitro antibacterial evaluation, Eur J Med Chem, 44, 2009, 845-853.

[17] B. Podeszwa, H. Niedbala, J. Polanski, R. Musiol, D. Tabak, J. Finster, K. Serafin, M. Milczarek, J. Wietrzyk, S. Boryczka, W. Mol, J. Jampilek, J. Dohnal, D.S. Kalinowski, Dolezal, D.R. Richardson, Investigating the antiproliferative activity of quinoline-5,8-diones and styrylquinolinecarboxylic acids on tumor cell lines, Bioorg Med Chem Lett, 17, 2007, 6138-6141.

[18] R. Musiol, J. Jampilek, V. Buchta, L. Silva, H. Niedbala, B. Podeszwa, A. Palka, K. Majerz-Maniecka, B. Oleksyn, J. Polanski, Antifungal properties of new series of quinoline derivatives, Bioorg Med Chem, 14, 2006, 3592-3598.

[19] S. Ökten, O. Çakmak, R. Erenler, Ö.Y. Şahin, Ş. Tekin, Simple and convenient preparation of novel 6,8-disubstituted quinoline derivatives and their promising anticancer activities, Turk J Chem, 37, 2013, 896-908.

[20] S. Ökten, Ö.Y. Şahin, Ş. Tekin, O. Çakmak, In vitro antiproliferative/ cytotoxic activity of novel quinoline compound SO-18 against various cancer cell lines, J Biotechn, 185S, 2014, S37-S125.

[21] F. Zouhiri, M. Danet, C. Benard, M. Normand-Bayle, J-F. Mouscadet, H. Leh, C.M. Thomas, G. Mbemba, J. D'Angelo, D. Desmaele, HIV-1 replication inhibitors of the styrylquinoline class: Introduction of an additional carboxyl group at the C-5 position of the quinoline, Tetrahedron Lett, 46, 2005, 2201-2205.

[22] A. Şahin, O. Çakmak, İ. Demirtaş, S. Ökten, A. Tutar, Efficent and selective synthesis of quinoline derivatives, Tetrahedron, 64, 2008, 10068-10074.

[23] S. Broch, B. Aboab, F. Anizon, P. Moreau, Synthesis and in vitro antiproliferative activities of quinoline derivatives, Eur J Med Chem, 45, 2010, 1657-1662.

[24] J.E. Nycz, M. Szala, G.J. Malecki, M. Nowak, J. Kusz, Synthesis, spectroscopy and computational studies of selected hydroxyquinolines and their analogues, Spectrochim Acta A, 117, 2014, 351-359.

[25] B. Machura, J. Milek, J. Kusz, J. Nycz, D. Tabak, Reactivity of oxorhenium(V) complexes towards quinoline carboxylic acids. X-ray structure of [ReOCl2(hquin-7-COOH)(PPh₃)]·OPPh3, [ReOBr2(hquin-7-COOH)(PPh3)] and [ReOX2(hmquin-7-COOH)(PPh3)]. DFT and TD-DFT

calculations for [ReOCl2(hquin-7-COOH)(PPh₃)], Polyhedron, 27, 2008, 1121-1130.

[26] S.D. Lytton, B. Mester, I. Dayan, H. Glickstein, J. Libman, A. Shanzer, Z.I. Cabantchik, Mode of action of iron (III) chelators as antimalarials: I. Membrane permeation properties and cytotoxic activity, Blood, 81, 1993, 214-221.

[27] Z. Rezvani, L.R. Ahar, K. Nejati, S.M. Seyedahmadian, Syntheses, characterization and liquid crystalline properties of new bis[5-((4-"alkoxyphenyl)azo)-N-("alkyl) salicylaldiminato]copper (II) and nickel (II) complex homologs, Acta Chim Slov, 51, 2004, 675- 686.

[28] P. Sen, S.Z. Yildiz, M. Tuna, M. Canlica, Preparation of aldehyde substituted phthalocyanines with improved yield and their use for Schiff base metal complex formation, J Organomet Chem, 769, 2014, 38-45.

[29] Z. Bıyıklıoglu, M. Durmuş, H. Kantekin, Synthesis, photophysical and photochemical properties of quinoline substituted zinc (II) phthalocyanines and their quaternized derivatives, J Photoch Photobiol A, 211, 2010, 32-41.

[30] A. Nas, Ü. Demirbaş, M. Pişkin, M. Durmuş, H. Kantekin, The photophysical and photochemical properties of new unmetallated and metallated phthalocyanines bearing four 5-chloroquinolin-8-yloxy substituents on peripheral sites, J Lumin, 145, 2014, 635-642.

[31] A.A. Kamiloglu, İ. Acar, Z. Bıyıklıoglu, Synthesis and electrochemical properties of new metal-free and metallophthalocyanines bearing 2,6-dimethylquinoline-4-yl derivatives, Polyhedron, 137, 2017, 10-16.

[32] S. Altun, A.R. Özkaya, M. Bulut, Peripheral octa-substituted metal-free, cobalt (II) and zinc (II) phthalocyanines bearing coumarin and chloro groups: Synthesis, characterization, spectral and electrochemical properties, Polyhedron, 48, 2012, 31-42.

[33] A.W. Snow, Phthalocyanine aggregation, in: K. Kadish, R. Guilard, K.M. Smith, The Porphyrin Handbook, Phthalocyanines: Properties and Materials, 17, 2003, Amsterdam, Academic Press.

[34] H. Enkelkamp, R.J.M. Nolte, Molecular materials based on crown ether functionalized phthalocyanines, J Porphyr Phthalocya, 4, 2000, 454-459.

[35] D.D. Dominguez, A.W. Snow, J.S. Shirk, R.S. Pong, Polyethyleneoxide-capped phthalocyanines: limiting phthalocyanine aggregation to dimer formation, J Porphyr Phthalocya, 5, 2001, 582-592.

Voltammetric analysis of class II antiarrhythmic drugs propranolol and acebutolol

Dilek Kul* [iD], Fatma Ağın [iD]

Karadeniz Technical University, Faculty of Pharmacy, Department of Analytical Chemistry, 61080, Trabzon, Turkey

Abstract

Antiarrhythmic agents are used to suppressing abnormal rhythms of the heart. Class II antiarrhythmic agents are beta-blockers used to treat supraventricular tachycardias. Voltammetric analysis of class II antiarrhythmic drug active ingredients propranolol and acebutolol carried out with various modified/non-modified electrodes using cyclic voltammetry (CV), linear sweep voltammetry (LSV), differential pulse voltammetry (DPV) and square wave voltammetry (SWV) were compiled from the literature. The effect of supporting electrolyte and pH was interpreted. Scan rate results obtained with the voltammetric methods showed whether the redox process of the drug active ingredient diffusion or adsorption controlled on the electrode used in the selected supporting electrolyte. Results of the quantitative analysis of these drugs were evaluated in terms of parameters such as linearity range, the limit of detection, stability, robustness, repeatability, reproducibility, and sensitivity. Accuracy and precision of the validated methods were compared by combining the results obtained from the pharmaceutical dosage forms of the drug active ingredients. Finally, the analytical application of the drugs in real samples such as human serum and urine was evaluated and it was examined whether the analysis results were affected by the other substances in real samples.

1. Introduction

Hypertension is one of the most common diseases detected in over 60% of people over 60 years old [1,2]. Although hypertension is not controlled, it is a complex disease that seriously affects the structure and function of many organs in the body, but the prevalence of hypertension in society is quite high [3-5]. It might also cause chronic kidney failure [6-8]. Beta-adrenergic receptor antagonists (β-blockers) used in the treatment of hypertension cause significant effects and side effects in order to eliminate/decrease the sympathetic muscle tone in various organs and structures, primarily the heart, and in proportion to the degree of this tone [9-12].

Antiarrhythmic agents are used to suppressing abnormal rhythms of the heart [13]. According to Vaughan Williams classification introduced in 1970 [14-17], antiarrhythmic agents are classified as Class I as sodium channel blockers, Class II as beta-blockers, Class III as potassium channel blockers, Class IV as calcium channel blockers and Class V with variable mechanisms [18].

Today, the increasing use of beta-blockers has enabled analysis to become very important and many chemical analysis methods are used for this purpose. There are many studies in the literature using spectroscopic [19-22], chromatographic [23-28], and electrochemical methods for the quantitative analysis of propranolol and acebutolol. Electroanalytical methods are more advantageous than other methods due to their fast, good repeatability rate, high stability, low cost, low detection limit features. In addition, the sample does not have to be pretreated separately, which increases the use of these methods in drug analysis. In recent years, the widespread use of voltammetric methods in the determination of electrochemically active substances is noteworthy [29-33]. In the voltammetric methods, a three-electrode system is used and the selection of working electrodes is very important for precise and effective

analysis. Especially carbon and metal-based working electrodes are widely used because they are easy to find, relatively inexpensive and can be easily modified. In recent years, studies in which the working electrodes used have been modified with various electroactive materials, and their sensitivity and selectivity have been very popular. For this purpose, a wide variety of materials are used, such as carbon nanotubes, electroactive polymers, and metal nanoparticles. Numerous studies with modified electrodes are available in the literature, reporting that more sensitive results are obtained than bare electrodes [34-41].

In this review, electrochemical analysis studies of beta-adrenergic receptor antagonists acebutolol and propranolol were compiled and gathered. Analyzes made by using linear, cyclic, square wave, differential pulse, and adsorptive stripping voltammetric methods with these active substances were interpreted. It was aimed at this review to determine the electrochemical qualitative and quantitative analysis of these drug active substances selected from beta-blockers by using variously modified and/or unmodified electrodes and voltammetric methods.

1.1. Beta-adrenergic receptor blockers

Beta-adrenergic receptor blockers antagonize the effects of catecholamines on beta-adrenergic receptors [42-44]. Beta-blockers are used in the treatment of hypertension, angina, long-term treatment of heart failure, supraventricular tachyarrhythmia, acute myocardial infarction, migraine, hyperthyroidism, social phobia, essential tremor [44-49]. When beta-adrenergic receptor antagonists were used for the first time, it was not expected to show antihypertensive effects in patients with a primary indication of angina. However, later, all beta-adrenergic receptor antagonists have also been found to reduce arterial blood pressure in hypertensive patients with angina pectoris [17,50,51].

Beta-blockers are divided into two groups: Non-selective, i.e. those that competitively block both $\beta1$ and $\beta2$ adrenergic receptors, and are generally called $\beta1$ selectors and show more affinity for $\beta1$ receptors than $\beta2$ receptors [44].

Non-selective beta-blockers, such as propranolol, block both $\beta1$ adrenergic receptors, which are found in heart cells and enable the sympathetic effect to reach the heart, as well as $\beta2$ adrenergic receptors, which are found in the vascular, bronchus, gastrointestinal tract and relax.

Cardio selective beta-blockers such as acebutolol, atenolol, and metoprolol show selectivity to the $\beta1$ receptor, and because of these properties, they can be used safely in asthma patients where bronchospasm is contraindicated [18,44,52].

Beta-adrenergic receptor blockers are also frequently used in glaucoma treatment [53]. However, since non-selective agents cause more pronounced decreases in pulmonary function tests, pulse, and systolic blood pressure compared to selective ones, it is recommended to prefer selective ones in those with cardiac and respiratory problems [44].

Propranolol is seen as a standard that needs to be compared to newly developed drugs for systemic use. It has been used extensively for many years and has been found to be safe and effective for many indications [51,54].

The antagonization of beta-adrenergic receptors is effective in regulating circulation as a result of different mechanisms including myocardial contraction, cardiac contraction and decreased cardiac output. As a result of the use of beta-adrenergic receptors, beta receptors are blocked, thereby decreasing the release of renin and decreasing circulating angiotensin II production. In addition, beta-blockers act by increasing the sensitivity of baroreceptors to blood pressure [17,51].

1.2. Effect mechanisms and pharmacokinetic properties of beta-blockers

The antagonization of beta-adrenergic receptors is effective in regulating circulation as a result of different mechanisms including myocardial contraction, cardiac contraction, and decreased cardiac output. As a result of the use of beta-adrenergic receptors, the beta receptors are blocked, thereby decreasing the release of renin and decreasing circulating angiotensin II production. In addition, beta-blockers act by increasing the sensitivity of baroreceptors to blood pressure [17,51,55-57].

Absorption rates of beta-blockers are generally high, reaching maximum concentration 1-3 hours after ingestion. Propranolol has a lower bioavailability as it is exposed to the common first-pass effect. The rate of drugs reaching the systemic circulation is dose-dependent and increases with increasing dose [55,58,59].

Beta-antagonists are rapidly dispersed and have a large distribution volume. Since propranolol and lindolol are lipophilic, they quickly cross the blood-brain barrier. The half-life of most beta antagonists is 2-5 hours. Propranolol and metaprolol are metabolized in the liver; very few unchanged drugs

are found in the urine. Elimination of drugs such as propranolol may take longer in cases of liver disease, decreased hepatic blood flow, or inhibition of hepatic enzymes [55,60]. Side effects of beta-blockers are fatigue, weight gain, cold hands and feet, headache, depression, and trouble sleeping [61,62].

Beta-receptor blockers have different effects on different systems such as cardiovascular, respiration, and endocrine as below:

1.2.1. *Effects on the cardiovascular system*
When beta-blocking drugs are taken chronically, they reduce blood pressure in patients with hypertension. These drugs do not hypotension in healthy volunteers with normal doses of blood pressure. Beta receptor antagonists have pronounced effects on the heart such as negative inotropic and chronotropic effects.

1.2.2. *Effects on the respiratory system*
Blockade of β2 receptors in the bronchial smooth muscle increases the resistance of the respiratory tract, especially in patients with asthma. Although this problem is solved with the use of β1 selective antagonists, there are currently no β1 selective antagonists that do not affect β2-adrenoreceptors.

1.2.3. *Eye effects*
Some beta-blocking drugs have been found to decrease intraocular pressure, especially in the eye with glaucoma.

1.2.4. *Metabolic and endocrine effects*
Beta-antagonists such as propranolol cause inhibition of lipolysis stimulated by the sympathetic nervous system. Chronic use of beta-adrenoreceptor antagonists caused an increase in VLDL (Very Low-Density Lipoprotein) concentrations and a decrease in HDL (High-Density Lipoprotein) concentration. This event is undesirable in terms of the risk of developing cardiovascular disease [44,60].

1.3. Propranolol
Propranolol (PRP, Fig. 1) is a prototype of beta-blocking drugs. It is a non-selective beta-blocker used in the treatment of various cardiovascular disorders such as hypertension, angina pectoris, pheochromocytoma, cardiac arrhythmia, myocardial infarction, and dysfunctional birth. As with all non-selective blockers, it should be used with caution in patients with diabetes as hypoglycemia improves in patients with diabetes and suppresses symptoms of hypoglycemia such as tachycardia, sweating, and

tremor. It is PRP causing the most side effects related to the central nervous system such as sedation, memory impairment, and fatigue [44].

Since PRP has been abused in many sports in recent years to control stage fear, the International Olympic Committee has accepted PRP as doping and included it in the category of banned substances. As a result of the studies conducted in the World Anti-Doping Agency analysis laboratories, it has determined the maximum amount of the drug in the urine as 0.5 μg mL^{-1} [63].
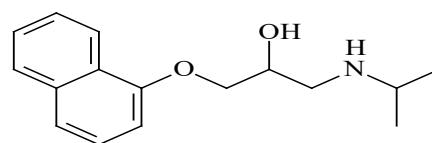
Figure 1. Structure of propranolol

1.4. Acebutolol
Acebutolol hydrochloride (ACB, Fig. 2) is a hydrophilic-adrenoreceptor blocking agent with cardio selective, mild intrinsic sympathomimetic activity. It slows the heart rate, prevents hand tremors, increases athletic performance (physical condition, abilities, and muscle strength), and has a calming effect. Therefore, determining this drug used by athletes in urine is of great importance [64].

Acebutolol has a lipophilic character and when taken orally, its absorption in the gastrointestinal tract is complete or nearly complete. Approximately 80% is excreted in urine and 20-30% in bile. It forms the active metabolite of diacetol in the body [44,65].
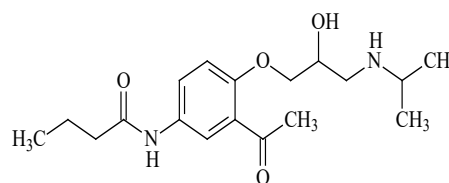
Figure 2. Structure of acebutolol

2. Electrochemical behavior of beta-blockers

Some studies presenting the electrochemical analysis of PRP and ACB carried out using various electrochemical sensors are available in the literature. The electroanalytical determination studies of PRP and ACB are described below and the results obtained using validated voltammetric methods are listed in Table 1.

2.1. Electroanalytical determination of PRP

Gaichore and Srivasta [66] prepared a modified carbon paste electrode based on γ-cyclodextrin carbon nanotube composite (γ-CD-CNT-CME) and used for the determination of PRP. Electrochemical analysis of PRP was checked out with cyclic voltammetry (CV) and differential pulse adsorptive stripping voltammetry (DPAdSV). CV results indicated that the electrooxidation of PRP was irreversible and adsorption controlled on γ-CD-CNT-CME. 0.04 M Britton Robinson buffer (BRB) solution at pH 1.5 was selected as supporting electrolyte in PRP determination. Under optimum experimental conditions, the peak current of PRP increased linearly with its concentration from 0.142 to 47.6 μM with a detection limit (LOD) of 40.19 nM by DPAdSV. The repeatability, reproducibility, precision, and accuracy of the selected method were detected by performing five replicate measurements for PRP with satisfactory results. Stability results indicated that the electrode was stable for about 6 months. The proposed method was used for the determination of PRP in pharmaceutical formulations, urine, and blood serum samples without any interference from other species.

p-(Melamine) film-coated edge plane pyrolytic graphite electrode (EPPG) was used as a sensitive electrochemical sensor for the determination of PRP by Raj et al. [67]. The p-(melamine)/EPPG sensor demonstrated excellent electrocatalytic activity for the oxidation of PRP with a significant increase in the peak current and a shift in the peak potential towards less positive potentials. Cyclic voltammograms of PRP showed a single irreversible oxidation peak at pH 7.4 on the p-(melamine)/EPPG sensor. Square wave voltammetry (SWV) was used for the detection of PRP as it has several advantages including excellent sensitivity and low background currents. Under optimum experimental conditions, the calibration plot of the peak current versus the concentration was found to be linear in the range of 0.1 to 800 μM. The limit of detection (LOD) and limit of quantification (LOQ) values were calculated as 9 nM and 30 nM, respectively. Interference studies were checked out to investigate the influence of some common interfering species (metabolites in biological fluids) in the determination PRP. It was observed no interference in the determination of PRP with the common metabolites in biological fluids. The modified sensor and the proposed method were applied to the determination of PRP in pharmaceuticals, human urine, and plasma samples with good recovery results.

A sensor-based on 8-hydroxy-8-propoxycalix [8] arene and multi-walled carbon nanotubes modified glassy carbon electrode (HPC-8/MWCNT/GCE) was prepared for the determination of PRP [63]. This modified electrode caused an increase in the peak current and the electrocatalytic activity on PRP electrooxidation. CV and DPV methods were used to investigate the electrooxidation behavior of PRP. The oxidation process of PRP was diffusion-controlled and irreversible on HPC-8/MWCNT/GCE. Oxidation peak currents were obtained linearly with PRP concentrations ranging from 0.338 to 54.1 μM with a detection limit of 135 nM in phosphate buffer solution (PBS) at pH 7.0. The results of the stability studies for HPC-8/MWCNT/GCE were stable for over 2 weeks and remained 91.7% reproducible when stored at 4 °C. The modified electrode was successfully used for the determination of PRP in pharmaceutical dosage forms.

In another study, a graphene and conductive polymer (poly-1,5-diaminonaphthalene) modified edge plane pyrolytic graphite (GR/PDAN/EPPG) electrode was used for the sensitive determination of PRP [68]. Cyclic voltammograms showed that the electrochemical oxidation of PRP was irreversible. The authors proposed a possible 2e[-]/2H[+] oxidation mechanism. The SWV method was applied to detect PRP over the concentration of 0.1 - 750 μM with a detection limit of 20 nM in PBS at pH 7.2. The results of reproducibility studies revealed that the sensor had excellent reproducibility with a relative standard deviation of 3.2%. The developed method was applied to detect PRP in pharmaceuticals, human urine, and blood plasma samples with good recoveries.

The electrochemical oxidation behavior of PRP was analyzed with CV and DPV methods using platinum nanoparticles doped multi-walled carbon nanotubes modified GCE (PtNPs/MWCNTs/GCE) by Kun et al. [69]. The oxidation reaction of PRP on PtNPs/MWCNTs/GCE was irreversible and diffusion controlled. The peak current response of PRP was linear in the concentration range of 0.676 to 38.0 μM with a LOD of 84.5 nM with DPV in PBS at pH 7.0. PtNPs/MWCNTs/GCE was found to be stable for two weeks. The prepared PtNPs/MWCNTs/GCE was used for the determination of PRP in its pharmaceutical dosage forms with reliable results.

A carbon paste electrode incorporated with nanosized propranolol-imprinted polymer (nanoMIP-CPE) was developed for the determination of N-nitrosopropranolol as a carcinogenic metabolite of PRP by Alizadeh and Allahyari [70]. Oxidation of

the hydroxyl group in N-nitrosopropranolol was used to monitor the target molecule. Under optimized conditions, the concentration of N-nitrosopropranolol ranged linearly from 0.1 to 10.0 µM with a LOD of 80.0 nM in acetate buffer solution at pH 4.5 by DPV method. The sensor and method developed for the determination of N-nitrosopropranolol were applied in plasma and gastric juice samples. The results clearly showed that the developed sensor and validated method could be applicable to detect N-nitrosopropranolol in real samples.

A reduced graphene oxide modified carbon paste electrode (rGO-CPE) was used to sensitively determine PRP by CV, DPV, and SWV methods [71]. The oxidation process of PRP was irreversible and diffusion controlled on rGO-CPE. The authors proposed that the electrooxidation of PRP involved $2H^+/2e^-$ transfer process. Under optimized conditions, the oxidation peak of PRP increased proportionally in the concentration range of 0.1 to 2.5 µM for DPV and 0.1 to 5.0 µM for SWV in BRB at pH 7.0. LOD values for DPV and SWV were calculated as 40.0 nM and 2.0 nM, respectively. The proposed sensor was successfully used to determine the amount of PRP in the pharmaceuticals, artificial urine, and serum samples with SWV.

Mohammadi and his colleagues developed a simple and sensitive method for PRP analysis using the magnetic core-shell manganese ferrite nanoparticles modified screen-printed carbon electrode (MCSNP/SPCE) [72]. CV and DPV methods were used for the electrochemical measurements of PRP. The oxidation reaction of PRP was irreversible and diffusion controlled on MSPCE/SPCE. DPV parameters were optimized for the quantitative determination of PRP. Under optimized conditions, the PRP peak current changed linearly with a concentration of 0.4 to 200.0 µM in PBS at pH 7.0. The detection limit was obtained as 80 nM. The developed method was applied for the measurement of PRP concentration in pharmaceutical dosage form and urine samples with good analytical performance.

Łuczak prepared a nanogold supported inorganic/organic hybrid 3D sensor (3D Au-NPs-Au electrode) for the electrochemical oxidation and quantitative determination of PRP [73]. The results of the scan rate study indicated that the irreversible oxidation process of PRP was controlled by diffusion in PBS at pH 7.4. The prepared sensor showed reliable results in the PRP concentration range from 0.1 to 20.0 µM with a detection limit of 0.0675 nM using the DPV method. The prepared voltammetric

sensor and the proposed method were applied to detect PRP in dosage forms without any interference.

Nateghi developed the $(Ti_{0.5}V_{0.5})_3C_2$ modified carbon paste electrode (CPE) and used it for the detection of PRP in its pharmaceutical dosage form and neutral solution by voltammetric methods [74]. According to the voltammetric analysis, it was proposed that the possible oxidation mechanism of PRP was over $2H^+/2e^-$. Linear PRP concentration range 0.5 - 5.0 µM, LOD value was obtained as 160.0 nM in BRB solution at pH 7.0 using DPV. The accuracy of the proposed method was demonstrated by the successful determination of PRP from its pharmaceutical dosage form.

In another study, the electroanalytical determination of PRP was carried out using a cathodically pretreated boron-doped diamond electrode (BDD) by the SWV method [75]. Cyclic voltammograms of PRP in 0.1 M H_2SO_4 showed one irreversible anodic peak with a diffusion-controlled process. The SWV method validated in the range of 0.2 - 9.0 µM for PRP in 0.1 M H_2SO_4. The LOD value for PRP was obtained as 180.0 nM. The proposed method was used for the determination of PRP in pharmaceutical formulations with good results.

Electroanalysis of PRP was investigated by CV and DPV methods using platinum nanoparticle doped multiwalled carbon nanotube-modified GCE (PtNPs/MWCNTs/GCE) in 0.1 M PBS at pH 7.4 [76]. PtNPs/MWCNTs/GCE showed electrocatalytic activity to the oxidation of PRP. Under optimized conditions, the linear range of PRP was 0.2 - 50 µM with a detection limit of 150.0 nM for the DPV method. The practical applicability of the developed modified electrode for the selective and sensitive determination of PRP was tested in serum samples and good recovery results were obtained.

When the studies in the literature described above were evaluated, it was seen that the electrochemical analysis of PRP was performed for the anodic behavior of PRP. Various modified or unmodified electrodes were used in the studies and it was found that PRP generally had a diffusion-controlled process. For this reason, DPV and SWV techniques could be used for the sensitive determination of PRP, except for a study done with DPAdSV due to the adsorption-controlled process of PRP [66]. The widest linearity ranges were obtained with p-(melamine) film-coated edge plane pyrolytic graphite electrode [67] and the graphene/conductive polymer (poly-1,5-diaminonaphthalene) modified edge plane pyrolytic graphite electrode [68]. Although the lowest LOD value was seen with the reduced graphene

oxide modified carbon paste electrode and SWV method [71], the linearity range of this study was narrow. The subsequent lowest LOD values were obtained for the studies with the widest linearity ranges [67,68]. Inter-day and intra-day repeatability values were obtained as RSD% and between 0.33% and 3.5%. Accuracy studies were carried out and recovery values were obtained in the range of 90.0% and 107.0% for pharmaceutical dosage forms, urine, serum, and gastric juice. Precision and accuracy studies showed that all electrodes and methods developed gave satisfying results and were suitable for the determination of PRP without any interference of excipients.

The possible oxidation mechanism of PRO has also been discussed in some studies, and two oxidation pathways have been proposed: The hydroxyl group in one of them and the secondary amine group in the other is thought to be oxidized. On both pathways, the redox mechanism proceeds over 2 electrons and 2 protons [63,66-69,71,76].

2.2. Electroanalytical determination of ACB

Al-Ghamdi et al. [77] investigated the cathodic electrochemical behavior of ACB using voltammetric methods with a hanging mercury drop electrode (HDME). The experimental results of ACB indicated an irreversible and adsorption controlled cathodic process of ACB. The reduction peak current was linear in proportion to the concentration of ACB in the range of 0.5 to 6.0 μM in BRB solution at pH 7.5 by square wave adsorptive stripping voltammetry (SWAdSV) under optimized conditions. LOD and LOQ values were obtained as 170.0 nM and 500.0 nM, respectively. The validated method was applied to direct analysis of ACB from its pharmaceutical dosage forms, human plasma, and human urine samples, with satisfying recovery results.

An electrochemical method for the determination of ACB was developed based on the pencil graphite electrode (PGE) by Levent [78]. ACB showed a reversible and adsorption controlled oxidation peak by CV method. The electrochemical oxidation mechanism of ACB was suggested to be via $2e^-/2H^+$. The oxidation peak current indicated a linear relationship between 0.0004 and 0.007 μM with a LOD of 0.09 nM in BRB solution at pH 10.0 by SWAdSV under the specified conditions. The proposed method was successfully applied for the ACB determination in pharmaceutical dosage forms and urine samples.

In another study, Yamuna et al. [79] investigated the electrochemical oxidation of ACB using screen-printed carbon electrodes (SPCE) with CV and DPV methods. SPCE was activated by electrochemical pretreatment prior to experiments. The authors reported that the activated SPCE (aSPCE) revealed a better performance than inactivated SPCE. ACB had an irreversible and diffusion-controlled electrooxidation process on aSPCE. The linear range was found to be 0.01 to 200 μM with a LOD of 6.0 nM in PBS at pH 7.0 with DPV. The results of the interference study indicated that aSPCE could be applicable for the determination of ACB in practical applications.

Detection of ACB was achieved using a simple and economic graphite pencil electrode (GPE) by Bagoji et al. [80]. Oxidation signals of ACB were measured by CV, DPV, and SWV methods. According to the results, the electrochemical oxidation process of ACB was irreversible and was defined as diffusion controlled. Oxidation peak currents increased linearly with an increase of ACB concentration in the range of 1.0 to 15.0 μM for DPV and SWV in PBS at pH 7.0. LOD values were obtained as 0.126 nM and 0.128 nM for DPV and SWV, respectively. The validated DPV method was applied for the detection of ACB in human urine samples.

Silva et al. [81] prepared a sensor based on a carbon paste electrode modified with amino-functionalized mesostructured silica (NH_2/HMS/CPE) for the simultaneous determination of ACB, pindolol, and metoprolol in waters by voltammetric methods. Two anodic and one cathodic peak were obtained for ACB using NH_2/HMS/CPE in 0.1 M PBS at pH 4.0. The first anodic peak and cathodic peak were attributed to a quasi-reversible redox process. The second irreversible anodic peak was used for the measurements of the experiments because it was more intense than the first oxidation peak. Scan rate studies indicated that the electrooxidation process of ACB on NH_2/HMS/CPE was adsorption controlled. The calibration curve obtained for ACB demonstrated a linear relationship in the concentration range of 0.5 - 50 μM. LOD and LOQ values were obtained with DPV as 58.0 and 190.0 nM, respectively. The proposed method was successfully applied for the determination of ACB, pindolol, and metoprolol in drinking water, environmental and wastewater samples.

Table 1. Validation data for the analysis of PRP and ACB (p=plasma, u=urine, ph= pharnaceut., w=real water sample, b=buffer, gj=gastric juice, hp=human plasma, hu=human urine)

Propranolol

Electrode Type	Method	Medium	Linear Range	LOD	LOQ	Precision (RSD%) Intra-day	Inter-day	Recovery (%)	Ref.
γ-CD-CNT-CME								99.5-99.8 (ph)	[66]
	DPAdSV	BRB, pH 1.5	0.142-47.60 μM	0.0401 μM	-	1.84	1.99	98.2-100.7 (u)	
								98.8-100.4 (s)	
p-(melamime)/ EPPGE	SWV	PBS, pH 7.4	0.1-800 μM	9 nM	30 nM	0.89	-	98.55-101.21 (u)	[67]
								98.63-101.62 (p)	
HPC-8/MWCNT/GCE	DPV	PBS, pH 7.0	0.338-54.10 μM	0.135 μM	-	3.2	-	99.4 (ph)	[63]
GR/PDAN/EPPG	SWV	PBS, pH 7.2	0.1-750 μM	20 nM	-	3.2	-	97.75 (ph)	[68]
PtNPs/MWCNTs/GCE	DPV	PBS, pH 7.0	0.676-38.0 μM	0.0845 μM	-	2.74	-	99.2 (ph)	[69]
nanoMIP-CPE	DPV	HClO$_4$, pH 4.5	0.1-10.0 μM	0.08 μM	-	-	-	90.0-106.0 (s)	[70]*
								91.0-107.0 (gj)	
rGO-CPE	DPV	BRB, pH 7.0	0.1-2.5 μM	0.04 μM	-	-	-	-	[71]
	SWV		0.1-5.0 μM	0.002 μM	-	-	-	100.0-100.34 (ph)	
								100.0 (u)	
								102.0 (s)	
MCSNP/SPCE	DPV	PBS, pH 7.0	0.4-200 μM	80 nM	-	-	-	97.8-103.9 (ph)	[72]
								97.0-102.5 (u)	
3D Au-NPs-Au electrode	DPV	PBS, pH 7.4	0.0001-0.02 mM	6.75x10^{-5} mM	-	-	2.9	97.0-105.0 (ph)	[73]
(Ti$_{0.5}$V$_{0.5}$)$_3$C$_2$ modified CPE	DPV	BRB, pH 7.0	0.5-5.0 μM	0.16 μM	-	-	-	94.0 (ph)	[74]
BDD	SWV	0.1 M H$_2$SO$_4$	0.2-9.0 μM	0.18 μM	-	0.33	3.5	93.3-105.0 (ph)	[75]
PtNPs/MWCNTs/GCE	DPV	PBS, pH 7.4	0.2-50 μM	0.15 μM	-	2.44	-	99.0-103.2 (s)	[76]

Acebutolol

Electrode Type	Method	Medium	Linear Range	LOD	LOQ	Precision (RSD%) Intra-day	Inter-day	Recovery (%)	Ref.
HDME	SWAdSV	BRB, pH 7.5	0.5-6.0 μM	0.17 μM	50 μM	2.9-3.2 (hp) 3.3-2.8 (hu)	3.4-3.8 (hp) 3.3-1.7 (hu)	101.6 (ph.) 97.0-103 (p) 96-104 (u)	[77]
PGE	SWAdSV	BRB, pH 10.0	0.4-7.0 nM	0.09 nM	0.30 nM	4.82 (b)	-	103.9 (ph) 90.6-109.1 (u)	[78]
aSPCE	DPV	PBS, pH 7.0	0.01-200 μM	0.006 μM	-	-	-	-	[79]
GPE	DPV	PBS, pH 7.0	1.0-15.0 μM	0.0126 μM	0.0418 μM	3.01	-	95.4-101 (u)	[80]
	SWV			0.0128 μM	0.0427 μM	-	-	-	
NH$_2$/HMS/CPE	DPV	PBS, pH 4.0	0.5-50 μM	0.058 μM	0.19 μM	3.8	4.0	99-108 (w)	[81]

* In this study, N-nitrosopropranolol was detected as the metabolite of propranolol.

In the literature, studies achieved for the electrochemical analysis of ACB were usually performed on the oxidation peak of ACB, except for a study with a hanging mercury drop electrode [77]. The studies were carried out using modified and unmodified electrodes, and the process of ACB on the electrodes was adsorption controlled for some studies [77,78] and diffusion controlled for other studies [79-81]. The widest linearity range and the lowest LOD value were obtained with the pretreated screen-printed electrode [79]. Inter-day and intra-day repeatability values were between 0.78% and 4.825% and were given as RSD%. Accuracy studies were achieved with recovery values, and the results were between 90.6% and 109.0% for pharmaceutical

dosage forms, urine, serum, and real water samples. Recovery values showed that the electrodes and the developed methods could be used for the sensitive determination of ACB without any interference of the excipients.

Possible oxidation and reduction mechanisms of ACB have been discussed in some studies. It has been suggested that the cathodic mechanism of ACB is due to the reduction of the carbonyl group between the methyl and phenyl groups [77]. In the oxidation mechanism of ACB, two different mechanisms have been proposed for the two anodic peaks of ACB. Accordingly, oxidation for the semi-reversible redox mechanism is thought to proceed with the hydroxyl group with 2 electrons and 2 protons. For the other

irreversible redox mechanism, it has been suggested that oxidation results from the breakdown and subsequent oxidation of the molecule [80,81].

3. Conclusions

Propranolol and acebutolol as class II antiarrhythmic agents are beta-blockers and are used in the treatment of supraventricular tachycardias. Voltammetric analysis of propranolol and acebutolol studied with various modified/non-modified electrodes were compiled from the literature. After the supporting electrolyte was selected for the voltammetric analysis of PRP and ACB, scan rate studies were achieved in the studies and it was observed that the redox process of PRP and ACB was generally diffusion-controlled on the electrodes used. Quantitative analysis of drug active ingredients was investigated in terms of some parameters such as linearity range, the limit of detection, stability, repeatability, reproducibility, and sensitivity. The accuracy and precision of the methods were studied using the pharmaceutical dosage forms of propranolol and acebutolol and the results were analyzed. Finally, the voltammetric determination of this drug's active ingredients was carried out using some real samples such as human serum and urine. The results showed that other excipients in real samples did not affect the quantitative analysis of propranolol and acebutolol.

References

[1] J.E. Bager, P. Hjerpe, K. Manhem, S. Bjorck, S. Franzen, A. Rosengren, S.A. Eryd, Treatment of hypertension in old patients without previous cardiovascular disease, J Hypertens, 37, 2019, 2269-2279.

[2] P.K. Whelton, N.R.C. Campbell, D.T. Lackland, G. Parati, C.V.S. Ram, M.A. Weber, X.H. Zhang, Strategies for prevention of cardiovascular disease in adults with hypertension, J Clin Hypertens, 22, 2020, 132-134.

[3] J. Naish, D.S. Court, Medical Sciences, 2. edition, Saunders Ltd, London, 2014, 562.

[4] N.R. Poulter, D. Prabhakaran, M. Caulfield, Hypertension, Lancet, 386, 2015, 801-12.

[5] R. McManus, M. Constanti, C.N. Floyd, M. Glover, A.S. Wierzbicki, Managing cardiovascular disease risk in hypertension, Lancet, 395, 2020, 869-870.

[6] V.P. Arcangelo, A.M. Peterson, Pharmacotherapeutics for Advanced Practice: A Practical Approach (4. edition), 2016, Philadelphia, Lippincott Williams & Wilkins.

[7] T.I. Chang, M.J. Sarnak, Intensive blood pressure targets and kidney disease, Clin J Am Soc Nephro, 13, 2018, 1575-1577.

[8] A. Duni, E. Dounousi, P. Pavlakou, T. Eleftheriadis, V. Liakopoulos, Hypertension in chronic kidney disease: Novel insights, Curr Hypertens Rev, 16, 2020, 45-54.

[9] A.V. Chobanian, G.L. Bakris, H.R. Black, W.C. Cushman, L.A. Green, J.L. Izzo, D.W. Jones, B.J. Materson, S. Oparil, J.T. Wright, E.J. Roccella, Seventh report of the joint national committee on prevention, detection, evaluation, and treatment of high blood pressure, Hypertension, 42, 2003, 1206-1252.

[10] A.S. Go, M.A. Bauman, S.M. Coleman King, G.C. Fonarow, W. Lawrence, K.A. Williams, E. Sanchez, An effective approach to high blood pressure control: A science advisory from the American Heart Association, the American College of Cardiology, and the Centers for Disease Control and Prevention, Hypertension, 63, 2014, 878-85.

[11] C.S. Wiysonge, H.A. Bradley, J. Volmink, B.M. Mayosi, L.H. Opie, Beta-blockers for hypertension, Cochrane Db Syst Rev 1, 2017, CD002003.

[12] S.W. Chan, M. Hu, B. Tomlinson, The pharmacogenetics of beta-adrenergic receptor antagonists in the treatment of hypertension and heart failure, Expert Opin Drug Met, 8, 2012, 767-790.

[13] Y. Agrawal, J.K. Kalavakunta., V. Gupta, Antiarrhythmic agent induced ventricular tachycardia, Am J Ther, 24, 2017, E487-E487.

[14] E.M. Vaughan Williams, A classification of antiarrhythmic actions reassessed after a decade of new drugs, J Clin Pharmacol, 24, 1984, 129-147.

[15] P. Brugada, The Vaughan-Williams classification of antiarrhythmic drugs - Why don't we find its clinical counterpart pace, Pace, 13, 1990, 339-343.

[16] J. Ritter, R. Flower, G. Henderson, H. Rang, Rang and Dale's Pharmacology (7. Edition), 2011, London, Churchill Livingstone.

[17] M. Lei, D.L. Wu, D.A. Terrar, C.L.-H. Huang, Modernized Classification of cardiac antiarrhythmic drugs, Circulation, 138, 2018, 1879-1896.

[18] D.P. Zipes, A consideration of antiarrhythmic therapy, Circulation, 72, 1985, 949-956.

[19] A.A. El-Emam, F.F. Belal, M.A. Moustafa, S.M. El-Ashry, D.T. El-Sherbiny, S.H. Hansen, Spectrophotometric determination of propranolol in formulations via oxidative coupling with 3-methylbenzothiazoline-2-one hydrazone, Farmaco, 58, 2003, 1179-1186.

[20] A. Gölcü, C. Yücesoy, S. Serin, Spectrophotometric determination of some beta-blockers in dosage forms based on complex formation with Cu(II) and Co(II), II Farmaco, 59, 2004, 487-492.

[21] A. Gölcü, New, simple, and validated UV-spectrophotometric method for the estimation of some beta blockers in bulk and formulations, J Anal Chem, 63, 2008, 538-543.

[22] J.M.M. Junior, A.L.H. Muller, E.L. Foletto, A.B. da Costa, C.A. Bizzi, E.I. Muller, Determination of propranolol hydrochloride in pharmaceutical preparations using near infrared spectrometry with fiber optic probe and multivariate calibration methods, J Anal Methods Chem, 2015, 795102.

[23] R. Ghanem, M.A. Bello, M. Callejon, A. Guiratum, Determination of beta-blocker drugs in pharmaceutical preparations by non-suppressed ion chromatography, J Pharmaceut Biomed, 15, 1996, 383-388.

[24] M. Delamoye, C. Duverneuil, F. Paraire, P. de Mazancourt, J.-C. Alvarez, Simultaneous determination of thirteen β-blockers and one metabolite by gradient high-performance liquid chromatography with photodiode-array UV detection, Forensic Sci Int, 141, 2004, 23-31.

[25] H.-B. Lee, K. Sarafin, T.E. Peart, Determination of β-blockers and β2-agonists in sewage by solid-phase extraction and liquid chromatography-tandem mass spectrometry, J Chromatogr A, 1148, 2007, 158-167.

[26] S.A.B. Salman, S.A. Sulaiman, Z. Ismail, S.H. Gan, Quantitative determination of propranolol by ultraviolet HPLC in human plasma, Toxicol Mech Method, 20, 2010, 137-142.

[27] M. Caban, P. Stepnowski, M. Kwiatkowski, N. Migowska, J. Kumirska, Determination of β-blockers and β-agonists using gas chromatography and gas chromatography-mass spectrometry - A comparative study of the derivatization step, J Chromatogr A, 1218, 2011, 8110-8122.

[28] A.A. Salem, I.A.Wasfi, S.S.Al-Nassibi, Trace determination of β-blockers and β2-agonists in distilled and waste-waters using liquid chromatography-tandem mass spectrometry and solid-phase extraction, J Chromatogr B, 908, 2012, 27-38.

[29] S.A. Özkan, B. Uslu, H.Y. Aboul-Enein, Analysis of pharmaceuticals and biological fluids using modern electroanalytical techniques, Crit Rev Anal Chem, 33, 2003, 155-181.

[30] V.K. Gupta, R. Jain, K. Radhapyari, N. Jadon, S. Agarwal, Voltammetric techniques for the assay of pharmaceuticals-A review, Anal Biochem, 408, 2011, 179-196.

[31] O.A. Farghaly, R.S.A. Hameed, A.-A.H. Abu-Nawwas, Electrochemical analysis techniques: A review on recent pharmaceutical applications, Int J Pharm Sci Rev Res, 25, 2014, 37-45.

[32] F. Scholz, Voltammetric techniques of analysis: The essentials, ChemTexts, 1, 2015, 17.

[33] O. Inam, E. Demir, B. Uslu, Voltammetric pathways for the analysis of ophthalmic drugs, Curr Pharm Anal, 16, 2020, 367-391.

[34] A. Vulcu, C. Grosan, L.M. Muresan, S. Pruneanu, L. Olenic, Modified gold electrodes based on thiocytosine/guanine-gold nanoparticles for uric and ascorbic acid determination, Electrochim Acta, 88, 2013, 839-846.

[35] D. Kul, C.M.A. Brett, Electrochemical investigation and determination of levodopa on poly(Nile blue-a)/multiwalled carbon nanotube modified glassy carbon electrodes, Electroanal, 26, 2014, 1320-1325.

[36] P. Krzyczmonik, E. Socha, G. Andrijewski, Determination of ascorbic acid by a composite-modified platinum electrode, Anal Lett, 50, 2017, 806-818.

[37] S. Palanisamy, S.K. Ramaraj, S.-M. Chen, V. Velusamy, T.C.K. Yang, T.-W. Chen, Voltammetric determination of catechol based on a glassy carbon electrode modified with a composite consisting of graphene oxide and polymelamine, Microchim Acta, 184, 2017, 1051-1057.

[38] I. Zablocka, M. Wysocka-Zolopa, K. Winkler, Electrochemical detection of dopamine at a gold electrode modified with a polypyrrole-mesoporous silica molecular sieves (MCM-48) film, Int J Mol Sci, 20, 2019, 111.

[39] H. Sarıoğulları, A. Şenocak, T. Basova, E. Demirbaş, M. Durmuş, Effect of different SWCNT-BODIPY hybrid materials for selective and sensitive electrochemical detection of guanine and adenine, J Electroanal Chem, 840, 2019, 10-20.

[40] E.S. Gomes, F.R.F. Leite, B.R.L. Ferraz, H.A.J.L. Mourão, A.R. Malagutti, Voltammetric sensor based on cobalt-poly(methionine)-modified glassy carbon electrode for determination of estriol hormone in pharmaceuticals and urine, J Pharm Anal, 9, 2019, 347-357.

[41] A. Şenocak, A. Khataee, E. Demirbas, E. Doustkhahd, Ultrasensitive detection of rutin antioxidant through a magnetic micro-mesoporous graphitized carbon wrapped Co nanoarchitecture, Sensor Actuat B-Chem, 312, 2020, 127939.

[42] J.W. Upward, D.G. Waller, C.F. George, Class II antiarrhythmic agents, Pharmacol Therapeut, 37, 1988, 81-109.

[43] W.H. Frishman, β-Adrenergic Blockers, Hypertension (2. edition), A Companion to Brenner and Rector's The Kidney, 2005, Amsterdam, Elsevier Inc.

[44] A.J. Trevor, B.G. Katzung, M. Kruidering-Hall, Katzung & Trevor's Pharmacology Examination & Board Review, 11. edition, 2015, New York, McGraw-Hill Education.

[45] N. Freemantle, J. Cleland, P. Young, J. Mason, J. Harrison, Beta blockade after myocardial infarction: systematic review and meta regression analysis, BMJ, 318, 1999, 1730-1737.

[46] P.A. James, S. Oparil, B.L. Carter, W.C. Cushman, C. Dennison-Himmelfarb, J. Handler, D.T. Lackland, M.L. LeFevre, T.D. MacKenzie, O. Ogedegbe, S.C. Smith, L.P. Svetkey, S.J. Taler, R.R. Townsend, J.T. Wright, A.S. Narva, E. Ortiz, 2014 evidence-based guideline for the management of high blood pressure in adults: Report from the panel members appointed to the Eighth Joint National Committee (JNC 8), JAMA, 311, 2014, 507-520.

[47] E.A. Ushkalova, S.K. Zyryanov, K.E. Zatolochina, A.P. Pereverzev, N.A. Chukhareva, Antiarrhythmic drugs use in elderly patients. Vaughan Williams class I and II drugs, Ration Pharmacother Cardiol, 12, 2016, 471-478.

[48] C. Hocht, F.M. Bertera, J.S. Del Mauro, Y.S. Plantamura, C.A. Taira, A.H. Polizio, What is the real efficacy of beta-blockers for the treatment of essential hypertension?, Curr Pharm Desing, 23, 2017, 4658-4677.

[49] J.M. Cruickshank, The Role of Beta-Blockers in The Treatment of Hypertension, Hypertension: From Basic Research to Clinical Practice, Advances in Experimental Medicine and Biology, Editor: M.S. Islam, 956, 2016, Springer, Cham.

[50] T.K. Morgan, R. Lis, W.C. Lumma, R.A. Wohl, K. Nickisch, G.B. Phillips, J.M. Lind, J.W. Lampe, S.V. Di Meo, H.J. Reiser, T.M. Argentieri, M.E. Sullivan, E. Camtor, Synthesis and pharmacological studies of N-[4-[2-hydroxy-3-[[2-[4-(1H-imidazol-1-Yl)phenoxy]ethyl]amino]propoxy]phenyl] methanesulfonamide, a novel antiarrhythmic agent with class II and class III activities, J Med Chem, 33, 1990, 1087-1990.

[51] L.L. Brunton, J.S. Lazo, K.L. Parker, The pharmacological basis of therapeutics (11. edition), 2006, New York, McGraw-Hill Education.

[52] D. Ladage, R.H.G. Schwinger, K. Brixius, Cardio-selective beta-blocker: Pharmacological evidence and their influence on exercise capacity, Cardiovasc Ther, 31, 2013, 76-83.

[53] K.Y. Xu, E.D.P. Campbell, S.S. Gill, R. Nesdole, R.J. Campbell, Impact of combination glaucoma therapies on beta-blocker exposure, J Glaucoma 26, 2017, E107-E109.

[54] A.V. Srinivasan, Propranolol: A 50-year historical perspective, Ann Indian Acad Neur, 22, 2019, 21-26.

[55] P.R. Kowey, Pharmacological effects of antiarrhythmic drugs, Arch Intern Med, 158, 1998, 325-332.

[56] R. Mehvar, D.R. Brocks, Stereospecific pharmacokinetics and pharmacodynamics of beta-adrenergic blockers in humans, J Pharm Pharm Sci, 4, 2001, 185-200.

[57] W.H. Frishman, M. Alwarshetty, Beta-adrenergic blockers in systemic hypertension - Pharmacokinetic considerations related to the current guidelines, Clin Pharmacokinet, 41, 2002, 505-516.

[58] B. Terhaag, Clinical pharmacokinetics of the beta-receptor blockers propranolol and talinolol, Z Klin Med, 44, 1989, 119-124.

[59] A. Corletto, H. Frohlich, T. Tager, M. Hochadel, R. Zahn, C. Kilkowski, R. Winkler, J. Senges, H.A. Katus, L. Frankenstein, Beta blockers and chronic heart failure patients: Prognostic impact of a dose targeted beta blocker therapy vs. heart rate targeted strategy, Clin Res Cardiol, 107, 2018, 1040-1049.

[60] B.G. Katzung, Basic and Clinical Pharmacology (4. edition), Editors: M. Weitz and P. Boyle 2020, New York, McGraw-Hill Education.

[61] J.B. Schwartz, D. Keefe, D.C. Harrison, Adverse effects of antiarrhythmic drugs, Drugs, 21, 1981, 23-45.

[62] W. Amjad, W. Qureshi, A. Farooq, U. Sohail, S. Khatoon, S. Pervaiz, P. Narra, S.M. Hasan, F. Ali, A. Ullah, S. Guttmann, Gastrointestinal side effects of antiarrhythmic medications: A review of current literature, Cureus, 9, 2017, e1646.

[63] Z. Kun, Y. Shuai, T. Dongmei, Z. Yuyang, Electrochemical behavior of propranolol hydrochloride in neutral solution on calixarene/multi-walled carbon nanotubes modified glassy carbon electrode, J Electroanal Chem, 709, 2013, 99-105.

[64] N.A. Alarfaj, M.F. El-Tohamy, Construction and validation of new electrochemical carbon nanotubes sensors for determination of acebutolol hydrochloride in pharmaceuticals and biological fluids, J Chin Chem Soc, 61, 2014, 910-920.

[65] J.S. Choi, J.P. Burm, Pharmacokinetics of acebutolol and its main metabolite, diacetolol after oral administration of acebutolol in rabbits with carbon tetrachloride-induced hepatic failure, Arch Pharm Res, 25, 2002, 541-545.

[66] R.R. Gaichore, A.K. Srivastava, Electrocatalytic determination of propranolol hydrochloride at carbon paste electrode based on multiwalled carbon-nanotubes and c-cyclodextrin, J Incl Phenom Macro, 78, 2014, 195-206.

[67] M. Raj, P. Gupta, N.R. Goyal, Poly-Melamine film modified sensor for the sensitive and selective determination of propranolol, a β-blocker in biological fluids, J Electrochem Soc, 163, 2016, H388-H394.

[68] P. Gupta, K.S. Yadav, B. Agrawal, N.R. Goyal, A novel graphene and conductive polymer modified pyrolyticgraphite sensor for determination of propranolol in biological fluids, Sensor Actuat B-Chem, 204, 2014, 791-798.

[69] Z. Kun, H. Yi, Z. Chengyun, Y. Yue, Z. Shuliang, Y. Yuyang, Electrochemical behavior of propranolol hydrochloride in neutral solution on platinum nanoparticles doped multi-walled carbon nanotubes modified glassycarbon electrode, Electrochim Acta, 80, 2012, 405-412.

[70] T. Alizadeh, L. Allahyari, Highly-selective determination of carcinogenic derivative ofpropranolol by using a carbon paste electrode incorporated withnano-sized propranolol-imprinted polymer, Electrochim Acta, 111, 2013, 663-673.

[71] H.T. Purushothama, Y.A. Nayaka, Electrochemical determination of propranolol using reduced graphene oxide modified carbon paste electrode, Anal Bioanal Electrochem, 11, 2019, 1575-1589.

[72] S.Z. Mohammadi, S. Tajik, H. Beitollahi, Electrochemical determination of propranolol by using modified screen-printed electrodes, Indian J Chem Techn, 27, 2020, 73-78.

[73] T. Łuczak, A nanogold supported inorganic/organic hybrid 3D sensor for electrochemical quantification of propranolol-effective antagonist of β-adrenergic receptors, Ionics, 25, 2019, 5515-5525.

[74] M.R. Nateghi, Synthesis of (Ti0.5V0.5)3C2 as novel electrocatalyst to modify carbon paste electrode for measurement of propranolol in real samples, Russ J Electrochem, 55, 2019, 106-115.

[75] E.R. Sartori, R.A. Medeiros, R.C. Rocha-Filho, O. Fatibello-Filho, Square-wave voltammetric determination of propranolol and atenolol in pharmaceuticals using a boron-doped diamond electrode, Talanta, 81, 2010, 1418-1424.

[76] Z. Kun, C. Hongtao, Y. Yue, B. Zhihong, L. Fangzheng, L. Sanming, Platinum nanoparticle-doped multiwalled carbon-nanotube-modified glassy carbon electrode as a sensor for

[77] A.F. Al-Ghamdi, M.M. Hefnawy, A.A. Al-Majed, F.F. Belal, Development of square-wave adsorptive stripping voltammetric method for determination of acebutolol in pharmaceutical formulations and biological fluids, Chem Cent J, 6, 2012, 15.

[78] A. Levent, Voltammetric behavior of acebutolol on pencil graphite electrode: Highly sensitive determination in real samples by square-wave anodic stripping voltammetry, J Iran Chem Soc, 14, 2017, 2495-2502.

[79] A. Yamuna, P. Sundaresan, S.M. Chen, S.R.M. Sayed, T.W. Chen, S.P. Rwei, X. Liu, Electrochemical determination of acebutolol on the electrochemically pretreated screen printed carbon electrode, Int J Electrochem Sc, 14, 2019, 6168-6178.

[80] A.M. Bagoji, S.M. Patil, T.S. Nandibewoor, Electroanalysis of cardioselective betaadrenoreceptor blocking agent acebutolol by disposable graphite pencil electrodes with detailed redox mechanism, Cogent Chem, 2, 2016, 1172393.

[81] M. Silva, S. Morenta-Zarcero, D. Pérez-Quintanilla, I. Sierra, Simultaneous determination of pindolol, acebutolol and metoprolol in waters by differential-pulse voltammetry using an efficient sensor based on carbon paste electrode modified with amino-functionalized mesostructured silica, Sensor Actuat B-Chem, 283, 2019, 434-442.

simultaneous determination of atenolol and propranolol in neutral solution, Ionics, 21, 2015, 1129-1140.

Turkish Journal of

Analytical Chemistry

www.turkjac.org
2019

TurkJAC

Carbon dots applications in electrochemical and electrochemiluminescence sensors: Some examples of pathogen sensors

Saliha Dinç[1*] (iD), Rabia Serpil Günhan[2] (iD)

[1]Selcuk University, Cumra School of Applied Sciences, Konya, Turkey
[2]Konya Technical University, Vocational School of Technical Sciences, Konya, Turkey

Abstract

The ongoing worldwide pandemic of the novel severe acute respiratory syndrome coronavirus 2 (SARS-CoV-2) has revealed that simple, fast, low-cost, reliable, and portable sensor systems should be developed immediately. Electrochemical and electrochemiluminescence (ECL) based pathogen sensors are promising alternatives to conventional methods due to several advantages including in situ and fast response time, high sensitivity, low cost, being portable, easy-to-operate and simple to construct using different receptors including, antibody, enzyme, DNA, aptamer, etc. Carbon dots/graphene quantum dots have been used as labels, electrode material, ECL luminophores, electrode modification materials, amplifier, reaction catalysts to increase sensitivity and selectivity of electrochemical and ECL sensors. In this mini-review, the latest applications of carbon dots in electrochemical and ECL based sensors are summarized and some examples of pathogen sensors are given.

Keywords: Carbon dots, electrochemistry, electrochemiluminescence, biosensor, pathogen

1. Introduction

Even today, one of the threats to the life and health system is the pandemic or infection caused by pathogen microorganisms. Approximately 1400 known species, which are primarily water and foodborne microorganisms, are considered as human pathogens [1]. However, novel species may emerge as a worldwide hazard from now to tomorrow. For example, severe acute respiratory syndrome coronavirus 2 (SARS-CoV-2), which has emerged in China in December 2019, now still leads to cause a global pandemic. The ongoing outbreak of SARS-CoV-2 infection throughout the world has revealed that the virus should be diagnosed at the earliest appearance of symptoms. To control or cease the contagion of viruses, viruses should be detected not only in health laboratories but also directly in places where humans circulate and spread the virus such as airports, trains, boats, and any public aggregation places [2]. Therefore, simple, fast, low-cost, reliable, and portable sensor systems should be developed immediately for SARS-COV-2, which is also an important requirement for all pathogens including

bacteria, viruses, and fungi [2]. Because culture-based methods considered as the gold standard for most pathogens are frequently time-consuming and laborious [3]. Similarly, molecular methods including enzyme-linked immunosorbent assay (ELISA) and polymerase chain reaction (PCR) frequently require trained staff to perform the complex assays [4].

The electrochemical sensor, a device detects the concentration of target molecules in real-time by measuring electrical signals generated by biological, chemical, or physical events between target and sensor surface. Various recognition elements including enzymes, proteins, antibodies, MIP, etc. are immobilized onto the electrode via different chemical modification methods [5,6]. The electrical signal monitored by electrode can be current, voltage or impedance, etc. So far, electrochemical sensors have been applied to various fields including clinical, food, environment and drug analysis [7], due to their several advantages such as in situ and fast response time, high sensitivity, low cost, being portable, easy-to-operate and simple to construct [8-10]. Among

applications of electrochemical sensors, pathogen detection is one of the remarkable applications that enable the before-mentioned advantages as well as shortening of analysis time. Up to now, different electrochemical biosensors were developed for rapid, direct (without sample preparation) and in situ detection of foodborne, waterborne, or human pathogens [11].

With the emergence of nanoscience and nanotechnology, nanomaterial has been used as a signal amplification to increase the sensitivity and selectivity of electrochemical sensors [8, 10]. Among nanoparticles, carbon nanoparticles especially carbon nanotubes and graphene are considered as cornerstone owing to their outstanding properties. Non-toxicity, biocompatibility, high effective surface area, superior electrical conductivity, mechanical strength, and electrocatalytic activity are considered some of these unique properties. Thanks to these properties, they are successfully adapted for the development of electrochemical sensors [10,12]. However, their manufacturing techniques are difficult and expensive [13].

Carbon quantum dots or graphene quantum dots are defined as luminescent nanoparticles with dimensions less than 10 nm [14-16]. Due to their biocompatibility, low toxicity, water/organic solubility, photostability, green and simple synthesis, chemically stability, good disparity, etc., they are assessed as a potential non-toxic alternative to traditional semiconductor quantum dots [17-19]. Recent studies showed that carbon dots and graphene quantum dots, zero-dimensional carbon-based nanostructures, can substitute graphene and graphene oxides because of their own aforementioned superior properties including enhanced electrocatalytic activity [13]. Furthermore, compared to natural enzymes, CDs have broader pH stability and are stable at different temperature ranges. Their large surface area enables them to immobilize a higher ratio of protein, enzymes, and antibodies by simple adsorption or other techniques. Besides, various functional groups on their surface facilitate the attachment of biomolecules. By taking into account all the above considerations, CDs can increase the precision and accuracy of biosensors. Ironically, the utilization of CDs as a signal amplifier or electrode modifiers for the development of electrochemical biosensors has not widely been investigated and still remains undeveloped [13].

Electrochemiluminescence (ECL) is defined as the production of light resulted from the electrochemical reaction that high-energy electron transfer reactions occurred between electron-donors and acceptors generate excited state and then light emission is formed [20]. Since ECL sensors merge the advantages of chemiluminescence and electrochemical sensors, ECL sensors possess many assets such as high sensitivity and selectivity, low background signal, easy reaction control and simple instrumentation, broad working range [21,22]. ECL sensors have been applied to clinical diagnostics, environmental assays, food analysis, etc. until now [23]. Carbon dots/graphene quantum dots show electrochemiluminescence properties [24] and can be used as ECL luminophores [25]. Therefore, integrating graphene quantum dots/carbon dots with ECL sensors platform have led to developing novel biosensors with high sensitivity and selectivity and expanded the applications of carbon dots/graphene quantum dots as well [25].

The aim of this mini-review is to present some examples from the latest applications of carbon dots in electrochemical / ECL based sensors and pathogen sensors.

2. Electrochemical sensors

In electrochemical sensors, carbon dots/graphene quantum dots employed as labels or electrode material can accelerate charge transport and redox reactions, enhance selectivity, conductivity, stability, and reproducibility of sensors. So, they are considered as indispensable components of high performing electrochemical sensors [26]. Recently, instead of carbon dots/graphene quantum dots, their nanocomposites with different structures that are carbon nanotubes, graphene, chitosan, and metal components, etc. are preferred in electrochemical sensor design [27].

Carbon dots/graphene quantum dots are not yet actively integrated with conductometric and potentiometric sensors by virtue of low-sensitivity, less-stability, less-specificity, and inaccuracy. However, their utilization in the voltammetric, amperometric, and impedimetric sensor is common compared with others [28]. Some sensor applications of carbon dots/graphene quantum dots are given in the following.

2.1. Amperometric sensors
Applications of carbon dots in amperometric sensors have recently been explored in the determination of different analytes. Carbon dots/graphene quantum dots have been used in the modification of the carbon paste electrode to increase the electrocatalytic power

of the sensor. For example, carbon dots synthesized from carbon soot were utilized for chronoamperometic detection of adrenaline which acts as a neurotransmitter with an important role in respiration, energy metabolism, etc., in physiological conditions [29,30]. Compared to the bare carbon paste electrode, the modification with carbon dots catalyzed the electrochemical reaction of adrenaline and enabled the simultaneous determination of adrenaline, ascorbic acid, and serotonin via functional groups of carbon dots including hydroxyl groups. Selective determination of adrenaline was achieved with a detection limit of 6 nM [30].

In a study, carbon paste electrode was modified with carbon dots extracted from sugar beet molasses [14] and then the enzymatic detection of neurotransmitter acetylcholine was achieved with this electrode. Carbon dots were used as nanozymes in this amperometric sensor due to peroxidase-mimicking behavior. Hydrogen peroxide formed from acetylcholine in the presence of acetylcholinesterase and choline oxidase enzymes was broken down by carbon dots with similar behavior of peroxidase. In addition, carbon dots provided higher immobilization ratio of enzymes on the electrode. The prepared sensor might easily detect lower level of acetylcholine (LOD: 5 nM) [31].

Carbon dots have been utilized in nanocomposites with other nanoparticles or compounds in the amperometric sensors to increase the precision and accuracy of sensors. The application of a glassy carbon electrode modified with a nanocomposite composed of aminated graphene quantum dots, thiolated β-cyclodextrin, and gold nanoparticles reported for analysis of quercetin has been reported [32]. The sensor selectively detected quercetin at the linear response range of 1-210 nM with a lower detection limit of 285 pM even in the presence of flavonoids having the similar structure of quercetin [32]. For the detection of glucose, a nanocomposite containing carbon dots and copper oxide was synthesized and used to develop a non-enzymatic amperometric sensor [33]. The copper oxide was used as an enzyme to oxidase glucose. The synergistic effects of copper oxide and carbon dots enhanced the electrochemical performance of the sensor. However, the reported limit of detection (0.2 mM) is not very low.

2.1.1. Amperometric pathogen sensors

As one of the major global health threats, chronic hepatitis B viruses cause chronic infection, cirrhosis, and liver cancer [34,35]. Yan et. al. [35] developed an amperometric immunosensor for the early diagnosis of hepatitis B viruses by detecting the hepatitis B surface antigen. In this research, a nanocomposite containing nitrogen-doped graphene quantum dots, palladium, gold, copper, and the electroactive polymer was synthesized as a signal amplification platform to design label-free electrochemical immunosensor. Nitrogen-doped graphene quantum dots were used as support material and reducing agents of gold, palladium, and copper. The catalytic activity of nitrogen-doped graphene quantum dots for the decomposition of hydrogen peroxide increased with other metal nanoparticles. Thus, the effects of hindering electron transport resulted from increasing antigen concentration were reduced. Eventually, the study reported the lowest linear range and limit of detection among previously developed electrochemical sensors (Table 1) [35].

Graphene quantum dots can be a promising alternative to horseradish peroxidase having some drawbacks including difficulties in immobilization and high-cost [36,37]. An amperometric immunosensor for the detection of *Yersinia enterocolitica* which causes foodborne-zoonotic infection via contaminated food and water including especially raw or undercooked meat was fabricated by Savaş and Altintas [37]. In this study, graphene quantum dots laminated on the gold electrode were used as nanozyme instead of horseradish peroxidase due to their peroxidase mimicking properties [37]. The increase in the amperometric signal was arrived at the mA range because of the interplay between gold and graphene quantum dots [37].

2.2. Voltammetric sensors

In literature, applications of carbon dots in voltammetric sensors have been more common compared to amperometric and impedimetric sensors. Carbon dots/graphene quantum dots have been utilized as a signal amplifier with other nanomaterials, conductive polymers, or compounds.

Arumugasamy et al. [38] designed an electrochemical dopamine sensor that graphene quantum dots were incorporated in multiwalled carbon nanotube and this nanocomposite was utilized for rapid, simple, and sensitive detection of dopamine. Carboxyl groups of graphene quantum dots significantly raised electrochemically active surface area of the electrode. The limit of detection (LOD) and the linear range was reported as 95 nM and 0.25-250 μM respectively [38].

In another work, Jahani et al. [39] developed a voltammetric sensor for the simultaneous

determination of norepinephrine and acetylcholine using graphene quantum dots and ionic liquids together. In this research, the combination of graphene quantum dots and ionic liquid dramatically increased the current compared to a single utilization of them. Furthermore, this binary provided two separate oxidation peaks belongs to norepinephrine and acetylcholine. The LOD value was reported as 0.06 μM for norepinephrine [39].

A voltammetric immunosensor was constructed using polyaniline functionalized graphene quantum dots which enables good conductivity was used to determine heat shock protein 70, which is a biomarker of early screening of depression [40]. The detection limit of this method (0.05 ng mL^{-1}) was reported as lower than that of Enzyme-Linked ImmunoSorbent Assay (ELISA) (0.47 ng mL^{-1}) thanks to the higher electrocatalytic activity of polyaniline functionalized graphene quantum dots [40].

Tian et al. [41] fabricated a voltammetric sensor using a nanocomposite containing amino-functionalized graphene quantum dots and conductive polymer for the detection of mercury with low LOD (0.00006 nM) [41].

The accuracy of a sensor depends on the immobilization of receptor molecules on the electrode surface. In this sense, various functional groups of carbon dots/graphene quantum dots facilitate the attachment of receptor molecules. Besides, their large surface area increases receptor loading. In a study reported by Majumdar et al. [42], DNA was immobilized on the surface of carbon dots for the detection of mutagenic, carcinogenic nitrosamines. Carbon dots ensured multiple binding sites for DNA due to larger surface area and various surface functionalities. Selective determination of nitrosamine was achieved with lower LOD (9.9 nM) than those of commercial methods including chromatography (μM) [42].

2.2.1. Voltammetric pathogen sensors
Similar to Majumdar et al. [42], Xiang et al. [43] developed a voltammetric sensor for the detection of hepatitis B viruses in which single-stranded DNA was immobilized on graphene quantum dots based on the strong interaction between graphene quantum dots and single-stranded DNA, as a probe. In this study, the signal of electroactive indicator ($K_3[Fe(CN)_6]$) decreased when the probe was strongly bound to graphene quantum dots. However, the signal increased when the hepatitis DNA was bound to probe. By taking into account the increase in signal,

the concentration of the virus was detected with the detection limit of 1 nM (Table 1) [43].

Doping of carbon dots/graphene quantum dots with different compounds leads to new ways for novel applications. For example, Valipour and Roushani [44] synthesized a nanocomposite composed of thiol doped graphene quantum dots and silver nanoparticles in immunosensor for the hepatitis C virus (Table 1). To load more antibodies, silver nanoparticles were covalently bound to thiol doped graphene quantum dots on the glassy carbon electrode. In this research, thiol doped graphene quantum dots utilized as intermediator to immobilize antibody owing to their large surface area and biocompatibility [44].

2.3. Impedimetric sensors
Carbon dots/graphene quantum dots are used for immobilization of receptors including aptamers. For example, Abazar and Noorbakhsh [45] constructed an impedimetric aptasensor for the detection of insulin using a nanocomposite composed of carbon dots and chitosan. In this study, carbon dots were dispersed in chitosan to prevent agglomeration. The synthesized nanocomposite was used as a platform for covalent immobilization of aptamer and fabrication of insulin sensor. A detection limit of 106.8 pM was reported with a linear range of 0.5-10 nM [45].

In recent years, an increase in the usage of antibiotics for nonbacterial infections as feed additives has created antibiotic resistance, threatening the world. Antibiotic resistance is an important issue in both the management of infections and food safety. Ye et al. [46] developed an impedimetric biosensor for rapid and sensitive detection of bacterial response to antibiotics. In this research, graphene quantum dots were conjugated with Salmonella antibody and immobilized on the alumina membrane. This electrochemical sensing platform was used to capture bacteria. After then, the antibiotics, enrofloxacin, and ampicillin were contacted on the sensor. Bacterial response to antibiotics was determined rapidly according to the change in the impedance signal. The authors reported that graphene quantum dots provided enhanced sensitivity and low detection limit (pM level) [46].

2.3.1. Impedimetric pathogen sensors
An impedimetric immunosensor was constructed for the detection of the hepatitis E virus, causing acute viral hepatitis worldwide. Nitrogen and thiol doped graphene quantum dots and gold-embedded

polyaniline wires were deposited on the glassy carbon electrode (Table 1). Nitrogen and thiol doped graphene quantum dots ensured to conjugate antibodies using EDC-NHS chemistry to amplify electrochemical activity and to provide their adsorption onto gold nanoparticles. The sensor determined the hepatitis E virus selectively at the femtogram level in the presence of other viruses, serum, and even in the culture medium [47].

3.   ECL sensors

Owing to their unique properties, especially electrochemical properties, carbon dots/graphene quantum dots can be used as ECL luminophores (Fig. 1), electrode modification materials, amplifier, reaction catalysts, etc. in the development of ECL biosensors [21].
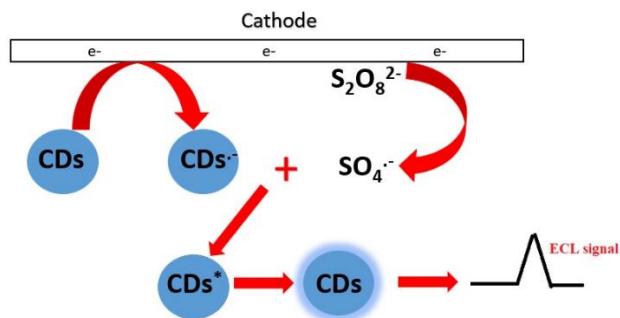

Figure 1. Illustration of carbon dots utilized as ECL luminophore in the presence of persulfate.

ECL properties of carbon dots were discovered in 2009 by Zhu et al. [48]. In this research, carbon dots were synthesized from glucose and polyethylene glycol (PEG-200) via the microwave pyrolysis method. After discovery, ECL sensors were developed using carbon dots/graphene quantum dots for the detection of metals ions, protein, DNA/RNA, folic acid, nitride, atrazine, lincomycin, tetracycline, etc. [21,27,49-54]. In addition, carbon dots/graphene quantum dots based ECL sensors were fabricated for the determination of cancer cells, enzyme activity, or pathogen microorganisms [21,55,56]. Some examples of ECL sensors published in 2020 are given as follows.

Yang et al. [57] developed a sandwich-type ECL sensor for the detection of prostate-specific antigen, a significant biomarker of prostate cancer. In this research, two antibodies for the recognition of antigens were used. The primary antibody (Ab1) was immobilized through an amide bond between the antibody and the nanocomposite (1) composed of poly (indole-6-carboxylic acid)/flower-like gold nanoparticles on the glassy carbon electrode.

Secondary antibody (Ab2) was attached to the nanocomposite (2) containing gold nanoparticles, graphene quantum dots on the poly (etherimide)-graphene oxide. When these two antibodies were bound to a prostate-specific antigen, ECL signal was formed through luminescent graphene quantum dots under applied voltage to the glassy carbon electrode. ECL signal was amplified very strong thanks to the synergistic effects between the nanocomposite (1) and the nanocomposite (2). The strong ECL signal gave an improvement in the sensitivity of the sensor with the detection limit of 0.44 pg mL^{-1} [57].

Raju et al. [58] developed an ECL sensor for the detection of copper ions in which phosphorus-doped carbon dots was utilized as a luminophore. The authors reported that phosphorus-doped carbon dots gave a strong ECL signal compared to bare carbon dots. The detection limit was measured as 0.27 nM for this sensor with the range of 1-1000 nM [58].

In another study, ECL immunosensor for okadaic acid, being diarrhetic shellfish poison was developed using phosphor and sulfur-doped carbon dots [59]. Co-doped carbon dots showed the best ECL performance among bare, mono-doped carbon dots. The linear working range and detection limit were reported as 0.01-20 ng mL^{-1} and 0.005 ng mL^{-1}, respectively [59].

Apart from the utilization of carbon dots/graphene quantum dots as luminophore, Kalaiyarasan et al. [60] used aminated carbon quantum dots as co-reactant for Ru(bpy)$_3^{2+}$. While ECL intensity of Ru(bpy)$_3^{2+}$ decreased with butein, a plant polyphenol, in the presence of aminated carbon dots there was no change in the case of commercial co-reactants [60].

3.1. ECL pathogen sensors
Escherichia coli O157:H7 as one of the major foodborne pathogens, causes severe and fatal diseases including hemorrhagic colitis (HC) and hemolytic uremic syndrome (HUS) especially in young and immunocompromised peoples. Chen et al. [61] reported an easily prepared ECL sensor for the detection of *Escherichia coli* O157:H7. In this report, nitrogen-doped graphene quantum dots were synthesized instead of bare dots to enhance ECL efficiency (Table 1) [21]. *Escherichia coli* O157:H7 recognition and binding were performed with poly-dopamine surface imprinted polymer synthesized via electropolymerization method. In this approach, nitrogen-doped graphene quantum dots labeled with *E. coli* O157:H7 polyclonal antibody used as luminophore to give strong ECL activity with co-

reactant (potassium persulfate) on the glassy carbon electrode [61].

Table 1. Carbon dots based electrochemical and ECL sensors for detection of pathogen species (ECL: Electrochemiluminescence)

Target Pathogen	Method	Receptor	Working electrode/ ECL luminophore	Synthesis of carbon dots	Linear working range	LOD	Ref.
Hepatitis B	Amperometry	Surface antigen	A nanocomposite composed of nitrogen doped graphene quantum dots, palladium, gold, copper and electroactive polymer on glassy carbon electrode	Hydrothermal method using citric acid and dicyandiamide (180 °C- 12 h)	10 fg mL^{-1} - 50 ng mL^{-1}	3.3 fg mL^{-1}	[35]
Yersinia enterocolitica	Amperometry	Monoclonal antibody	Graphene quantum dots laminated on the gold electrode	Commercial	1- 6.23 x10^{-8} cfu mL^{-1}	5-cfu mL^{-1} for milk 30-cfu mL^{-1} for serum	[37]
Hepatitis B	Voltammetry	Single stranded DNA	Graphene quantum dots modified glassy carbon electrode	Pyrolysis using citric acid (200 °C)	10-500 nM	1 nM	[43]
Hepatitis C	Voltammetry	Antibody	A nanocomposite composed of thiol doped graphene quantum dots and silver nanoparticles on glassy carbon electrode	Acid oxidation using multiwalled carbon nanotube	0.05 pg mL^{-1} - 60 ng mL^{-1}	3 fg mL^{-1}	[44]
Hepatitis E	Impedimetric	Antibody	Nitrogen and thiol doped graphene quantum dots and gold- embedded polyaniline wires on the glassy carbon electrode	Hydrothermal method using citric acid and thiourea (160 °C- 4 h)	10^{-12} -10^{-15} g mL^{-1}	8 x 10^{-14} g mL^{-1}	[47]
Escherichia coli O157:H7	ECL	Poly-dopamine surface imprinted polymer and antibody	Nitrogen doped graphene quantum dots were used ECL luminophore	Hydrothermal method using critic acid and ammonia	10 -10^7 cfu mL^{-1}	8 cfu mL^{-1}	[61]
Escherichia coli	ECL	Antibody	A nanocomposite composed of graphene quantum dots and silver nanoparticles used as luminescence enhancer	Commercial	10 -10^7 cfu mL^{-1}	5 cfu mL^{-1}	[62]

In another study issued by Li et al. [62], a smartphone-based ECL system was developed for the detection of Escherichia coli using an antigen-antibody relationship.Ç Silver nanoparticles were adsorbed on the graphene quantum dots to amplify the ECL signal and this nanocomposite was used as a luminescence enhancer in tris(2,2′-bipyridyl)ruthenium (II)/tripropylamine (Ru(bpy)$_3$ $^{2+}$/TPA) assay (Table 1). Generated ECL signal was caught with the smartphone camera and was measured by image analysis application during analysis [62]. The researchers pointed out that the portable device constructed in the research can be suitable for point of care testing (POCT) [62].

4. Summary and future works

Nowadays, infections and pandemics caused by pathogens are continuing to threaten the world. Besides, a novel pathogen may emerge as a global threat at any moment as in coronavirus pandemic.

The ongoing outbreak of SARS-CoV-2 global infection has proved the need for reliable, selective, rapid, easily accessible, portable, and low-cost diagnostic methods for the detection of pathogens. Electrochemical and electrochemiluminescence (ECL) based pathogen sensors are promising alternatives with respect to conventional methods because they offer several advantages including in situ and fast response time, high sensitivity, low cost, being portable, easy-to-operate and simple to construct. As rising stars of carbon-based nanoparticles, carbon dots/graphene quantum dots have been used as labels, electrode material, ECL luminophores, electrode modification materials, amplifiers, and reaction catalysts to increase sensitivity and selectivity of electrochemical and ECL sensors. This mini-review highlights the applications of carbon dots in the electrochemical and ECL pathogen sensors and tries to draw attention to this subject, for future studies as well.

References

[1] B.D. Mansuriya, Z. Altintas, Graphene quantum dot-based electrochemical immunosensors for biomedical applications, Materials, 13, 2020, 96.

[2] F. Martinelli, A. Perrone, I. Della Noce, L. Colombo, S. Lo Priore, S. Romano, Application of a portable instrument for rapid and reliable detection of SARS-CoV-2 infection in any environment, Immunol Rev, 295, 2020, 4-10.

[3] J. Shen, T. Zhou, R. Huang, Recent advances in electrochemiluminescence sensors for pathogenic bacteria detection, Micromachines, 10, 2019, 592.

[4] M. Amiri, A. Bezaatpour, H. Jafari, R. Boukherroub, S. Szunerits, electro-chemical methodologies for the detection of pathogens, ACS Sensors, 3(6), 2018, 1069-1086.

[5] I.H. Cho, D.H. Kim, S. Park, Electrochemical biosensors: Perspective on functional nanomaterials for on-site analysis, Biomater Res, 24, 2020, 6.

[6] A.A. Lahcen A. Amine, Recent advances in electrochemical sensors based on molecularly imprinted polymers and nanomaterials, Electroanal, 31(2), 2019, 188-201.

[7] Y. Wang, H. Xu, J. Zhang, G. Li, Electrochemical sensors for clinic analysis, Sensors, 8, 2008, 2043-2081.

[8] C. Zhu, G. Yang, H. Li, D. Du, Y. Lin, Electrochemical sensors and biosensors based on nanomaterials and nanostructures, Anal Chem, 87(1), 2015, 230-49.

[9] F.T.C. Moreira, M.G.F. Sale, M. Di Lorenzo, Towards timely Alzheimer diagnosis: A self-powered amperometric biosensor for the neurotransmitter acetylcholine, Biosens Bioelectron, 87, 2017, 607-614.

[10] E. Asadian, M. Ghalkhani, S. Shahrokhian, Electrochemical sensing based on carbon nanoparticles: A review, Sensor Actuat B-Chem, 293, 2019, 183-209.

[11] E. Cesewski B.N. Johnson, Electrochemical biosensors for pathogen detection, Biosens Bioelectron, 159, 2020, 112214.

[12] S. Muniandy, S.J. Teh, K.L. Thong, A. Thiha, I.J. Dinshaw, C.W. Lai, F. Ibrahim, B.F. Leo, Carbon nanomaterial-based electrochemical biosensors for foodborne bacterial detection, Crit Rev Anal Chem, 49(6), 2019, 510-533.

[13] S. Campuzano, P. Yanez-Sedeno, J.M. Pingarron, Carbon dots and graphene quantum dots in electrochemical biosensing, Nanomaterials, 9(4), 2019, 634.

[14] S. Dinç, A simple and green extraction of carbon dots from sugar beet molasses: Biosensor applications, Sugar Ind, 141(9), 2016, 560-564.

[15] Y. Li, Y. Zhong, Y. Zhang, W. Weng, S. Li, Carbon quantum dots/octahedral Cu_2O nanocomposites for non-enzymatic glucose and hydrogen peroxide amperometric sensor, Sensor Actuat B-Chem, 206, 2015, 735-743.

[16] A. Gümrükçüoğlu, A. Başoğlu, S. Kolayli, S. Dinç, M. Kara, M. Ocak, Ü. Ocak, Highly sensitive fluorometric method based on nitrogen-doped carbon dot clusters for tartrazine determination in cookies samples, Turkish J Chem, 44(1), 2020, 99-111.

[17] S. Hill M.C. Galan, Fluorescent carbon dots from mono- and polysaccharides: Synthesis, properties and applications, Beilstein J Org Chem, 13, 2017, 675-693.

[18] S. Dinç, M. Kara, M. Demirel Kars, F. Aykül, H. Çiçekci, M. Akkuş, Biocompatible yogurt carbon dots: Evaluation of utilization for medical applications, Appl Phys A, 123(9), 2017, 572.

[19] X. Li, S. Zhang, S.A. Kulinich, Y. Liu, H. Zeng, Engineering surface states of carbon dots to achieve controllable luminescence for solid-luminescent composites and sensitive Be^{2+} detection, Sci Rep-UK, 4, 2014, 4976.

[20] L. Benoit J.-P. Choi, Electrogenerated chemiluminescence of semiconductor nanoparticles and their applications in biosensors, Chemelectrochem, 4(7), 2017, 1573-1586.

[21] Y. Chen, Y. Cao, C. Ma, J.-J. Zhu, Carbon-based dots for electrochemiluminescence sensing, Mater Chem Front, 4(2), 2020, 369-385.

[22] Y. Zhang, R. Zhang, X. Yang, H. Qi, C. Zhang, Recent advances in electrogenerated chemiluminescence biosensing methods for pharmaceuticals, J Pharm Anal, 9(1), 2019, 9-19.

[23] M.M. Richter, Electrochemiluminescence (ECL), Chem Rev, 104, 2004, 3003-3036.

[24] L. Li, G. Wu, G. Yang, J. Peng, J. Zhao, J.J. Zhu, Focusing on luminescent graphene quantum dots: Current status and future perspectives, Nanoscale, 5(10), 2013, 4015-39.

[25] Y. Xu, J. Liu, C. Gao, E. Wang, Applications of carbon quantum dots in electrochemiluminescence: A mini review, Electrochem Commun, 48, 2014, 151-154.

[26] K. Nekoueian, M. Amiri, M. Sillanpaa, F. Marken, R. Boukherroub, S. Szunerits, Carbon-based quantum particles: An electroanalytical and biomedical perspective, Chem Soc Rev, 48(15), 2019, 4281-4316.

[27] Z. Zhuang, H. Lin, X. Zhang, F. Qiu, H. Yang, A glassy carbon electrode modified with carbon dots and gold nanoparticles for enhanced electrocatalytic oxidation and detection of nitrite, Microchim Acta, 183(10), 2016, 2807-2814.

[28] B.D. Mansuriya Z. Altintas, Applications of graphene quantum dots in biomedical sensors, Sensors, 20(4), 2020, 1072.

[29] Y. Wang, H. Xu, J. Zhang, G. Li, Electrochemical sensors for clinic analysis, Sensors, 8, 2008, 2043-2081.

[30] S.S. Shankar, R.M. Shereema, V. Ramachandran, T.V. Sruthi, V.B.S. Kumar, R.B. Rakhi, Carbon quantum dot-modified carbon paste electrode-based sensor for selective and sensitive determination of adrenaline, ACS Omega, (4), 2019, 7903-7910.

[31] O.C. Bodur, S. Dinc, M. Ozmen, F. Arslan, A sensitive amperometric detection of neurotransmitter acetylcholine using carbon dot-modified carbon paste electrode, Biotechol Appl Biochem, 2020.

[32] Z. Zhou, P. Zhao, C. Wang, P. Yang, Y. Xie, J. Fei, Ultra-sensitive amperometric determination of quercetin by using a glassy carbon electrode modified with a nanocomposite prepared from aminated graphene quantum dots, thiolated beta-cyclodextrin and gold nanoparticles, Microchim Acta, 187, 2020, 130.

[33] T. Sridara, J. Upan, G. Saianand, A. Tuantranont, C. Karuwan, J. Jakmunee, Non-enzymatic amperometric glucose sensor based on carbon nanodots and copper oxide nanocomposites electrode, Sensors, 20(3), 2020, 808.

[34] M.H. Nguyen, G. Wong, E. Gane, J.-H. Kao, G. Dusheiko, Hepatitis B virus: Advances in prevention, diagnosis, and therapy, Clin Microbiol Rev, 33(2), 2020, e00046-19.

[35] Q. Yan, Y. Yang, Z. Tan, Q. Liu, H. Liu, P. Wang, L. Chen, D. Zhang, Y. Li, Y. Dong, A label-free electrochemical immunosensor based on the novel signal amplification system of AuPdCu ternary nanoparticles functionalized polymer nanospheres, Biosens Bioelectron, 103, 2018, 151-157.

[36] H.-S. Wang, Q.-X. Pan, G.-X. Wang, A biosensor based on immobilization of horseradish peroxidase in chitosan matrix cross-linked with glyoxal for amperometric determination of hydrogen peroxide, Sensors, 5(4), 2005, 266-276.

[37] S. Savas Z. Altintas, Graphene quantum dots as nanozymes for electrochemical sensing of yersinia enterocolitica in milk and human serum, Materials, 12(13), 2019, 2189.

[38] S.K. Arumugasamy, S. Govindaraju, K. Yun, Electrochemical sensor for detecting dopamine using graphene quantum dots

incorporated with multiwall carbon nanotubes, Appl Surf Sci, 508, 2020, 145294.

[39] P. Mohammadzadeh Jahani, Graphene quantum dots/ionic liquid-modified carbon paste electrode-based sensor for simultaneous voltammetric determination of norepinephrine and acetylcholine, Int J Electrochem Sc, 2020, 947-958.

[40] B. Sun, Y. Wang, D. Li, W. Li, X. Gou, Y. Gou, F. Hu, Development of a sensitive electrochemical immunosensor using polyaniline functionalized graphene quantum dots for detecting a depression marker, Mat Sci Eng C Mater, 111, 2020, 110797.

[41] B. Tian, Y. Kou, X. Jiang, J. Lu, Y. Xue, M. Wang, L. Tan, Ultrasensitive determination of mercury ions using a glassy carbon electrode modified with nanocomposites consisting of conductive polymer and amino-functionalized graphene quantum dots, Microchim Acta, 187, 2020, 210.

[42] S. Majumdar, D. Thakur, D. Chowdhury, DNA Carbon-Nanodots based electrochemical biosensor for detection of mutagenic nitrosamines, ACS Appl Bio Mater, 3(3), 2020, 1796-1803.

[43] Q. Xiang, J. Huang, H. Huang, W. Mao, Z. Ye, A label-free electrochemical platform for the highly sensitive detection of hepatitis B virus DNA using graphene quantum dots, RSC Adv, 8(4), 2018, 1820-1825.

[44] A. Valipour M. Roushani, Using silver nanoparticle and thiol graphene quantum dots nanocomposite as a substratum to load antibody for detection of hepatitis C virus core antigen: Electrochemical oxidation of riboflavin was used as redox probe, Biosens Bioelectron, 89, 2017, 946-951.

[45] F. Abazar A. Noorbakhsh, Chitosan-carbon quantum dots as a new platform for highly sensitive insulin impedimetric aptasensor, Sensor Actuat B-Chem, 304, 2020, 127281.

[46] W. Ye, J. Guo, X. Bao, T. Chen, W. Weng, S. Chen, M. Yang, Rapid and sensitive detection of bacteria response to antibiotics using nanoporous membrane and graphene quantum dot (gqds)-based electrochemical biosensors, Material, 10, 2017, 603.

[47] A.D. Chowdhury, K. Takemura, T.C. Li, T. Suzuki, E.Y. Park, Electrical pulse-induced electrochemical biosensor for hepatitis E virus detection, Nat Commun, 10, 2019, 3737.

[48] H. Zhu, X. Wang, Y. Li, Z. Wang, F. Yang, X. Yang, Microwave synthesis of fluorescent carbon nanoparticles with electrochemiluminescence properties, Chem Commun (Camb), (34), 2009, 5118-20.

[49] L.-L. Li, J. Ji, R. Fei, C.-Z. Wang, Q. Lu, J.-R. Zhang, L.-P. Jiang, J.-J. Zhu, A facile microwave avenue to electrochemiluminescent two-color graphene quantum dots, Adv Funct Mater, 22(14), 2012, 2971-2979.

[50] Y. Hu, L. Su, S. Wang, Z. Guo, Y. Hu, H. Xie, A ratiometric electrochemiluminescent tetracycline assay based on the combined use of carbon nanodots, $Ru(bpy)_3^{2+}$, and magnetic solid phase microextraction, Microchim Acta, 186(8), 2019, 512.

[51] R. Zhu, Y. Zhang, J. Wang, C. Yue, W. Fang, J. Dang, H. Zhao, Z. Li, A novel anodic electrochemiluminescence behavior of sulfur-doped carbon nitride nanosheets in the presence of nitrogen-doped carbon dots and its application for detecting folic acid, Anal Bioanal Chem, 411(27), 2019, 7137-7146.

[52] S. Li, C. Liu, G. Yin, Q. Zhang, J. Luo, and N. Wu, Aptamer-molecularly imprinted sensor base on electrogenerated chemiluminescence energy transfer for detection of lincomycin, Biosens Bioelectron, 91, 2017, 687-691.

[53] Y. Wu, Y. Chen, S. Zhang, L. Zhang, J. Gong, Bifunctional S, N-Codoped carbon dots-based novel electrochemiluminescent bioassay for ultrasensitive detection of atrazine using activated mesoporous biocarbon as enzyme nanocarriers, Anal Chim Acta, 1073, 2019, 45-53.

[54] R. Zhang, A. Chen, Y. Yu, Y. Chai, Y. Zhuo, R. Yuan, Electrochemiluminescent carbon dot-based determination of microRNA-21 by using a hemin/G-wire supramolecular nanostructure as co-reaction accelerator, Microchim Acta, 185(9), 2018, 432.

[55] M. Amiri, A. Bezaatpour, H. Jafari, R. Boukherroub, S. Szunerits, Electrochemical methodologies for the detection of pathogens, ACS Sensors, 3(6), 2018, 1069-1086.

[56] H.F. Zhao, R.P. Liang, J.W. Wang, J.D. Qiu, A dual-potential electrochemiluminescence ratiometric approach based on graphene quantum dots and luminol for highly sensitive detection of protein kinase activity, Chem Commun (Camb), 51(63), 2015, 12669-12672.

[57] C. Yang, Q. Guo, Y. Lu, B. Zhang, G. Nie, Ultrasensitive "signal-on" electrochemiluminescence immunosensor for prostate-specific antigen detection based on novel nanoprobe and poly(indole-6-carboxylic acid)/flower-like Au nanocomposite, Sensor Actuat B-Chem, 303, 2020, 127246.

[58] C. Venkateswara Raju, G. Kalaiyarasan, S. Paramasivam, J. Joseph, S. Senthil Kumar, Phosphorous doped carbon quantum dots as an efficient solid state electrochemiluminescence platform for highly sensitive turn-on detection of Cu^{2+} ions, Electrochim Acta, 331, 2020, 135391.

[59] J. Peng, Z. Zhao, M. Zheng, B. Su, X. Chen, X. Chen, Electrochemical synthesis of phosphorus and sulfur co-doped graphene quantum dots as efficient electrochemiluminescent immunomarkers for monitoring okadaic acid, Sensor Actuat B-Chem, 304, 2020, 127383.

[60] G. Kalaiyarasan, C.V. Raju, M. Veerapandian, S.S. Kumar, J. Joseph, Impact of aminated carbon quantum dots as a novel co-reactant for $Ru(bpy)_3^{2+}$: Resolving specific electrochemiluminescence for butein detection, Anal Bioanal Chem, 412(3), 2020, 539-546.

[61] S. Chen, X. Chen, L. Zhang, J. Gao, Q. Ma, Electrochemiluminescence Detection of Escherichia coli O157:H7 Based on a Novel Polydopamine Surface Imprinted Polymer Biosensor, ACS Appl Mater Inter, 9(6), 2017, 5430-5436.

[62] S. Li, J. Liu, Z. Chen, Y. Lu, S.S. Low, L. Zhu, C. Cheng, Y. He, Q. Chen, B. Su, Q. Liu, Electrogenerated chemiluminescence on smartphone with graphene quantum dots nanocomposites for Escherichia Coli detection, Sensor Actuat B-Chem, 297, 2019, 126811.